Digital Signal Processing for Optical Communications and Coherent LiDAR

Wenting Yi

A dissertation submitted to

University College London

for the degree of

Doctor of Philosophy

Department of Electronic & Electrical Engineering

University College London

April 2023

I, Wenting Yi, confirm that the work presented in this thesis is my own. Where information has been derived from other sources, I confirm that this has been indicated in the work.

Abstract

Internet data traffic within data centre, access and metro networks is experiencing unprecedented growth driven by many data-intensive applications. Significant efforts have been devoted to the design and implementation of low-complexity digital signal processing (DSP) algorithms that are suitable for these short-reach optical links. In this thesis, a novel low-complexity frequency-domain (FD) multiple-input multiple-output (MIMO) equaliser with momentum-based gradient descent algorithm is proposed, capable of mitigating both static and dynamic impairments arising from the optical fibre. The proposed frequency-domain equaliser (FDE) also improves the robustness of the adaptive equaliser against feedback latencies which is the main disadvantage of FD adaptive equalisers under rapid channel variations.

The development and maturity of optical fibre communication techniques over the past few decades have also been beneficial to many other fields, especially coherent light detection and ranging (LiDAR) techniques. Many applications of coherent LiDAR are also cost-sensitive, e.g., autonomous vehicles (AVs). Therefore, in this thesis, a low-cost and low-complexity single-photodiode-based coherent LiDAR system is investigated. The receiver sensitivity performance of this receiver architecture is assessed through both simulations and experiments, using two ranging waveforms known as double-sideband (DSB) amplitude-modulated chirp signal and single-sideband (SSB) frequency-modulated continuous-wave (FMCW) signals. Besides, the impact of laser phase noise on the ranging precision when operating within and beyond the laser coherence length is studied. Achievable ranging precision beyond the laser coherence length is quantified.

Impact statement

Low-complexity digital signal processing (DSP) algorithms are desirable for cost-sensitive intra- and inter-data centre connections. In this thesis, a novel low-complexity frequency-domain equaliser (FDE) is proposed. It combines static chromatic dispersion compensation and an adaptive multiple-input multiple-output (MIMO) equaliser for mitigating time-varying effects, such as polarisation mode dispersion (PMD) and state of polarisation (SOP) rotations, in one fast Fourier transform (FFT) block processing. The interim FFT operations between individual DSP stages can therefore be avoided, reducing computational complexity. Additionally, the momentum-based gradient descent method is applied to the frequency-domain adaptive MIMO equaliser for the first time. It is shown to be capable of mitigating penalties arising from the feedback delays of the adaptive equaliser, the major disadvantage in the adaptive frequency-domain equalisation. Numerical simulations show that, compared to the conventional gradient descent algorithm, the proposed momentum-based gradient descent equaliser is significantly more tolerant to feedback latencies under rapid channel variations.

Leveraging the maturity of optical fibre communication techniques, a low-cost single-photodiode based coherent light detection and ranging (LiDAR) receiver, suitable for LiDAR applications that require high cost-efficiency, is investigated in this thesis. Through both experiments and simulations, it is shown that the single-sideband (SSB) frequency-modulated continuous-wave (FMCW) signal is a strong candidate for such coherent receivers. It does not suffer from laser phase noise to amplitude noise conversion, as is the case with double-sideband

(DSB) amplitude-modulated chirp signal, hence offering a better receiver sensitivity performance. The system limitations and trade-offs in such single-photodiode based coherent LiDAR systems are also identified.

Apart from the coherent receiver, the linewidth of the transmitter laser is also critical for LiDAR performance. The dependence of ranging precision on the laser linewidth and ranging distance is assessed through both experiments and simulations in this thesis. The achievable ranging precision when operating within and beyond the laser coherence length is identified.

In summary, the research work presented in this thesis makes significant contributions to the understanding and implementation of low-complexity optical communication and coherent LiDAR systems.

Acknowledgements

First and foremost, I would like to thank my primary supervisor Prof. Robert Killey, for giving me this opportunity to pursue this PhD with the Optical Networks Group (ONG) at UCL, and for sharing his wisdom, knowledge and experience with me. Without his support and guidance, none of this work would have been possible. I would also like to thank my secondary supervisor Prof. Polina Bayvel, who set up this world-leading research group. Her success in scientific research and career is truly inspiring to many female students in Science and Engineering, including me.

Besides my supervisors, I am deeply grateful for the tremendous help I received from many former and current ONG members - forever shout-out :-). I would like to thank Dr. Zhe Li for the fruitful discussions from my early work on Kramers-Kronig (KK) scheme to later on light detection and ranging (LiDAR). I am also thankful to Dr. Lidia Galdino, Dr. Eric Sillekens, and Dr. Domaniç Lavery for introducing me to the lab and sharing their knowledge of digital signal processing with me. Thanks also go to Dr. Zhixin Liu, Mr. Zichuan Zhou, Dr. Callum Deakin, Dr. Filipe Ferreira, Mr. Ronit Sohanpal, and Dr. Thomas Gerard for the support and advice on LiDAR experiments. I am also grateful to Dr. Paris Andreades, Dr. Boris Karanov, Dr. Hui Yuan, Dr. Yuta Wakayama, Mrs. Xun Mu, Dr. Hubert Dzieciol as well as many other ONG members, from serious research discussions to coffee, tea, home-made cakes, frappe, guacamole, fun and laughs in 808.

In addition, I would like to acknowledge the financial support from UCL Overseas Research Scholarship and UCL Graduate Research Scholarship.

Last but not least, I would like to offer my sincere gratitude to all my family members and friends for their unceasing support, love and trust in me.

Contents

List of Figures

List of Tables

Chapter 1

Introduction

1.1 Introduction to optical communication and LiDAR technique

Data traffic today is experiencing an unprecedented rate of increase. It was predicted that by 2023, two-thirds of the global population will have Internet access, accounting for 5.6 billion Internet users [1]. In addition, there will be 3.6 networked devices per capita by 2023, accelerated by the growth of Internet of Things (IoT) where different kinds of devices are able to connect with each other and exchange data over the network [1]. Among them, video devices, in particular, generate a huge amount of data traffic, stimulated by ultra-high-definition (UHD) video streaming, real-time gaming and so on. In fact, during the outbreak of the Covid-19 pandemic, the shift to remote working, lecturing, and social activities led to a 20% increase of Internet traffic within one week [2]. In order to help ease this broadband strain, many streaming platforms reduced the default video quality or bit rates of streams [3]. This (hopefully once-in-a-lifetime) global health crisis may also change the way in which we communicate and collaborate over the long term, as many companies announced that their employees can continue to work remotely post-pandemic [4]. This continuing demand for high-quality and low-latency online meetings and real-time communications will further add to the growth of Internet data traffic.

In addition, the advances of augmented reality (AR) and virtual reality (VR)

technologies in recent years, and the emergence of so-called 'Metaverse', with which people are able to interact seamlessly using digital avatars, are expected to push data usage by more than 20 times over the next decade [5–7]. While these technologies open up our imagination about the future, all of them can only be made possible by having a robust and reliable underlying communication infrastructure with fast speed and low latency.

Such demand for high data rate transmission capacity motivated the innovations and developments of optical fibre communications in the last few decades, which essentially served as the backbone for Internet data traffic. The use of optical fibre as the transmission medium was first proposed in 1966 [8]. The fibre at that time suffered from high loss. The improvements in the manufacturing process have significantly reduced the fibre attenuation, resulting in a low-loss window of 0.2 dB/km around 1550 nm, which led to optical fibre becoming the preferred communication medium [9]. In the early stage of optical fibre transmission, only intensity-modulated signal formats with non-coherent detection were utilised, known as intensity modulation (IM) / direct detection (DD). In such schemes, only the amplitude is used for signalling and the signal phase information is lost during the nonlinear square-law detection, which significantly limits the transmission capacity.

To increase the system throughput, coherent optical fibre communication attracted a lot of research interest in the 1980s [10, 11]. The presence of a local oscillator (LO) improves the receiver sensitivity and allows more degrees of freedom, including amplitude, phase and polarisation, to be employed for encoding data. However, owing to the difficulty and complexity in implementing coherent receivers at that time, especially the optical phase-lock loop (PLL) for aligning the phase of the received signal and the LO, its popularity was overtaken by the invention of optical amplifiers, i.e., Erbium-doped fibre amplifier (EDFA) [12]. The EDFA can optically amplify the signal over a wide spectrum to compensate the loss induced in the optical fibre. Together with the wavelength division multiplexing (WDM) technique, in which independent channels can be transmitted at different

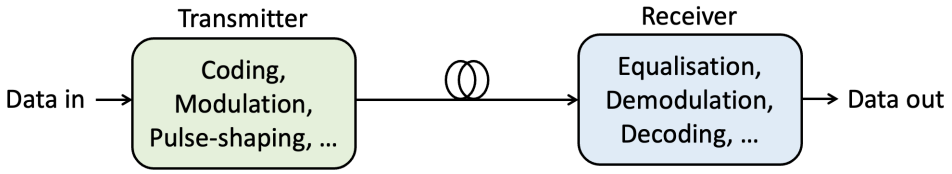

Figure 1.1: Basic schematic of a digital coherent transceiver with some of the main signal processing modules at the transmitter and the receiver [17].

wavelengths, this led to a significant increase in the system throughput compared to that with the traditional IM/DD technique [13, 14].

After 2000, the development of high-speed digital-to-analogue converter (DAC) and analogue-to-digital converter (ADC) technologies, and advanced digital signal processing (DSP) algorithms renewed interest in coherent detection. With the LO serving as the phase reference at the receiver, the optical field can be fully captured at photodetection. The detected electrical signal can then be digitised and passed to DSP modules for mitigation of various linear and nonlinear impairments arising from the optical channels. Such digital coherent transceivers lead to significant enhancement of spectral efficiency. Fig.1.1 shows the schematic of a digital coherent transceiver with the main signal processing modules at the transmitter and the receiver. Nowadays, DSP-based coherent optical transceivers with WDM and forward error correction (FEC), a data coding mechanism to enhance the system throughput, have become a standard for long-distance optical fibre communication systems [15, 16].

There have been a number of investigations on many other novel techniques to further improve the system throughput in order to keep up with the growth of data traffic, for instance, coded modulation schemes, where the position of constellation points or the occurrence probability of the points, known as geometric shaping (GS) and probabilistic shaping (PS) respectively, can be optimised to improve the system's tolerance to certain noise and hence enhance the spectral efficiency [18, 19]. Besides, extending the transmission bandwidth beyond conventional (C) band (1530-1565 nm) and long (L) band (1565-1625 nm) has attracted a lot of research interest [20–22]. Table.1.1 shows the wavelength range and the average fibre loss of each transmission band in the SSMF [23]. Combining all the bands

Band	Wavelength range	Bandwidth in frequency	Average fibre loss [dB/km]	Amplification
O	1260-1360	17.5 THz	0.36	PDFA
E	1360-1460	15.1 THz	0.28	BDFA
S	1460-1530	9.4 THz	0.22	TDFA
C	1530-1565	4.4 THz	0.18	EDFA
L	1565-1625	7.1 THz	0.18	EDFA

Table 1.1: Low loss transmission band of single mode fibre [23]. O band: original band; E band: extended band; S band: short band; C band: conventional band; L band: long band; PDFA: Praseodymium-doped fibre amplifier; BDFA: Bismuth-doped fibre amplifier; TDFA: Thulium-doped fibre amplifier; EDFA: Erbium-doped fibre amplifier.

together can give a total transmission bandwidth of 365 nm. With the assistance of a variety of optical amplifiers, such as rare-earth-doped fibre amplifiers as shown in Table.1.1, ultra-wideband transmission is proven to potentially play a leading role in supporting high-capacity transmission [24–26]. Alternatively, multiple spatial paths of the optical fibre can be utilised to carry information. This type of technique is referred to as space division multiplexing (SDM) [27] [28]. SDM techniques range from standard fibre bundles to multicore fibres or multimode fibres. Though SSMF bundles do not require distinct associated fibre techniques, multicore fibres and multimode fibres normally need a modified fibre design and profile [28].

More recently, the progress in the machine learning (ML) and deep learning (DL) field has also motivated its application to optical fibre communication systems [17, 29, 30]. A number of studies have explored the use of ML techniques or neural networks to, for example, reduce the computational complexity of digital back propagation (DBP) for mitigating linear and nonlinear impairments from the optical fibre [31, 32] or to decrease the demodulation complexity of received symbols in additive white Gaussian noise (AWGN) channels [33].

The rapid development and maturity of optical fibre communication techniques

over the past few decades have also been beneficial to many other applications. High-performance lasers and optical amplifiers, advanced modulators, coherent receivers that are commonly used in telecommunications have found applications in areas such as optical sensing, spectroscopy, chemical sensing and so on [34–38]. Among them, one of the emerging topics is light detection and ranging (LiDAR). LiDAR is essentially the counterpart of the conventional technique radio detection and ranging (Radar) in the optical domain. Instead of using radio frequency (RF) waves to detect the distance and velocity of the object, LiDAR uses light at a much higher frequency for sensing. The resulting shorter wavelength enables LiDAR to generate the point cloud at a much higher resolution and precision compared to Radar.

Using a laser as the light source for sensing is not new. This technique was first demonstrated in Massachusetts Institute of Technology (MIT) Lincoln Laboratory, shortly after the invention of the laser in 1960 [39]. Since then, it has been developed and applied across a wide range of areas including topography, anemometry and biomedical sensing [38, 40, 41]. In 2005, the LiDAR sensor was applied for the first time to autonomous driving vehicles in the 2nd Defense Advanced Research Projects Agency (DARPA) Autonomous Vehicle Grand Challenge [42]. The winner of this competition, Stanley from Stanford University, was equipped with 5 roof-mounted SICK LiDAR units to build a 3D map of the environment [43]. In the same race, the first version of Velodyne 360° scanning LiDAR, which is now a key player in the LiDAR market, was introduced, capable of generating a high-resolution point cloud at more than 100 meters [42, 44]. In the following 3rd Challenge in 2007, 5 out of 6 winning teams were equipped with Velodyne LiDAR [44]. The booming of the autonomous vehicle (AV) market since then rejuvenated industrial and research interest in LiDAR.

For applications in AVs, the optical wavelength at around 1550 nm is particularly attractive. On the one hand, advanced lasers, optical modulators, and coherent receivers can be bought off-the-shelf thanks to the development of optical fibre communications. On the other hand, as human eyes are less sensitive to

Parameter	Short range	Long range
Range	20-30 m	200-300 m
Axial/longitudinal resolution	a few cm	
Lateral/azimuthal resolution	1°	0.1-0.15 °
Precision	$\sim$ mm	$\sim$ cm
Frame rate	10-25 Hz	
FOV	$>$ 90 °	$<$ 90 °
Temperature range	ACE-Q100 grade 2	
Reliability	AEC-Q100	
Laser safety	IEC60825-1 Class 1	
Size	100 cm^3 - 200 cm^3	
System cost	$ 50	$ 100-200

Table 1.2: Suggested automotive LiDAR performance specifications [47, 48]. FOV: field-of-view.

this wavelength, it can potentially alleviate eye safety issues when operating in free space, allowing the possibility of transmitting the signal at a higher power for detecting the target at a longer distance (200-300 m) [44]. Together with well-established sensors such as Radar, ultrasonic sensors and cameras, LiDAR is widely regarded as an excellent complement in self-driving cars [45, 46].

Apart from AVs, as mentioned earlier, LiDAR as an optical sensing technique is useful for applications such as medical sensing, robotics and video gaming. For different applications, the required LiDAR performance varies and different trade-offs have to be made in the system design, carefully balancing cost, size, performance and reliability. As the research work presented in this thesis focuses

on the application to AVs, metrics for evaluating LiDAR's performance in the short and long-distance ranging are listed in Table 1.2, together with typical suggested specifications [47, 48]. In this table, short-range usually refers to the case of side-looking or rearview, while long-range refers to the scenario of forward-looking. Axial/longitudinal resolution indicates the minimum resolvable distance in the direction parallel to the beam direction while lateral/azimuthal resolution is for assessing the resolution in the direction perpendicular to the beam. By scanning horizontally and vertically, LiDAR can generate a 3D map, also known as a frame. Typically, 10-25 frames are produced in one second, known as the frame rate. The parameter precision, obtained by calculating the standard deviation of multiple measurements of a target at a certain distance, suggests the confidence in the measurement of the target location. The field-of-view (FOV) represents the beam steering angle of the LiDAR sensor.

1.2 Research problem

Despite the exponential growth of Internet data traffic, it is reported that 86 % of the data traffic is related to intra-data centre and inter-data centre communications, where the transmission distance is below $\sim$100 km [23, 49]. Unlike long-haul optical transmission systems, for which the main objective is to support reliable and high data rate communication, the primary goal for implementing short-reach optical fibre communication links (i.e.,$<$100 km) is cost-efficiency. Major efforts have been put into investigations of low-complexity and cost-effective transceivers and DSP algorithms for applications on short-reach systems. While fibre nonlinearity has a major impact on long-haul transmissions as it accumulates with the transmission distance, in short optical links, linear impairments such as fibre loss, chromatic dispersion (CD), polarisation mode dispersion (PMD) and state of polarisation (SOP) rotations are the main causes of system penalty. As the research work presented in this thesis focuses on short distances for applications in data centre, metro and access networks, the penalties arising from the optical channel are confined to linear distortions.

The fundamental causes of these impairments and various DSP algorithms for their mitigation will be reviewed in detail in Chapter 2. While the fibre loss due to material absorption and Rayleigh scattering is often compensated by optical amplifiers, the other linear impairments need to be mitigated with the DSP. In general, chromatic dispersion is often considered a static effect and can be mitigated via a non-adaptive frequency-domain equaliser (FDE) by multiplying the signal with the inverse transfer function of the dispersive link [50]. The latter two effects, i.e., polarisation mode dispersion and state of polarisation rotation caused by fibre birefringence, are non-static and typically vary with time. To mitigate the resulting signal distortions, an adaptive equaliser is required, which uses an iterative search algorithm to find the optimum filter coefficients to minimise the error and recover the signal [51]. In the polarisation-division multiplexing (PDM) coherent system, the adaptive equaliser is implemented in a butterfly structure, known as an adaptive 2×2 multiple-input multiple-output (MIMO) equaliser [52–54]. Conventionally, the adaptive MIMO equaliser is processed in the time-domain (TD) through sample-by-sample equalisation [54]. Together with a non-adaptive FDE for chromatic dispersion compensation (CDC) preceding the MIMO equaliser, this structure is mostly used in the receiver DSP for PDM coherent systems [55–58].

Nevertheless, the TD adaptive 2×2 MIMO equaliser is rather computationally expensive and power-hungry, especially when the filter length is large [59]. In fact, this adaptive MIMO equaliser is often found to be the most power-consuming block in the coherent DSP chain for short-reach optical links in addition to FEC [52]. Therefore, many advanced DSP algorithms propose to move the adaptive time-domain equaliser (TDE) to the frequency domain [60–62]. Instead of performing sample-by-sample equalisation as in the time domain, frequency-domain (FD) equalisers process a large block of samples together. Taking advantage of the low calculation complexity offered by fast Fourier transform (FFT), the computational complexity can be significantly reduced [63]. With the filter length of N samples, the computational complexity per sample of a FDE increases approximately proportional to $O(\log_2 N)$ while the TDE scales as

$O(N)$ [55]. Hence, with increased filter length, there is a great benefit of employing FDEs due to the significant reductions in the computational complexity compared to the TDE.

The low complexity and reduction in the power consumption offered by an adaptive FDE come with the trade-off of feedback delays in the filter coefficients update, which is the main disadvantage of adaptive FDE. This is due to the presence of multiple FFTs/IFFTs and DSP operations involved in calculating errors and updating gradients in the feedback loop [55, 64–66]. Such delays will degrade the adaptive equaliser's ability to track time-varying effects as the filter coefficients are no longer up-to-date. This is particularly detrimental during rapid SOP rotations, for instance when aerial fibres used in a transmission link are struck by lightning, leading to SOP rotation frequencies on the order of a few Mrad/s [67–69]. Improving the robustness of the adaptive FDE against feedback latencies is hence crucial to successfully recover the PDM signals.

Since it is possible to mitigate CD, PMD and SOP rotations together in the frequency domain, it is beneficial to further combine these individual DSP stages into one block, avoiding interim FFT/IFFT conversions to further reduce the computational complexity. The design and implementation of such a low-complexity FDE, combining static equaliser and adaptive MIMO equaliser together, and the algorithm to improve the adaptive equaliser's tolerance to feedback latencies, have been investigated in this thesis.

For the implementation of LiDAR systems, minimising system cost while still maintaining desirable performance is also important [47, 70]. Generally, there are three categories of LiDAR, known as pulsed time-of-flight (ToF) LiDAR, amplitude-modulated continuous-wave (AMCW) LiDAR and frequency-modulated continuous-wave (FMCW) LiDAR. The operating principles and related literature will be reviewed in Chapter 2. This thesis focuses on the investigation of FMCW LiDAR, as it offers a higher receiver sensitivity, and higher ranging resolution and precision over longer distances compared to the other two techniques.

There are two approaches to generate the FMCW signal. One is to directly

modulate the laser which is simple and low cost [71, 72]. The directly modulated laser (DML) can offer a frequency tuning from tens of GHz to even THz, thus enabling a high-ranging resolution in the LiDAR system [35,73,74]. However, such lasers usually suffer from a larger laser phase noise, limiting the maximum ranging distance [45, 75]. This results in a system trade-off between ranging resolution and ranging distance. Apart from the laser phase noise, obtaining a precise linear frequency sweep is rather challenging in the case of directly modulating a laser, and a linearisation technique is often required to optimise the signal waveform [76–78]. In addition, the frequency modulation of a laser by varying the injection current into the gain section often comes with an unwanted intensity modulation which cannot be compensated. To overcome these drawbacks, an alternative approach is to externally modulate the laser source using an electro-optic modulator (EOM). Apart from the possibility of using a low-linewidth laser source, this approach offers a better modulation linearity and control of the frequency and amplitude of the chirp signal.

When using an EOM to generate the chirp signal, there are two categories of chirp signals that have been proposed for ranging, known as single-sideband (SSB) frequency-modulated continuous-wave (FMCW) signal and double-sideband (DSB) amplitude-modulated chirp signal [79, 80]. The DSB signal requires a simpler transmitter design, as it is real-valued and can be generated using a single-drive Mach-Zehnder modulator (MZM), while the SSB signal, which is frequency/phase modulated, requires an in-phase and quadrature modulator (IQM) based transmitter. The operating principle of these two waveforms will be discussed in the research work presented in Chapter 4. Both signals have previously been investigated in an optical 90° hybrid-based balanced phase-diversity coherent receiver [79–81]. Nonetheless, this receiver architecture is rather complex and expensive, limiting its practical implementations. Hence, a simplified receiver architecture design for coherent LiDAR, which is desirable for cost-sensitive applications such as autonomous vehicles, has been studied in this thesis, and the performance of systems employing these two chirp waveforms has been assessed.

Besides the coherent receiver, the transmitter laser is critical for LiDAR performance. As mentioned earlier, the maximum ranging distance is commonly assumed to be limited by the laser coherence length [74]. This is because the ranging precision can be degraded by incoherent measurements. Hence, to enable long-distance ranging of a few hundred meters, a low-linewidth laser is often assumed to be necessary, which potentially increases the system cost. A number of studies have explored the possibility of mitigating precision penalties from laser phase noise. For instance, in [75], by exploiting the prior knowledge of the power spectral density (PSD) of the received signal and using a least-squares estimation, $10\times$ better-ranging precision can be realised when operating beyond the laser coherence distance. Although a certain degradation in ranging precision would be expected in the incoherent regime, its dependence on ranging distance and laser linewidth has not been thoroughly assessed. If the performance is acceptable, the use of a relatively high-linewidth laser source might be a compromise solution for many cost-sensitive applications.

It should be noted that the research work carried out in this thesis focuses on the LiDAR subsystem designs and evaluations. Immense efforts have been made across industry and academia to fully integrate the LiDAR system on chip in order to make it more power-efficient, compact and easily scalable for mass production [48, 70, 82–87]. Readers are referred to the aforementioned references for more exhaustive discussion and review of various integrated LiDAR systems.

1.3 Thesis outline

The remainder of the thesis is organised as follows:

Chapter 2 presents the requisite theory for linear impairments that arise from the optical fibre, including CD, PMD, and SOP rotations. Various DSP techniques that have been proposed in the literature for the mitigation of these impairments are reviewed. The second half of this chapter focuses on LiDAR systems. The operating principle of different LiDAR techniques, i.e., pulsed TOF LiDAR, AMCW LiDAR and FMCW LiDAR are discussed. Achievable performance in commercialised

products are presented. As coherent FMCW LiDAR is the focus of this thesis, its related literature is reviewed in more detail.

In chapter 3, a novel low-complexity frequency-domain MIMO equaliser employing a momentum-based gradient descent algorithm is proposed. The principles of the proposed FD MIMO equaliser are presented first. Its performance is evaluated through numerical simulations of varying feedback delays and SOP rotation speeds. The simulation results are discussed and compared with those obtained using the conventional gradient descent algorithm.

Chapter 4 compares the performance of two categories of chirp signals, namely DSB amplitude-modulated signal and SSB FMCW signal, in a low-cost and low-complexity single-photodiode based coherent LiDAR system. The impact of direct detection (DD) beating distortions arising from single-photodiode detection, and penalties in receiver sensitivity due to laser phase noise are mathematically studied first with expressions to calculate this being derived. Both simulations and experiments are then performed for verification, followed by a detailed discussion and comparison between simulation and experiment results.

Chapter 5 investigates the impact of laser phase noise on the ranging precision when operating within and beyond the laser coherence length. Experimental results comparing the ranging precision of 100 kHz and 1.2 MHz laser sources at various ranging distances are discussed first, following which simulation results, sweeping across a wide range of ranging distances and laser linewidths, are presented.

Chapter 6 summarises the research work presented in Chapters 3, 4 and 5. Suggestions for future work are also proposed.

1.4 Key contributions

The key contributions from the research work presented in this thesis are as follows:

- A novel low-complexity frequency-domain equalisation technique, combining chromatic dispersion compensation and an adaptive MIMO equaliser in one FFT block is proposed (Section 3.1). The proposed equaliser has the advantage of saving intermediate FFTs/IFFTs between individual DSP stages.

The algorithm was published in VII as listed below in Section 1.5.

- A momentum-based gradient descent algorithm is applied to the FD adaptive MIMO equaliser for the first time in order to improve its robustness against adaptive filter feedback delays and dynamic SOP rotations (Section 3.1). Through numerical assessments, the momentum-based gradient descent is shown to outperform the conventional gradient descent algorithm, capable of mitigating penalties from high feedback delays in the presence of rapid SOP rotations (Section 3.3). The results were published in VII.

- Theoretical equations for desired beat signal, direct detection beating interference, and the impact of laser phase noise on the receiver sensitivity when employing SSB FMCW signal and DSB amplitude-modulated signal in single-photodiode based coherent LiDAR systems are derived and analysed (Section 4.1). This led to the publication of III.

- Numerical simulations and experimental verifications are performed to compare the receiver sensitivity performance with SSB and DSB signals (Section 4.3). System limitations and trade-offs in this single photodiode based coherent LiDAR receiver are discussed. The results were published in III.

- The penalties arising from the laser phase noise on the ranging precision when operating within and beyond the laser coherence length are investigated. Experiments are carried out comparing the ranging precision of 1.2 MHz and 100 kHz linewidth lasers for a variety of ranging distances (Section 5.1). Results were reported in I.

- Numerical assessments are performed across a wide range of distances and laser linewidths (Section 5.2). Achievable ranging precision with varying laser linewidths and ranging distances is identified and reported in I.

1.5 List of publications

The following is the list of original work published in this course of research:

I) **W. Yi**, Z. Zhou, Z. Liu, P. Bayvel, and R. I. Killey, "Impact of laser phase noise on ranging precision within and beyond laser coherence length in FMCW LiDAR," in 2023 Optical Fiber Communication Conference (OFC). Optica, 2023, pp. M3F.3.

II) J. Yang, E. Sillekens, **W. Yi**, P. Bayvel, and R. I. Killey, "Joint estimation of dynamic polarization and carrier phase with pilot-based adaptive equalizer in PDM-64 QAM transmission system," Optica Optics Express, vol. 29, no. 26, pp. 43136–43147, 2021.

III) **W. Yi**, Z. Li, Z. Zhou, E. Sillekens, T. Gerard, C. Deakin, F. M. Ferreira, L. Galdino, Z. Liu, P. Bayvel, and R. I. Killey, "Frequency-modulated chirp signals for single-photodiode based coherent LiDAR system," IEEE/Optica Journal of Lightwave Technology, vol. 39, no. 14, pp. 4661–4670, 2021.

IV) H. Buglia, E. Sillekens, A. Vasylchenkova, **W. Yi**, R. Killey, P. Bayvel, and L. Galdino, "Challenges in extending optical fibre transmission bandwidth beyond C+L band and how to get there," in 2021 International Conference on Optical Network Design and Modeling (ONDM). IEEE, 2021, pp. 1–4.

V) E. Sillekens, **W. Yi**, D. Semrau, A. Ottino, B. Karanov, D. Lavery, L. Galdino, P. Bayvel, R. I. Killey, S. Zhou et al., "Time-domain learned digital back-propagation," in 2020 IEEE Workshop on Signal Processing Systems (SiPS). IEEE, 2020, pp. 1–4.

VI) L. Galdino, A. Edwards, **W. Yi**, E. Sillekens, Y. Wakayama, T. Gerard, W. S. Pelouch, S. Barnes, T. Tsuritani, R. I. Killey et al., "Optical fibre capacity optimisation via continuous bandwidth amplification and geometric shaping," IEEE Photonics Technology Letters, vol. 32, no. 17, pp. 1021–1024, 2020.

VII) **W. Yi**, E. Sillekens, D. Lavery, H. Dzieciol, S. Zhou, K. Law, J. Chen, P. Bayvel, and R. I. Killey, "Performance of momentum-based frequency-domain MIMO equalizer in the presence of feedback delay," Optica Optics Express, vol. 28, no. 13, pp. 19133–19143, 2020.

VIII) **W. Yi**, Z. Li, M. S. Erkılınç, D. Lavery, E. Sillekens, D. Semrau, Z. Liu, P. Bayvel, and R. I. Killey, "Performance of Kramers–Kronig receivers in the presence of local oscillator relative intensity noise," IEEE/Optica Journal of Lightwave Technology, vol. 37, no. 13, pp. 3035–3043, 2019.

IX) R. I. Killey, M. S. Erkılınç, **W. Y**i, and P. Bayvel, "Low complexity self-coherent transceivers for metro, access and inter-datacenter applications," in 2019 Optical Fiber Communication Conference (OFC). Optica, 2019, pp. Tu2B–5.

Chapter 2

Theory and literature review

This chapter presents the requisite theory and literature review for the research described in this thesis. Sec.2.1 focuses on the linear impairments arising from the optical channel, and DSP algorithms that have been proposed to mitigate these distortions. Sec.2.2 introduces the LiDAR technique. Three types of commonly used LiDAR systems are discussed, namely, pulsed time-of-flight (ToF) LiDAR, amplitude-modulated continuous-wave (AMCW) LiDAR and frequency-modulated continuous-wave (FMCW) LiDAR, followed by a summary and comparison of these different LiDAR systems in Sec.2.2.4.

2.1 Linear optical fibre impairments and DSP mitigation algorithms

2.1.1 Chromatic dispersion

The refractive index of the optical fibre is frequency-dependent, resulting in different frequency components of the optical pulse travelling at different speeds. This phenomenon is referred to as chromatic dispersion (CD). The main penalty caused by chromatic dispersion in an optical communication system arises from the pulse broadening as shown in Fig.2.1. In the time domain, the broadened pulses may interfere with neighbouring pulses and induce inter-symbol interference (ISI). This is particularly detrimental to high-speed transmission systems, as the symbol period becomes rather short.

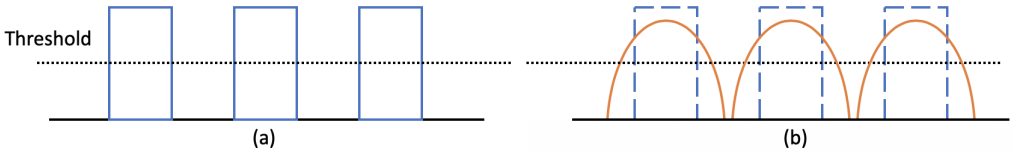

Figure 2.1: Inter-symbol interference (a) transmitted symbol; (b) broadened symbol.

From the mathematical perspective, if the amplitude of the optical signal is denoted as A, the propagation of each frequency component of the signal through standard single-mode fibre (SSMF) over a distance z can be described as [88]:

$$A(z,\omega) = A(0,\omega)\exp(j\beta z) \tag{2.1}$$

where ω is the angular frequency and β represents the mode-propagation constant. Expanding β as the Taylor series around the optical frequency ω_0 gives [88]:

$$\beta(\omega) = n(\omega)\frac{\omega}{c} = \beta_0 + \beta_1(\omega-\omega_0) + \frac{1}{2}\beta_2(\omega-\omega_0)^2 + ..., \tag{2.2}$$

$$\beta_m = \left(\frac{d^m\beta}{d\omega^m}\right)_{\omega=\omega_0} \tag{2.3}$$

where the parameter n is the refractive index, c denotes the speed of light and β_0 is the propagation constant at frequency ω_0.

The parameter β_1 specifies the velocity at which the optical pulse propagates in the fibre, known as the group velocity v_g. They are related to each other through [88]:

$$\beta_1 = \frac{d\beta}{d\omega} = \frac{1}{v_g} = \frac{n_g}{c} = \frac{1}{c}(n+\omega\frac{dn}{d\omega}) \tag{2.4}$$

where n_g is the group refractive index. The parameter β_2 denotes the 2nd-order dispersion, representing the dispersion of group velocity, and thus is responsible for pulse broadening [88]:

$$\beta_2 = \frac{d\beta_1}{d\omega} = \frac{d}{d\omega}\left[\frac{1}{c}(n+\omega\frac{dn}{d\omega})\right] = \frac{1}{c}(2\frac{dn}{d\omega}+\omega\frac{d^2n}{d\omega^2}) \tag{2.5}$$

This phenomenon is referred to as group velocity dispersion (GVD). The dispersion

of optical fibre is commonly specified by the chromatic dispersion parameter D (ps$\cdot$ nm^{-1}km^{-1}), which is related to β_2 through [88]:

$$D = \frac{d\beta_1}{d\lambda} = -\frac{2\pi c}{\lambda^2}\frac{d\beta_1}{d\omega} = -\frac{2\pi c}{\lambda^2}\beta_2 \tag{2.6}$$

where λ represents the reference wavelength and $d\lambda = -\frac{\lambda^2}{2\pi c}d\omega$. For SSMF operating at 1550 nm, $D \approx 17$ ps$\cdot$nm^{-1}km^{-1} [89, 90].

The higher-order dispersion plays a critical role in the propagation of ultrashort pulses (around tens of fs) or at wavelengths approaching the zero-dispersion wavelength at around 1.27 μm [88]. As the research work in this thesis considers systems operating at 1.55 μm, the impact of higher-order dispersion is neglected.

With negligible contribution to distortion from fibre nonlinearity, usually the case in short-reach optical links, the impact of chromatic dispersion on the signal's envelope $A(z,t)$ at time instance t and distance z can be modelled as [53]:

$$\frac{\partial A(z,t)}{\partial z} = j\frac{D\lambda^2}{4\pi c}\frac{\partial A^2(z,t)}{\partial t^2} \tag{2.7}$$

where $j = \sqrt{-1}$. Taking the Fourier transform of Eq.2.7 yields the frequency domain transfer function of the dispersive link, which is given by [53]:

$$G(z,\omega) = \exp\left(-j\frac{D\lambda^2 z}{4\pi c}\omega^2\right) \tag{2.8}$$

Hence, chromatic dispersion can be modelled simply by multiplying the signal, represented in the frequency domain, with the transfer function $G(z,\omega)$.

Multiple DSP algorithms have been proposed to mitigate penalties induced by CD. For example, it has been proposed to design a finite impulse response (FIR) filter to approximate the inverse of the frequency response of chromatic dispersion [53]. The FIR filter can be implemented through a tap-delay line [91]. The filter tap weights are expressed as [53]:

$$g_k = \sqrt{\frac{jcT_s^2}{D\lambda^2 z}}\exp\left(\frac{-j\pi cT_s^2}{D\lambda^2 z}k^2\right) \tag{2.9}$$

where T_s represents the sampling interval. The parameter k is the index for filter tap weights, which is defined as [53]:

$$-\left\lfloor \frac{N}{2} \right\rfloor \leq k \leq \left\lfloor \frac{N}{2} \right\rfloor \quad \text{and} \quad N = 2\left\lfloor \frac{|D|\lambda^2 z}{2cT_s^2} \right\rfloor + 1 \tag{2.10}$$

where the parameter N defines the filter length required for chromatic dispersion compensation (CDC).

It can be seen from Eq.2.10 that filter length N increases proportionally with the transmission distance z and inversely proportional to the square of the sampling period T_s, which indicates that, for a high-speed transmission system over a long distance, the filter length needs to be sufficiently high in order to compensate CD effectively. This leads to a rapid increase in computational complexity due to the linear time-domain convolution for implementing the FIR filter [92, 93]. One approach to reduce the computational cost is to leverage the pulse shaping [94]. Since pulse shaping can effectively reduce the signal bandwidth, the FIR filter length can be designed to cover only the signal bandwidth, rather than the whole frequency band, limited by Nyquist frequency as in Eq. 2.10. Therefore, the FIR filter length, and hence the computational cost, can be reduced.

In contrast to implementing CDC in the time domain using FIR filters, it is possible to perform the equalisation in the frequency domain at a much-reduced calculation complexity thanks to the low calculation complexity of the fast Fourier transform (FFT) as mentioned in Chapter 1. The frequency-domain equaliser (FDE) is implemented by transferring the signal into the frequency domain, multiplying the signal with the inverse of the dispersive link's transfer function $G(z,\omega)$ (Eq.2.8), and then transforming the equalised signal back into the time domain. While the time-domain equalisation is a continuous sample-by-sample process, frequency-domain equalisation is based on block processing where a block of samples are collected and processed together [93]. There are two main categories for implementing block-based frequency-domain (FD) equalisation, known as overlap-add and overlap-save methods. Readers are referred to [63, 95] for detailed analysis and comparison between these two methods, but the general operating

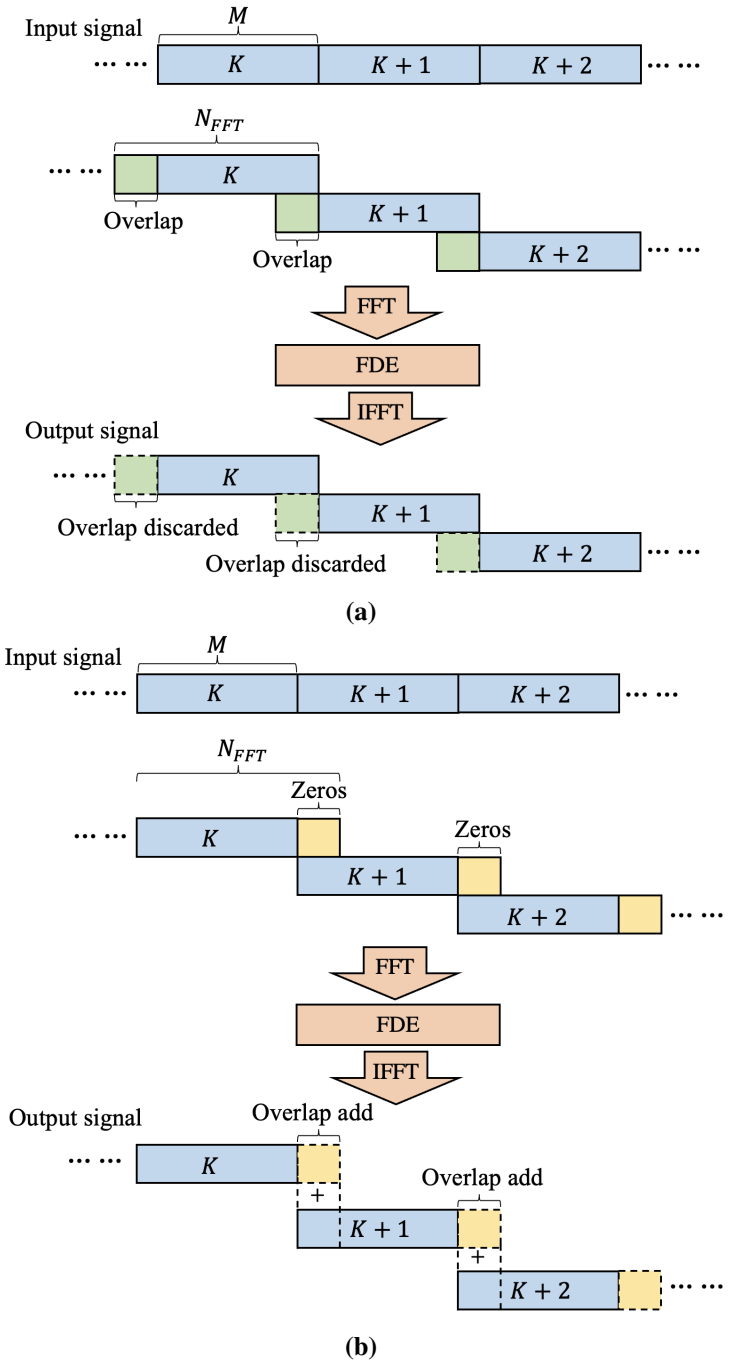

Figure 2.2: Frequency-domain equalisation with (a) overlap-save method and (b) overlap-add method. K is the block index; M denotes the number of useful samples in one block, together with added overlap samples comprising one FFT block with N_{FFT} samples. FFT: fast Fourier transform; IFFT: inverse fast Fourier transform; FDE: frequency-domain equaliser.

principle is shown in Fig. 2.2. Since directly transferring the signal into the frequency domain and multiplying it with the frequency-domain filter response yields a circular convolution after inverse fast Fourier transform (IFFT), a certain overlap should be added to the block of useful samples to form each FFT block. The linear convolution between the input signal and the filter response can be extracted from a subset of the IFFT output samples. Specifically, the overlap-save method divides the signal sequence into multiple blocks with a certain overlap of samples from the previous block while overlap-add method divides the signal sequence into blocks with overlap composed of zeros. After frequency-domain equalisation, the overlap-save method combines the signal in the time domain and discards the overlap samples. In contrast, the overlap-add method adds up the overlap samples. Both methods can achieve similar performance but the overlap-save method has been shown to be more computationally efficient and has been widely adopted for equalisation [50, 96, 97], and hence is employed in the research work presented in this thesis. Its operating principle will be presented in detail in Chapter 3.

The number of overlap samples in the FDE is determined by the pulse broadening induced by chromatic dispersion. Similarly to the FIR filter length in the TDE, the number of overlap samples is critical for performing accurate CDC [98]. The FFT size, on the other hand, is more flexible provided it is longer than the minimum number of overlap samples. Depending on the implementation of FFT algorithms in the field-programmable gate array (FPGA) or application-specific integrated circuit (ASIC), the FFT size can be configured to optimise the calculation complexity and power consumption [93, 96].

In most cases, it is assumed that the amount of CD that is accumulated from the optical fibre is known to the receiver. Therefore, a simple static frequency-domain equalisation is sufficient for CDC as discussed above. However, there are some scenarios in which the chromatic dispersion may vary due to external perturbations such as temperature changes or dynamic light path changes between two nodes in a network. As a result, the receiver may not have prior knowledge of the amount of chromatic dispersion that has accumulated in the link. Several adaptive

equalisation schemes have been proposed to cope with such dynamic chromatic dispersion variations, for instance, using a frequency-domain blind look-up table in which transfer functions for various amounts of dispersion are stored in memory [92]. The equaliser goes through a coarse and then a fine search of dispersion, until a certain error criterion is satisfied. Alternatively, it was proposed to employ an adaptive time-domain least mean square (LMS) equaliser [94, 98]. It is shown to be very robust in dynamic dispersive optical links; however, the computation is rather cumbersome due to the need for multiple iterations and the complex update procedure of the adaptive filter coefficients. In addition, it is possible to combine both time-domain and frequency-domain equaliser together for mitigating chromatic dispersion, which is referred to as a hybrid FD/TD equaliser [99]. The idea behind this algorithm is to apply a frequency-domain equaliser first to compensate the majority of chromatic dispersion, and then employ a small time-domain adaptive equaliser for mitigating residual CD, and time-varying impairments such as polarisation mode dispersion (PMD) and polarisation rotations [97, 100].

It should be noted that in this thesis, the static transmission link is assumed, where the accumulated chromatic dispersion is known to the receiver, and thus, a non-adaptive frequency-domain equaliser is sufficient to achieve accurate chromatic dispersion compensation.

2.1.2 Polarisation mode dispersion and state of polarisation rotation

In contrast to chromatic dispersion, polarisation mode dispersion (PMD) and state of polarisation (SOP) rotations typically vary with time. In the ideal case with cylindrical fibre, the refractive indices for x and y polarisations are identical, as shown in Fig.2.3(a), and thus the two polarisations travel at the same speed in the fibre. However, in reality, the manufacturing imperfections and mechanical stress during fibre fabrication, cabling and deployment result in an unsymmetrical core of the fibre. The fibre refractive indices for the two polarisations are therefore different as shown in Fig.2.3(b). This is known as fibre birefringence [88]. The fibre

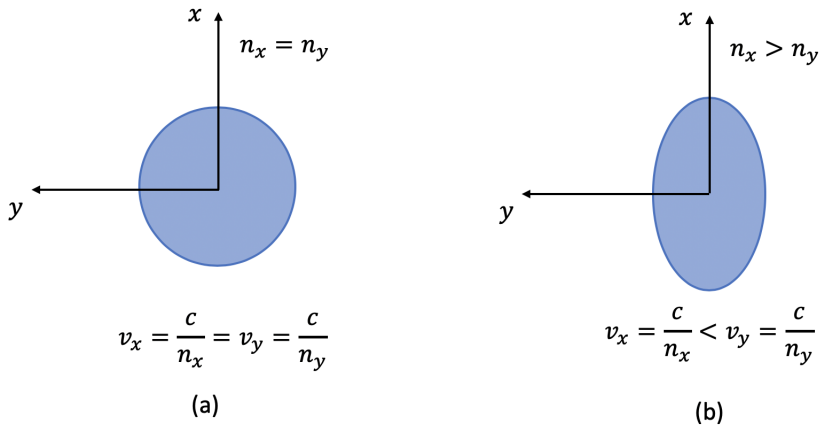

Figure 2.3: (a) The ideal-symmetric fibre with the same refractive index for x and y polarisation; (b) The fibre with non-symmetric core. n_x and n_y denote the refractive indices for the x and y polarisations. v_x and v_y represent the velocities at which the signal travels with the two polarisations. c denotes the speed of light.

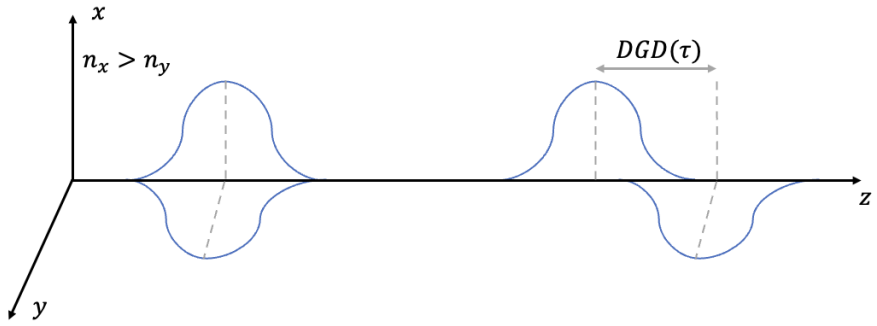

Figure 2.4: Differential group delay (DGD) between x and y polarisation as they propagate along the fibre.

birefringence leads to two orthogonal polarisations travelling at different speeds and with random SOP rotations. At the fibre output, the optical pulse is broadened and the signals on the two polarisations are mixed.

The accumulated time delay τ between the two polarisation modes as they propagate along the fibre is known as differential group delay (DGD) as shown in Fig.2.4 [101]. The measured instantaneous DGD changes in a random manner due to random fibre birefringence, but in general, it can be approximated by a Maxwellian probability distribution [102]. The root-mean-square value of instantaneous DGD is known as the PMD of the fibre, usually measured in ps [88, 102]. Further dividing PMD by the square-root of the fibre length L (km) gives the

PMD coefficient ($\mathrm{ps}/\sqrt{\mathrm{km}}$), and it is usually a specified parameter for commercially available fibres [89, 90]. For most commercial fibres, the PMD parameter is within the range of 0.1 to 1 $\mathrm{ps}/\sqrt{\mathrm{km}}$ [88]. As PMD scales proportionally to $\sqrt{L}$, the impact of induced pulse broadening is relatively small compared to that of CD [103].

The analytical description of PMD is rather complex due to its statistical nature [102]. A numerical model of PMD considers the fibre as a concatenated series of random birefringence sections [103]. For a given section, the fibre birefringence remains constant but varies randomly from section to section. The resulting impact on PMD and SOP rotations between two polarisations due to this random fibre birefingence can be modelled by multiplying the signal with a 2×2 complex matrix, known as the Jones matrix. For section i, the Jones matrix $\mathbf{R}_i$ and $\mathbf{D}_i$ are given by [88]:

$$\mathbf{R}_i = \begin{bmatrix} \cos\theta_i e^{-j\phi_i} & \sin\theta_i \\ -\sin\theta_i & \cos\theta_i e^{j\phi_i} \end{bmatrix} \qquad \mathbf{D}_i = \begin{bmatrix} e^{-j\omega\frac{\tau_i}{2}} & 0 \\ 0 & e^{j\omega\frac{\tau_i}{2}} \end{bmatrix} \tag{2.11}$$

where θ_i and ϕ_i refer to the random rotation and random phase shift between two polarisations, τ_i denotes the local DGD, and ω is the angular frequency. Typically, variables θ_i and ϕ_i follow the uniform distribution between $[-\pi, \pi]$ and $[-\pi/2, \pi/2]$ [88]. Given that the total fibre is modeled by m cascaded sections, the effect of the fibre on the signal can be modelled using the Jones matrix $\mathbf{J} = \mathbf{R}_m\mathbf{D}_m \ldots \mathbf{R}_i\mathbf{D}_i \ldots \mathbf{R}_1\mathbf{D}_1$ [103].

The PMD and SOP rotations are time-varying effects, and an adaptive equaliser is required to undo polarisation rotation and recover the signal. Normally, an adaptive equaliser is composed of three steps [51]. The first step is referred to as filtering, where the digital filter is linearly convolved with the input signal. The next step, known as the error estimation, is to compute the deviation between the desired output and the filter output. The final step is the updating of the filter coefficients by examining the obtained errors from the previous step.

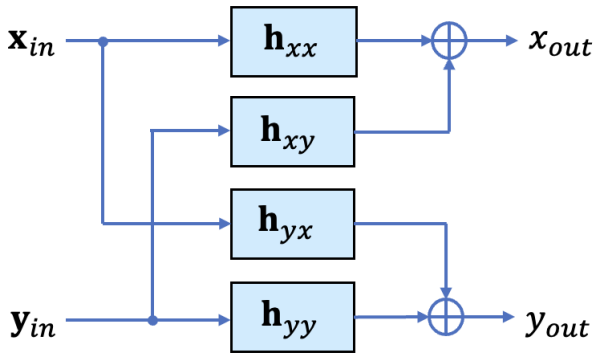

Figure 2.5: Schematic of a 2×2 MIMO equaliser. $\mathbf{x}_{in}$ and $\mathbf{y}_{in}$ denote the input signal vectors for x and y polarisations. $\mathbf{h}_{xx}$, $\mathbf{h}_{xy}$, $\mathbf{h}_{yx}$, $\mathbf{h}_{yy}$ represent the time-domain filter vectors. x_{out} and y_{out} are the output signal samples after equalisation.

With two polarisation modes propagating in the optical fibre, the adaptive equaliser is constructed as a 2×2 multiple-input multiple-output (MIMO), shown in Fig.2.5 [53]. $\mathbf{h}_{xx}$, $\mathbf{h}_{xy}$, $\mathbf{h}_{yx}$, $\mathbf{h}_{yy}$ represent the time-domain filters. Considering the input signal vector $\mathbf{x}_{in}$ and $\mathbf{y}_{in}$ with L samples, the $n-th$ equalised signals for the two polarisations are given by [54]:

$$\begin{aligned} x_{out}(n) &= \mathbf{h}_{xx}^T \mathbf{x}_{in} + \mathbf{h}_{xy}^T \mathbf{y}_{in} \\ y_{out}(n) &= \mathbf{h}_{yx}^T \mathbf{x}_{in} + \mathbf{h}_{yy}^T \mathbf{y}_{in} \end{aligned} \tag{2.12}$$

where T denotes the transpose of the vector. Both input signals and filter coefficients are represented by an L by 1 vector. For instance,

$$\begin{aligned} \mathbf{x}_{in}(n) &= [x_{in}(n),\ x_{in}(n-1),\ \ldots,\ x_{in}(n-L+1)]^T \\ \mathbf{h}_{xx}(n) &= [h_{xx0}(n),\ h_{xx1}(n),\ \ldots,\ h_{xx(L-1)}(n)]^T \end{aligned} \tag{2.13}$$

Similar expressions can be obtained for input signal vector $\mathbf{y}_{in}$, and other filter coefficients.

After filtering, the next step is to calculate the errors. For the modulation format of phase shift keying (PSK) where all symbols lie on the same ring in the constellation (i.e., having a constant radius of 1), the constant modulus algorithm (CMA) is often employed to calculate the deviation of the equalised sample from the constant radius [104, 105]. For higher-order modulation formats, such as

	Error estimation
CMA	$e_x(n) = 1 - \lvert x_{out}(n)\rvert^2$ $e_y(n) = 1 - \lvert y_{out}(n)\rvert^2$
RDE	$e_x(n) = R_x^2 - \lvert x_{out}(n)\rvert^2$ $e_y(n) = R_y^2 - \lvert y_{out}(n)\rvert^2$
DD-LMS	$e_x(n) = \hat{x_{out}}(n) - x_{out}(n)$ $e_y(n) = \hat{y_{out}}(n) - y_{out}(n)$

Table 2.1: Error estimation in adaptive equalisers [53]. CMA: constant modulus algorithm; RDE: radially-directed equalise; DD-LMS: decision-directed least mean square. n is the sample index. $e_x(n)$ and $e_y(n)$ denote the estimated errors for x and y polarisations respectively. x_{out} and y_{out} are the output signal samples after equalisation. R_x and R_y represent the nearest constellation radii for x_{out} and y_{out}. $\hat{x_{out}}(n)$ and $\hat{y_{out}}(n)$ denote the symbols that are closest to the equaliser output after decision.

M-ary quadrature amplitude modulation (QAM) where the different symbols have a variety of amplitudes, the deviation is obtained by subtracting the filter output from its nearest constellation ring. This algorithm is known as radially-directed equaliser (RDE) [106]. Alternatively, instead of bringing the received symbol to the closest radius, the receiver can also directly make hard decisions on equalised symbols, known as decision-directed least mean square (DD-LMS) algorithm. It should be noted that, in contrast to CMA or RDE, DD-LMS is very sensitive to laser phase noise as it makes an estimate of what the transmitted symbol might be after adaptive equalisation [57]. Hence, DD-LMS often requires an accurate carrier phase recovery before equalisation to eliminate the penalty from laser phase noise (e.g., through the use pilot symbols [107]). Otherwise, it might lead to unstable operation. In many cases of using higher-order modulation schemes, CMA is often chosen for pre-convergence before switching to RDE or DD-LMS for more accurate error estimation [108]. The error calculations for these three methods are summarised in Table 2.1.

The objective of the adaptive equalisation is essentially to minimise the mean squared error (MSE) $E[\lvert e(n)\rvert^2]$, which is also referred to as the cost

function [105]. As the cost function is related to adaptive filter coefficients (see Eq.2.12 and Table 2.1), minimising the errors requires searching for the optimum filter coefficients. Employing the stochastic gradient descent algorithm by taking the instantaneous value of the gradient (i.e., replacing $E[|e(n)|^2]$ by $|e(n)|^2$), the cost function can be minimised by setting the partial derivative of $|e(n)|^2$ with respect to every filter tap weight (see Eq. 2.13) to zero, given by [51]:

$$\frac{\partial |e(n)|^2}{\partial h_i(n)} = 0, \quad \text{where} \quad 0 \leq i \leq L-1 \tag{2.14}$$

where i denotes the index for each individual filter tap weight in the filter coefficient vector $\mathbf{h}(n)$. Collectively, Eq.2.14 can be written as [51]:

$$\nabla_{\mathbf{h}} |e(n)|^2 = 0 \tag{2.15}$$

where $\nabla_{\mathbf{h}}$ denotes the gradient operator with respect to filter coefficient vector $\mathbf{h}(n)$. The obtained gradient is then used to update the adaptive filter tap weights given by [51]:

$$\mathbf{h}(n+1) = \mathbf{h}(n) - \mu \nabla_{\mathbf{h}} |e(n)|^2 \tag{2.16}$$

where μ is the convergence parameter which determines the convergence rate of the equaliser, also known as the step size.

Employing CMA or RDE as the cost function, the equations for updating the four sets of filter taps are given by [54, 105]:

$$\begin{aligned}
\mathbf{h}_{xx}(n+1) &= \mathbf{h}_{xx}(n) + \mu e_x(n) x_{out}(n) \mathbf{x}_{in}^*(n) \\
\mathbf{h}_{xy}(n+1) &= \mathbf{h}_{xy}(n) + \mu e_x(n) x_{out}(n) \mathbf{y}_{in}^*(n) \\
\mathbf{h}_{yx}(n+1) &= \mathbf{h}_{yx}(n) + \mu e_y(n) y_{out}(n) \mathbf{x}_{in}^*(n) \\
\mathbf{h}_{yy}(n+1) &= \mathbf{h}_{yy}(n) + \mu e_y(n) y_{out}(n) \mathbf{y}_{in}^*(n)
\end{aligned} \tag{2.17}$$

where the asterisk denotes the complex conjugate. Similarly, the filter update in the

case of DD-LMS is calculated as [53]:

$$\begin{aligned}
\mathbf{h}_{xx}(n+1) &= \mathbf{h}_{xx}(n) + \mu e_x(n)\mathbf{x}_{in}^*(n) \\
\mathbf{h}_{xy}(n+1) &= \mathbf{h}_{xy}(n) + \mu e_x(n)\mathbf{y}_{in}^*(n) \\
\mathbf{h}_{yx}(n+1) &= \mathbf{h}_{yx}(n) + \mu e_y(n)\mathbf{x}_{in}^*(n) \\
\mathbf{h}_{yy}(n+1) &= \mathbf{h}_{yy}(n) + \mu e_y(n)\mathbf{y}_{in}^*(n)
\end{aligned} \tag{2.18}$$

The most complex step in these 3-step adaptive equalisation methods is the filter coefficients update, which accounts for almost half of the calculation complexity of the algorithm itself. A few techniques for reducing the calculation complexity in the filter update have been investigated in [52]. In particular, the proposed multiplier-free tap weight update algorithm is shown to significantly reduce the complexity since multiplications are usually more computationally intensive than additions. In the experimental verification of 3 Gbaud polarisation-division multiplexing (PDM)-quadrature phase shift keying (QPSK) system in transmission over 100 km SSMF, it was shown to be capable of achieving similar performance to that of using the conventional filter update algorithm. Alternatively, one can reduce the filter length via sample pruning [59]. Normally, the adaptive equaliser is performed at two samples per symbol. Using sample pruning, the input signal to the adaptive equaliser is downsampled to one sample per symbol and calculations are only performed for the required samples for the output symbols. In the simulation, the sample pruning method was shown to offer a greater than 50% reduction in power dissipation in a 28 nm ASIC implementation. Such a reduction is achieved at the expense of a small penalty on the equaliser's tracking ability due to a noiser gradient estimation.

Similarly to FD CDC discussed in the last section, the adaptive time-domain equaliser can also be implemented in the frequency domain to reduce the calculation complexity and power consumption [63]. In [60], an adaptive FDE comprised of two sub-equalisers for odd and even samples was evaluated in a 40 Gbit/s dual polarisation QPSK system. The performance is shown to be equivalent to TDE but with reduced computation cost. In particular, a constrained gradient estimation

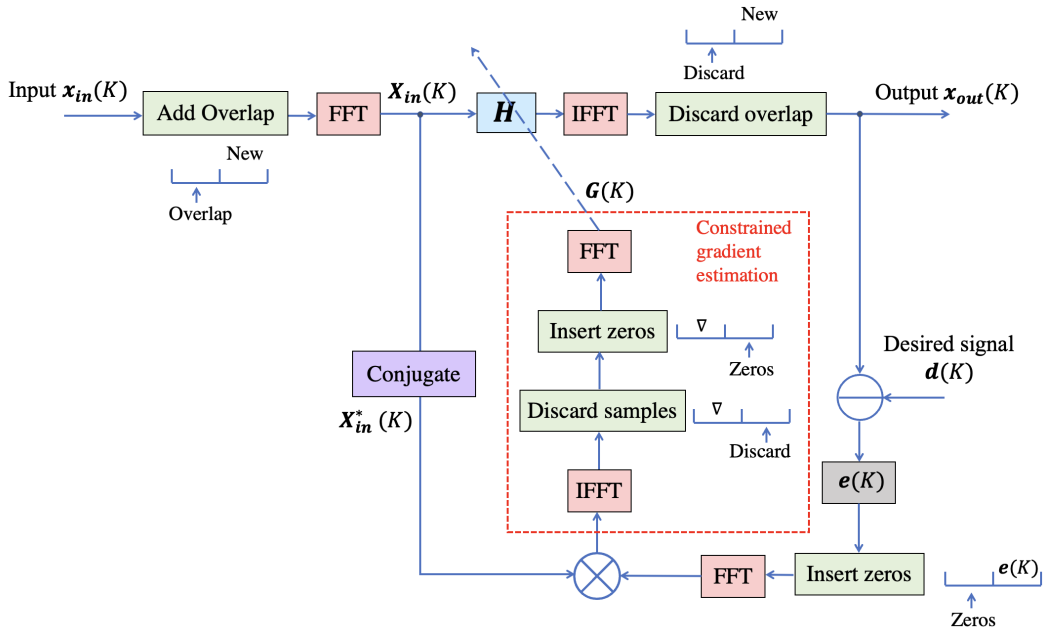

Figure 2.6: Schematic of adaptive frequency-domain equalisation with constrained gradient estimation based on overlap-save method. The red-dash box displays the implementation of constrained gradient estimation [63]. $\mathbf{x}_{in}(K)$ and $\mathbf{X}_{in}(K)$ represent the time-domain and frequency-domain input signal vector respectively. $\mathbf{H}$ denotes the frequency-domain filter coefficients. $\mathbf{x}_{out}(K)$ is the time-domain output signal after equalisation. $\mathbf{d}(K)$ and $\mathbf{e}(K)$ are the time-domain desired signal vector and error vector respectively. $\mathbf{G}(K)$ is the frequency-domain gradient vector. ∇ denotes the gradient.

is employed in the proposed FDE [60, 63]. A schematic of the overlap-save method-based adaptive frequency-domain equalisation with constrained gradient estimation is shown in Fig.2.6. As with the static frequency-domain equalisation shown in Fig.2.2(a), the adaptive FDE also requires a block of samples ($\mathbf{x}_{in}(K)$ as shown in Fig.2.6) added with certain overlaps to be converted to the frequency domain first ($\mathbf{X}_{in}(K)$). Following this, the frequency-domain equalisation ($\mathbf{H}$) is performed and the signal is then transformed back to the time domain to obtain the equalised output signal ($\mathbf{x}_{out}(K)$). The main difference compared to the static FDE is that the adaptive FDE involves two more steps for calculating errors ($\mathbf{e}(K)$) and updating the adaptive filter coefficients using the obtained $\mathbf{G}(K)$. The red-dash box displays the implementation of constrained gradient estimation where a time-domain constraint is imposed on the frequency-domain gradient vector by converting it back to the time domain, discarding the last set of samples of the

gradient vector and padding the same number of zeros before converting it back to the frequency domain again for updating filter coefficients [63]. This time-domain constraint is imposed to ensure that the calculated frequency-domain gradient vector is the result of a correct linear correlation between the error signal and the input signal vector [63].

It can be seen that constrained gradient estimation used in adaptive frequency-domain equalisation adds some computational complexity to the feedback loop in the filter update. Compared to a static (i.e., non-adaptive) FDE used in CDC, the adaptive FDE with constrained gradient estimation for mitigating PMD and SOP rotations in one polarisation increases the computation complexity by 250 % (five more FFTs/IFFTs, with four from constrained gradient estimation since equalising one polarisation involves two adaptive filter coefficient updates, and one from error calculation). It is possible to reduce the computation complexity by omitting the time-domain constraint and hence saving four FFTs/IFFTs for recovering one polarisation [109]. This approach is known as unconstrained gradient descent algorithm [63]. In this case, the calculation complexity increases by only 50 % compared to the static FDE. Nonetheless, this comes with small penalties in the performance of the adaptive equaliser as demonstrated in [110]. Therefore, the constrained gradient descent estimation has also been adopted for the research work presented in Chapter 3.

The above-mentioned adaptive equalisation algorithms are all blind, which means that the receiver has no knowledge of what signal has been transmitted. In some situations, it might be challenging for the blind adaptive equaliser to converge quickly and to be able to track dynamic effects. For example, the rapid SOP rotations caused by lightning strikes on aerial fibres can lead to rapid SOP rotations at the order of a few Mrad/s [67–69]. These fast changes of SOP rotations make it almost impossible for most commercial DSPs in polarisation multiplexed transmission systems to successfully de-multiplex the signal as the adaptive equaliser is only capable of tracking SOP rotations at rates of up to a few hundred krad/s [65, 111]. Hence, a number of studies explored the possibility of

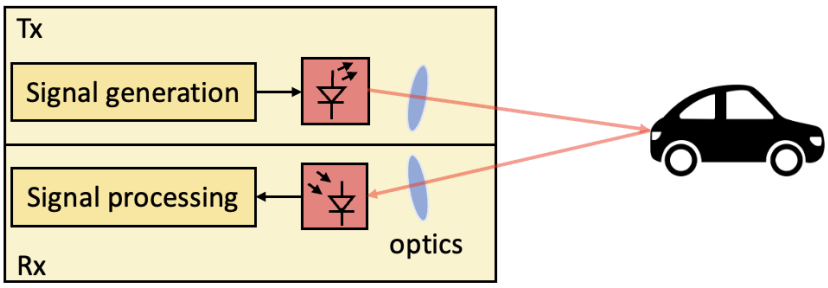

Figure 2.7: Overview of a LiDAR system. Tx: transmitter; Rx: receiver.

training-based feed-forward equalisation technique where part of the transmitted signal is known to the receiver [65, 112]. In this case, pilot symbols are inserted periodically. Comparing transmitted and received pilot symbols, the inverse of the Jones matrix of the optical channel can be obtained without the filter update process. Moreover, in [113], it was proposed to update the adaptive equaliser only based on pilot symbols. The filter coefficients were then kept constant for the following payload until the next pilot symbol. This type of feed-forward equalisation is shown to have a faster convergence speed than blind equalisation and is capable of tracking higher-speed SOP rotations. Nonetheless, the insertion of training or pilot symbols will inevitably add a certain overhead [56].

2.2 LiDAR architecture

Fig.2.7 shows an overview of a typical LiDAR system. It consists of a transmitter generating a modulated LiDAR signal. The signal is then collimated and illuminates the target. After being reflected back from the target, the signal is focused onto the photodiode for detection [114]. Signal processing is applied to the detected signal to extract the range and velocity information. Fig.2.8 shows three types of LiDAR that can be applied for ranging, known as pulsed time-of-flight (ToF) LiDAR, amplitude-modulated continuous-wave (AMCW) LiDAR and frequency-modulated continuous-wave (FMCW) LiDAR. While the pulsed TOF LiDAR directly measures the distance to the target by measuring the time delay, AMCW LiDAR and FMCW LiDAR encode the distance information into phase shift and beat frequency respectively.

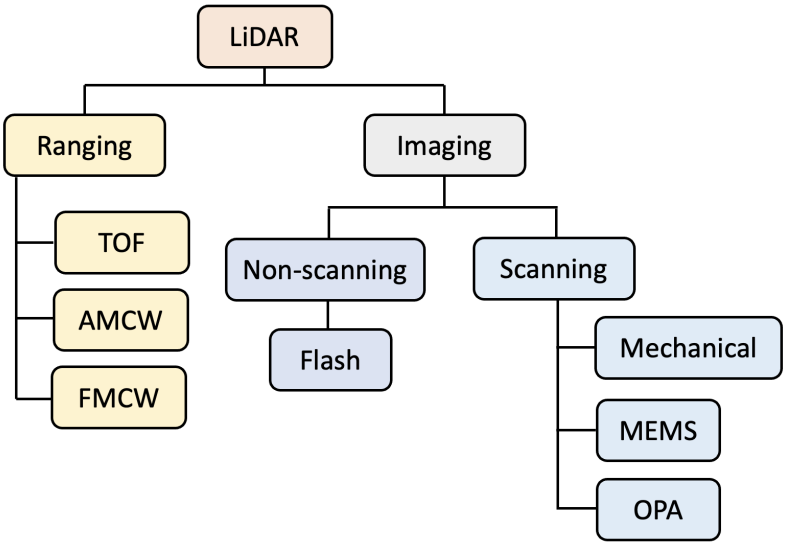

Figure 2.8: LiDAR sub-systems. ToF: time-of-flight; AMCW: amplitude-modulated continuous-wave; FMCW: frequency-modulated continuous-wave; MEMS: micro-electromechanical system; OPA: optical phased array.

The main advantage of LiDAR over conventionally remote sensing techniques such as radio detection and ranging (Radar) is its ability to generate a high-resolution 3D point cloud. This imaging ability can be realised through a non-scanning approach, for instance flashing the entire field-of-view (FOV) simultaneously, or various beam scanning techniques as shown in Fig.2.8. The working principle of flash LiDAR is very similar to the flash light used in camera. The entire FOV of interest is illuminated at once, and all the reflections are received by a detector matrix at the receiver [45, 115]. Since the entire scene is measured at once, this approach enables faster data acquisition and is more resistant to vibrations and movements when taking the measurements. On the other hand, as the light is dispersed in all directions in the flash LiDAR, this approach significantly reduces the signal optical power and thus constrains the ranging distance to tens of meters [46].

To extend the ranging distance, a focused beam can be used instead, concentrating light at one point and generating one pixel at a time. The entire FOV is then scanned sequentially. This method is referred to as beam scanning. A number of techniques have been developed to achieve beam scanning, e.g.,

mechanical beam steering technique [116], optical phased array (OPA) [84, 117], micro-electromechanical system (MEMS) mirrors [118] and so forth. Mechanical beam scanning includes a galvanometer-driven mirror, to rotate the beam to different angles. It usually works in combination with pulsed TOF LiDAR system and is currently prevalent in the automotive industry, with leading sensor providers such as Velodyne, Ouster and Hesai [42, 119]. Despite its popularity, such system still presents a few drawbacks. First, it is usually very bulky and power hungry, and the inertia of the rotating module limits the scanning speed to 100 Hz [46]. Besides, the system is very susceptible to vibrations which might lead to misalignment and raise questions about their long-term reliability.

The other two beam scanning techniques, namely MEMS mirrors and OPAs, have received growing research and industrial interest in recent years and have proven to be appealing alternatives to mechanical beam steering [85, 114, 119]. MEMS systems replace external rotating mirrors with micromirrors to adjust the direction of the incoming light. These micromirrors with diameters of just a few millimeters are tilted to different angles in response to the stimulus such as electrostatic, electromagnetic or piezoelectric [120]. MEMS beam steering systems tend to be compact and have a low power consumption. However, as the system still involves moving components, it is sensitive to shocks and vibrations.

The OPA is the alternative solid-state beam steering technique, consisting of multiple phase modulators to adjust the delay of the light as it travels through phase modulators. The constructive and destructive interference of the light emerging from the phase modulators changes the optical wave-front shape and hence the beam steering angle [85]. Combined with integrated photonic circuits, OPAs have the potential to achieve a chip-scale system. The main drawback of OPAs is their high insertion loss of the laser power, limiting the transmitter's maximum emission power and hence the ranging distance [42, 84]. As both flash LiDAR and beam scanning LiDAR come with their own features and shortcomings when in use to generate a 3D representation of the environment, hybrid approaches to combine the strength of each are being explored and many other emerging scanning techniques

are under development to potentially provide better optical sensing performance and reliability [42].

After the LiDAR signal has been generated and directed at the target, the back-scattered signal needs to be detected and processed at the receiver. In the flash LiDAR, a detector matrix is used to collect all the light reflected back from the FOV of interest with each detector corresponding to one pixel [46]. In terms of beam scanning where a single point is measured at a time, it is possible to use detector arrays, each responsible for a certain direction, in order to accelerate the data acquisition speed [82].

In the following sections, the operating principles of three optical sensing techniques, i.e., the pulsed TOF LiDAR, AMCW LiDAR and FMCW LiDAR, are presented in Sec. 2.2.1, 2.2.2 and 2.2.3 respectively. The unique strengths and drawbacks of each, and the system trade-offs are discussed. As coherent FMCW LiDAR was investigated in the research work presented in Chapter 4, its operating principle and related literature, including various signal generation techniques, detection mechanisms, are reviewed in more detail. Readers are referred to [121–124] for more comprehensive discussions on pulsed TOF LiDAR and AMCW LiDAR. Section 2.2.4 presents a summary and comparison of these three LiDAR techniques.

2.2.1 Pulsed time-of-flight (TOF) LiDAR

The pulsed TOF LiDAR is the most-commonly used type of laser range finder and currently prevails in the LiDAR market due to its simple modulation principle and low-cost, low-complexity architecture [125]. It directly measures the time delay τ between the emission and the arrival of the optical pulse after being reflected back by the target as shown in Fig.2.9. Hence, the target distance L can be obtained by multiplying this time difference τ and the speed of light in the air c given by:

$$L = \frac{c\tau}{2} \tag{2.19}$$

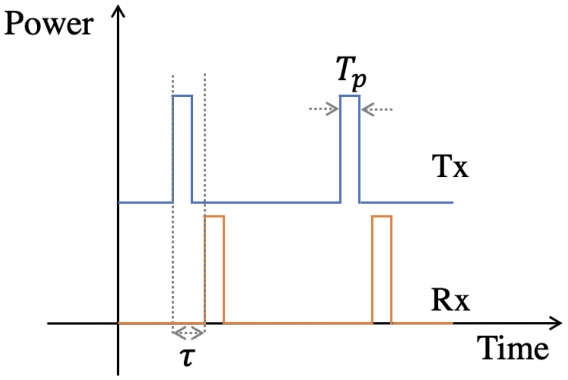

Figure 2.9: Schematic for pulsed TOF LiDAR.

The factor of two maps the round-trip delay to one-way distance. In practice, this time delay is often measured by a high-speed and high-precision timing discriminator. The start of the emission pulse triggers the timer and the back-reflected pulse stops it [126]. In practice, the jitter of the timing circuit, variation of the pulse shape and amplitude due to transmission together with other typical noise sources such as electronics, shot noise, background noise, will affect the precision of timing, hence impacting the ranging precision [77].

Ranging resolution is another important parameter which determines a LiDAR's ability to differentiate two closely located targets in space. A higher resolution is desirable as it captures more details when generating a 3D point cloud. In the TOF LiDAR, the ranging resolution is related to the pulse duration T_p, given by [127]:

$$R_{res} = \frac{cT_p}{2} \tag{2.20}$$

Therefore, a shorter pulse can provide a finer ranging resolution. A typical pulse duration of a few nanoseconds enables a ranging resolution of tens of centimeters (e.g., 5 ns pulse gives a ranging resolution of 0.75 m) [128].

Another important system metric is the maximum ranging distance. In the TOF LiDAR, if the timing interval of the timing discriminator is sufficiently long, the maximum ranging distance is limited by the following factors. First, the ambiguity distance which refers to the scenario that the echo of the first pulse returns after the emission of the second pulse. This causes ambiguity of identifying the correct time

delay and thus induces errors in the distance measurement. The longest distance the pulse can travel without inducing aliasing from other pulses is known as the maximum unambiguous range [129]. It is obvious that the unambiguous range is associated with the pulse repetition rate. The higher the pulse repetition rate, the shorter the unambiguous range. In addition, the optical power of the pulse is critical in defining the maximum ranging distance. Under the condition that the eye-safety requirement is always met, the pulsed LiDAR can be operated at a shorter pulse duration of a few nanoseconds or even picoseconds to increase the optical peak power [77]. The high optical peak power offsets the loss in free space when travelling long distances. The corresponding system trade-off is the increase of the required receiver bandwidth ($\propto 1/T_p$), introducing more noise into the system, and thus degrading the signal-to-noise ratio (SNR) [127, 129]. The constant high-peak-power operation may also cause damage to the laser source, potentially reducing its lifetime [77].

Apart from sending shorter pulses to increase the optical peak power at the transmitter, one can also use highly-sensitive detectors at the receiver, for instance, the single-photon avalanche detector (APD) [130], to improve its ability of successfully detecting weak signals. APDs normally operate in the reverse-bias mode (Geiger mode), under which a single photon can generate an electron-hole pair that triggers the avalanche process and leads to a large current [45]. The large amplitude of the current triggers the timing circuit. Nonetheless, the APDs are very susceptible to ambient light and scattering and may cause false detections [45, 115].

As mentioned earlier, TOF LiDAR prevails in the current LiDAR market. Most commercial TOF LiDAR systems work at 905 nm, as pulsed diode lasers are readily available at a low cost, as are the photodetectors. In addition, this wavelength range is within the detection range of silicon, so it is compatible with complementary metal-oxide semiconductor (CMOS) techniques [42, 47]. The main drawback associated with this wavelength is the eye-safety issue. As light with the wavelength of 905 nm can penetrate human eyes and reach the retina, the maximum emission power needs to be kept low which limits its ranging distance to tens of meters [44].

Nowadays, most commercially available products can achieve a ranging resolution and precision of a few centimeters at these distances [121, 131–133].

In addition to applications in range-finding, the pulsed TOF LiDAR has also been used for anemometry to detect the wind velocity [134]. Such detection technique is also referred to as Doppler Wind LiDAR, in which the light is backscattered by aerosols and introduces a Doppler frequency on the carrier frequency [135]. In contrast to the direct detection scheme used in ranging, coherent detection is required in anemometry in order to resolve the Doppler ambiguity [40]. At the receiver, by mixing the Rx signal with the local oscillator (LO) and applying the Fourier transform after digitisation, a Doppler frequency can be found through a peak search [134]. The radial velocity v_r can be determined from the identified Doppler frequency f_d by [134]:

$$v_r = \frac{c}{2f_c} f_d \tag{2.21}$$

where f_c is the carrier frequency. The velocity resolution is defined as [134]:

$$v_{res} = \frac{c}{2f_c T_p} \tag{2.22}$$

As T_p refers to the pulse duration as shown in Fig.2.9, Eq.2.22 suggests that a longer pulse duration enables a better velocity resolution. On the other hand, a shorter pulse duration offers a finer ranging resolution as shown in Eq.2.20. The selection of pulse duration involves the trade-off between range and velocity resolution in the Doppler Wind LiDAR [81].

2.2.2 Amplitude-modulated continuous-wave (AMCW) LiDAR

In AMCW LiDAR, the light intensity is modulated by a sinusoidal wave of frequency f_m [45]. The target distance information is extracted by measuring the relative phase shift $\Delta\Phi$ between the backscattered Rx signal and the reference signal as displayed in Fig.2.10 [46]. Therefore, this method is also known as phase measurement [77] or continuous wave intensity modulation [136].

There are a number of techniques to extract this phase shift. One approach

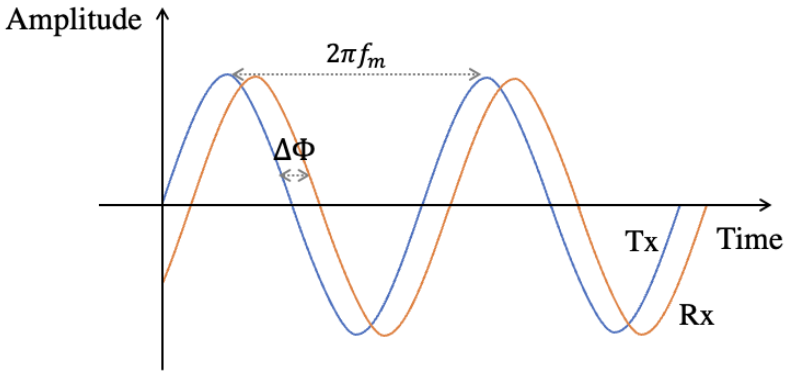

Figure 2.10: Schematic for AMCW LiDAR.

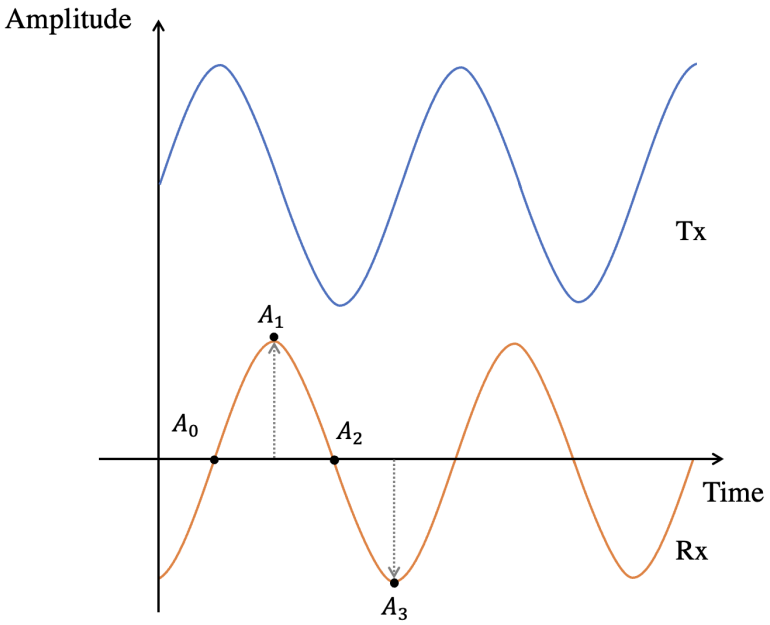

Figure 2.11: Measurement of phase shift in the AMCW LiDAR with 'four-bucket' sampling [124].

is to use the amplitude of the Rx signal as shown in Fig.2.11. By measuring the amplitude at four equally spaced offsets of 90°, the phase shift $\Delta\Phi$ can be calculated by [124, 137]:

$$\Delta\Phi = \arctan\left(\frac{A_3 - A_1}{A_0 - A_2}\right) \tag{2.23}$$

where A_0, A_1, A_2 and A_3 denote the measured amplitudes. As the Rx signal is sampled at four points in each modulation cycle, this phase demodulation method is also known as 'four-bucket' sampling [124].

Alternatively, one can use mixers and low-pass filters to remove the modulation

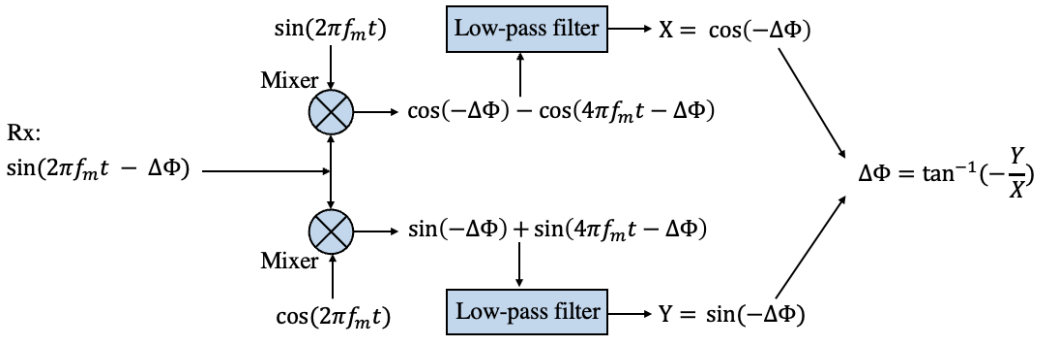

Figure 2.12: Measurement of phase shift in the AMCW LiDAR using mixers and low-pass filters [138].

frequency and then filter out the desired phase change that is associated with the target distance as shown in Fig.2.12. Nonetheless, this technique involves rather complex circuitry for implementing mixers and low-pass filters [138].

With the phase shift $\Delta\Phi$ being measured, the round-trip delay can be obtained through [126]:

$$\Delta\Phi = 2\pi f_m \tau \tag{2.24}$$

where the time delay $\tau = \frac{2L}{c}$. Hence, the target distance L is described as [126]:

$$L = \frac{c\Delta\Phi}{4\pi f_m} \tag{2.25}$$

The ranging resolution of AMCW LiDAR varies inversely proportional to the modulation frequency f_m [139]. A higher modulation frequency leads to a better ranging resolution [140]. The maximum unambiguous ranging distance in the AMCW LiDAR is limited by the 2π phase shift due to the periodicity of the modulated signal (i.e., $L_{max} = \frac{c}{2f_m}$) [77, 138]. As the signal modulation frequency increases to improve the resolution, the ranging distance decreases accordingly. Normally, the modulation frequency f_m is of a few tens of MHz, allowing a maximum ranging distance of a few meters and a resolution of a few centimeters [124, 141].

AMCW LiDAR has been used in products since the 1990s and is often referred to as TOF cameras with parallel arrays of emitters and detectors [124]. Numerous

studies have been carried out on the design of low-cost TOF cameras using complementary metal-oxide semiconductor (CMOS) pixel array with an active modulated light source [142–144]. In contrast to pulsed TOF LiDAR or FMCW LiDAR which normally use lasers as the light source, AWCW LiDAR more often uses near-infrared light-emitting diodes (LEDs) with wavelength around 630 nm - 950 nm [141, 145]. The non-concentrated light emitted by LEDs, in addition to the finite unambiguous range limited by 2π phase shift, constrains the AMCW LiDAR to short-distance applications (normally below 10 m), mostly indoors such as video gaming and robotics [45, 122, 136]. Currently, ranging resolution of a few centimeters and precision at $\sim$cm or $\sim$mm level have been achieved in commercial TOF cameras [141, 142, 144, 146].

2.2.3 Frequency-modulated continuous-wave (FMCW) LiDAR

Both pulsed ToF LiDAR and AMCW LiDAR are intensity modulated as discussed above. Frequency-modulated chirp signal, more commonly known as frequency-modulated continuous-wave (FMCW), employs frequency modulation of the lightwave while keeping its amplitude constant [45]. The operating principle of FMCW LiDAR is based on the interference between the reference signal and the back-reflected signal, generating a beat frequency that varies proportionally to the target distance.

The sawtooth waveform of the optical frequency, which is commonly used for ranging in the FMCW LiDAR systems is shown in Fig.2.13. The instantaneous frequency starts from f_1 and linearly increases over the modulation period of T_m with a chirping bandwidth of B. It can be mathematically described as:

$$\cos(\varphi(t)) = \cos\left(2\pi f_1 t + \frac{\pi B t^2}{T_m}\right) \tag{2.26}$$

where $\varphi(t)$ denotes the phase of the chirp signal, and t is the time instance. The back-reflected signal is time delayed by τ, and beats with the reference signal at the

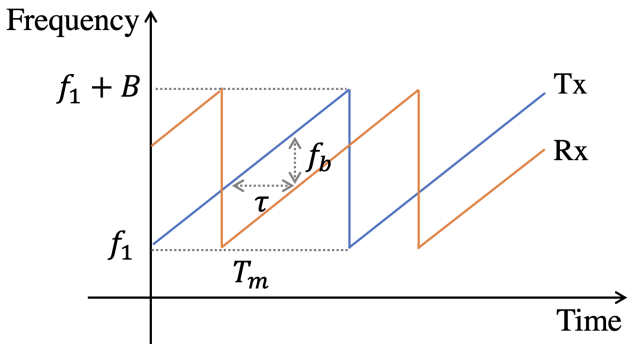

Figure 2.13: Schematic for FMCW LiDAR using a sawtooth chirp waveform.

receiver, producing a beat frequency f_b:

$$\cos(\varphi(t) - \varphi(t-\tau)) = \cos\left(2\pi f_b t + 2\pi f_1 \tau - \frac{\pi B}{T_m}\tau^2\right) \tag{2.27}$$

where $f_b = \frac{B\tau}{T_m}$. In Eq. 2.27, while the last two terms are of constant values, the first term is associated with time t and varies proportionally with time delay τ. Usually, the beat frequency is identified by a peak search in the frequency domain after taking the Fourier transform of the detected beat signal (i.e., applying Fourier transform to Eq.2.27). By detecting f_b, the one-way ranging distance can be obtained:

$$L = \frac{cT_m}{2B} f_b \tag{2.28}$$

This sawtooth chirp signal has been used in the research work presented in Chapter 4 and Chapter 5 for laser ranging. Detailed derivations regarding the modulation of the chirp signal and the detection of the beat frequency can be found in Chapter 4.

In the presence of a moving target, the Doppler frequency f_d will be superimposed onto the distance-dependent beat frequency f_b, introducing errors in the distance measurement. Hence, in this case, the sawtooth waveform is no longer suitable. Triangular frequency modulation can be utilised instead to resolve the distance and velocity ambiguity as shown in Fig.2.14. Two beat frequencies, f_{up} and f_{down}, are measured separately from the upward and downward ramps. While the Doppler frequency f_d is one half of the frequency difference between f_{up} and

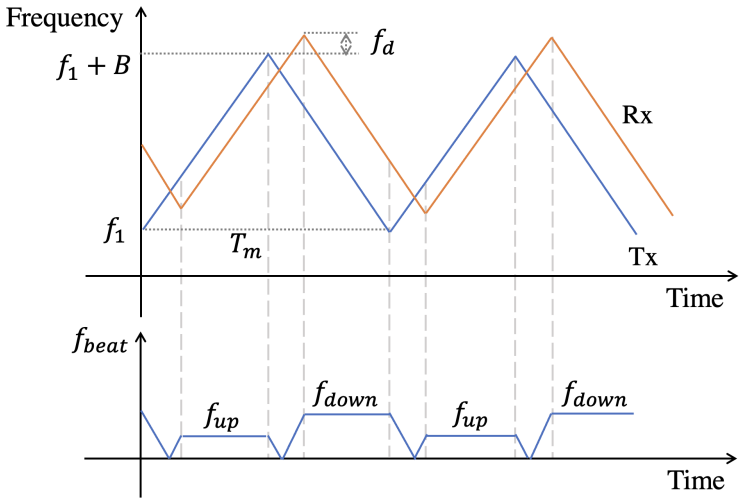

Figure 2.14: Schematic for FMCW LiDAR using a triangular waveform.

f_{down}, distance-dependent beat frequency f_b is the average of the two [147]:

$$\begin{aligned} f_d &= \frac{1}{2}|f_{up} - f_{down}| \\ f_b &= \frac{1}{2}|f_{up} + f_{down}| \end{aligned} \tag{2.29}$$

The target distance and radial velocity are related to f_b and f_d by [147]:

$$\begin{aligned} L &= \frac{cT_m}{4B} f_b \\ v &= \frac{c}{2f_c} f_d \end{aligned} \tag{2.30}$$

The same notations as before are used. c denotes the speed of light, T_m is the modulation period, B is the chirping bandwidth, f_c represents the transmitter laser carrier frequency. The direction of the velocity is estimated by comparing the relative frequency at the upward and downward ramp. For the positive Doppler frequency with the target moving closer, f_{up} obtained with the upward ramp is smaller than f_{down} measured with the downward ramp (i.e., $f_{up} < f_{down}$) as shown in Fig.2.14. Conversely, if the target is moving away, producing a negative Doppler frequency, then $f_{up} > f_{down}$.

The maximum unambiguous range in the case of a sawtooth waveform corresponds to half of the modulation period. Otherwise, the second beating tone

caused by the discontinuity of the sawtooth waveform will introduce errors [148]. In addition to the modulation period which sets a limit on the ranging distance, the laser coherence length plays a major role as well. It is commonly assumed that the reference beam and the time-delayed beam due to the back-reflection from the target should be within the laser coherence length [75, 77]. When operating beyond the laser coherence length, the laser phase noise causes certain spectral broadening in the frequency domain, and therefore, the distance measurement precision is degraded. The laser coherence length L_{coh} is normally defined as the inverse of the laser linewidth given by [75]:

$$L_{coh} = \frac{c}{\pi \Delta v} \tag{2.31}$$

where Δv is the laser linewidth. Therefore, a narrower laser linewidth is beneficial for long-distance ranging.

The ranging resolution of FMCW LiDAR is related to the chirping bandwidth. Taking a single signal period, the Fourier transform-limited ranging resolution is defined as [76]:

$$\Delta r = \frac{c}{2B} \tag{2.32}$$

where c denotes the speed-of-light and B is the chirping bandwidth. Hence, it is usually desirable to have a large chirping bandwidth in order to achieve a higher resolution. The simplest approach to generate such a wide-bandwidth frequency-modulated chirp signal is to directly modulate the laser [71, 72]. Commercially available directly modulated laser (DML) such as vertical-cavity surface-emitting laser (VCSEL) can offer over THz level modulation bandwidth, enabling a ranging resolution of a few micrometers [35, 73, 74, 149]. Distributed feedback (DFB) lasers, can achieve a slightly lower tuning bandwidth, usually of a few hundred GHz [73, 116]. A few techniques have been proposed in the literature to increase the total modulation bandwidth of DFB lasers. For instance, it was proposed to spectrally stitch the optical spectrum of multiple laser sources, e.g., using DFB arrays to replicate a single wide frequency scan, capable of achieving

a $\sim$ µm scale ranging resolution [73, 150]. The main challenge of implementing such coherent stitching of multiple uncorrelated laser sources is to ensure the phase continuity across the sweep, which usually requires an external reference signal and thus slightly complicates the system.

Though widely tunable lasers can enhance the ranging resolution, they often suffer from greater laser phase noise. Laser phase noise is the broadband stochastic frequency noise, normally caused by intrinsic spontaneous emission noise and 1/f noise caused by fluctuations in the laser cavity and noise from the driving circuits [151]. This will lead to an increased laser linewidth [45, 75]. As discussed earlier, a high laser linewidth limits the ranging distance in coherent FMCW LiDAR systems. Using DFB lasers for example, typically with $\sim$1 MHz linewidth, limits the maximum ranging distance to tens of meters [75].

In this case of directly modulating the laser to generate the FMCW LiDAR signal, the trade-off between modulation bandwidth and laser phase noise (and consequently the raging resolution and ranging distance) becomes a fundamental issue. Besides, generating a perfect linear chirp using a tunable laser is challenging due to the inherent nonlinear relation between the output frequency and the driving waveform. A linearisation technique is often required to optimise the signal waveform [77, 78]. For example, this can be implemented by using an iterative learning pre-distortion circuit which predistorts the laser driving waveform in order to obtain a linear frequency modulation [76]. Nonetheless, this pre-estimated driving waveform is susceptible to external changes, e.g., temperature variations, and needs to be updated accordingly. To alleviate this environmental dependence, it was proposed to use a femtosecond fibre laser to generate the frequency comb as a reference [152]. The modulation rate of the tunable laser is then measured against the comb's repetition rate simultaneously with the LiDAR signal to suppress environmental influence.

An alternative approach to generate the linear frequency-modulated chirp signal is to use an external modulator. Though the modulation bandwidth offered by external modulators are usually tens of GHz, not as wide as many

DMLs, this approach gives a better control of the signal waveforms which can be generated independently using an arbitrary waveform generator (AWG). Advanced modulators, such as Mach-Zehnder modulator (MZM) and in-phase and quadrature modulator (IQM), can provide more degrees of freedom in terms of signal modulation. Besides, low-linewidth lasers operating in CW mode can be used as light source, for instance, an external cavity laser (ECL) which normally has a linewidth below $\sim$100 kHz, enabling a coherence length of a few hundred meters [153, 154].

A number of novel and complex signal waveforms generated by external modulators have been proposed in the literature. For example, in order to have fast data acquisition when detecting a moving target, a double sideband signal of opposite chirping, generated by MZM, was proposed in [155]. The distance-dependent beat frequency and Doppler frequency can be detected at the same time, instead of separately from the up and down ramp as conventionally used with the triangular frequency modulation. In [81], it was proposed to modulate individual RF signals onto the upper and lower optical sidebands via an IQM. In this case, a single frequency is loaded to the lower sideband of the carrier to measure the velocity of the target, and a wide frequency-modulated signal is loaded to the upper sideband to measure the distance at a high resolution. As the velocity and distance are measured separately using different signals, this approach resolves the ranging and velocity resolution trade-off in pulsed Doppler Wind LiDAR as discussed in Sec. 2.2.1. The IQM can also be used to extend the chirping bandwidth. It was shown that by continuously sweeping the frequency from the lower optical sideband to the upper optical sideband, provided that the phase is continuous across the band, the total chirping bandwidth can be doubled and hence improves the ranging resolution by a factor of two [156, 157]. In addition to complex modulation of the lightwave, one can also modulate information onto the orthogonal polarisation using a dual-polarisation IQM to obtain a polarisation-division multiplexing system [158]. Apart from measuring distance and velocity from two polarisations separately, this technique allows detection of the depolarisation ratio of the target by examining the

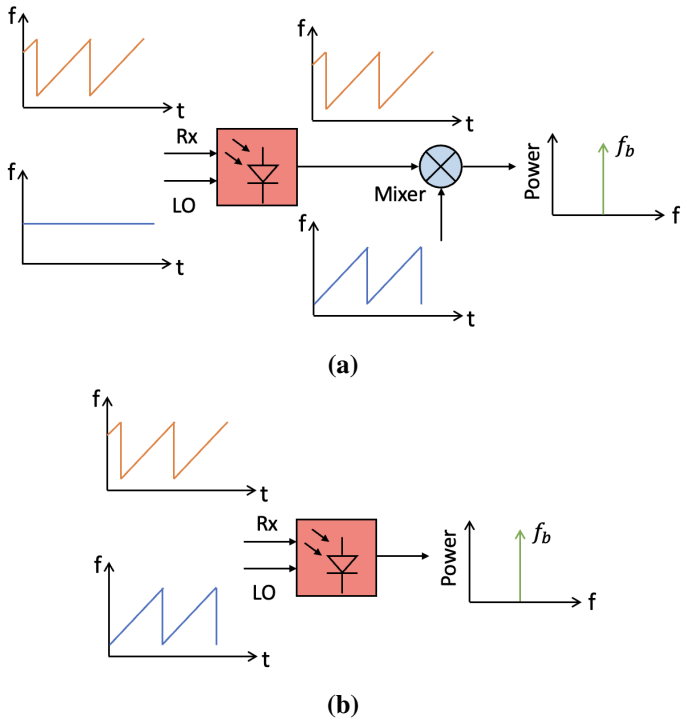

Figure 2.15: Generation of the beat frequency in coherent FMCW LiDAR through (a) electrical mixing, and (b) optical mixing. Rx refers to the received signal and f_b denotes the detected beat frequency. LO: local oscillator.

intensity of the reflected signal on two polarisations.

At the receiver side, the FMCW LiDAR requires beating with a reference signal in order to produce a beat tone as mentioned earlier. There are two main approaches to generate this beat frequency at the receiver, known as electrical mixing and optical mixing. In the case of electrical mixing, the LO is a continuous wave (CW) laser as shown in Fig.2.15(a). It can be generated from either splitting a portion from the Tx laser, or using a separate laser source in addition to the Tx laser [156]. Naturally, taking a fraction of the Tx laser as the LO would be more efficient and cost-effective in the LiDAR system as the transmiter and the receiver are co-located. The LO's function in this electrical mixing is mainly to amplify the Rx signal and down-convert the signal to the baseband [81, 155]. The detected photocurrent is a delayed chirp signal, following which an electrical mixer is used for de-chirping and to get the beat frequency [155, 159]. However, in this case, additional noise and nonlinearity are induced during frequency mixing and lead to a degraded receiver sensitivity [79]. Such drawbacks of electrical mixing

can be avoided by optical mixing where an optical splitter is used to obtain two copies of the modulated chirp signal, transmitting one and using the other as the LO [79, 156] as displayed in Fig.2.15(b). The desired beat signal is produced when the LO beats with the Rx signal during photodetection. Apart from the benefit of removing penalties from electrical mixing and simplifying the receiver configuration, this approach relaxes the bandwidth requirement for the photodiode as the beat frequency is generally smaller than the chirp bandwidth. Due to these advantages, optical mixing has been adopted in the receiver configuration in the research work presented in Chapter 4 and Chapter 5.

There are mainly three types of coherent receivers that have been employed in FMCW LiDAR, namely 1) a balanced phase-diversity coherent receiver based on an optical 90° hybrid [80], 2) 3-dB coupler-based balanced detection [75], and 3) 3-dB coupler-based receiver employing a single-ended photodiode [76]. Among them, the balanced phase-diversity coherent receiver is the most complicated as it requires a 90° optical hybrid and two pairs of balanced photodiodes (BPDs) and two transimpedance amplifiers (TIAs) for one polarisation. However, as it allows the detection of both the in-phase and the quadrature components of the signal, this receiver architecture can be used in combination with the IQM at the Tx to generate many advanced signal waveforms for improving the distance and velocity estimation performance [81, 157]. A 3-dB coupler-based receiver employing a single-ended photodiode offers the simplest coherent receiver solution. It replaces the 90° optical hybrid with a simple 3-dB coupler, and reduces two pairs of BPDs and TIAs to just a single photodiode. The system trade-off is the reduction on the receiver sensitivity as the system performance is affected by unwanted direct detection (DD) beating distortions. One possible approach to mitigate DD beating distortions is to use balanced detectors, provided that there is a good length match and the common mode rejection ratio (CMRR) is sufficiently high. Alternatively, a wide spectral guard band can be inserted to separate the DD beating distortions from the desired signal at the expense of requiring a larger electrical and optical bandwidth.

Most FMCW LiDAR systems that have been demonstrated in the literature work at the wavelength of 1550 nm. As mentioned in the introduction, this wavelength can alleviate the eye-safety issue, and is suitable for long-distance ranging of a few hundred meters. The shortcomings associated with this wavelength are first, the laser and the detection technique are relatively expensive as materials such as InP or InGaAs need to be utilised [44]. Besides, since the light at 1550 nm is subject to water absorption, it can potentially degrade the LiDAR's ability to function in rainy or foggy weather [160]. In terms of commercial products, FMCW LiDAR is not yet as mature as TOF or AMCW LiDAR, and there are not many products that can be bought off-the-shelf. Blackmore (now acquired by Aurora) was the first company that introduced FMCW LiDAR into the market [161]. In 2019, they demonstrated ranging up to 450 m and velocity measurements of up to 150 m/s [162]. More recently, SiLC and AEVA announced chip-integrated 4D LiDAR (3D environment and velocity) [163, 164]. Ranging distance up to 500 m and $\sim$mm scale precision are claimed to be possible.

2.2.4 Comparison of LiDAR systems

In the last three sections, the operating principles of three LiDAR techniques are presented. Due to the simplicity and low-cost of TOF LiDAR, it is currently the most popular and commercially available product in the market [125]. The AMCW LiDAR measures the relative phase shift between the Rx signal and the reference signal to estimate the distance, and has been mostly applied for indoor applications such as robotics and video gaming. The FMCW LiDAR encodes the target distance and velocity into beat frequencies. The utilisation of wide optical bandwidth enables a much better ranging resolution compared to the other two techniques. The presence of a strong LO at the coherent receiver also significantly improves the receiver sensitivity and allows for long-distance ranging.

Table 2.2 summarises the properties of these three types of LiDAR systems together with some achieved ranging resolution and precision in commercially available products [121, 131–133, 141, 145, 146, 161, 162, 165]. It should be noted that this table presents the parameters that are commonly used, and they are not

	Pulsed TOF	AMCW	FMCW
Wavelength	905 nm	850 nm	1550 nm
Parameter measured	Pulse delay	Phase shift	Beat frequency
Detection	Direct/Coherent	Direct	Coherent
Ranging resolution	$\sim$cm	$\sim$cm	$\sim$mm
Ranging precision	$\sim$cm	$\sim$cm	$\sim$ mm
Ranging distance	$<$ 100 m	$<$ 10 m	$>$ 100 m
Application	Indoor/Outdoor	Indoor	Indoor/Outdoor
Advantage	Simplicity	Simplicity	High resolution and resistance to background noise
Limitation	Poor sensitivity	Short ranging distance	Complexity and relatively high cost

Table 2.2: Comparison of pulsed TOF LiDAR, AMCW LiDAR and FMCW LiDAR. TOF: time-of-flight; AMCW: amplitude-modulated continuous-wave; FMCW: frequency-modulated continuous-wave.

absolute nor exhaustive. For example, TOF LiDARs are mostly seen working at around 905 nm [165, 166], but commercial products at 1550 nm or 940 nm are also available [167, 168].

Chapter 3

Adaptive frequency-domain MIMO equaliser

This chapter presents a novel frequency-domain (FD) multiple-input multiple-output (MIMO) equaliser which combines static chromatic dispersion compensation (CDC), and adaptive MIMO equalisation for mitigating polarisation mode dispersion (PMD) and state of polarisation (SOP) rotations together in the frequency domain. The frequency-domain equaliser (FDE) offers a much lower computational complexity compared to the time-domain (TD) equalisation as discussed in the last chapter. Nonetheless, the main disadvantage regarding the adaptive FD equalisation is the feedback latency. This is due to the presence of multiple FFTs/IFFTs and DSP operations in the feedback loop which may require multiple clock cycles [169]. This gives rise to a delay in the update of adaptive filter coefficients, and consequently degrades the tracking ability of adaptive equalisers [55, 64].

In order to improve the adaptive FD equaliser's tolerance to feedback delays, a momentum-based gradient descent algorithm is introduced for the first time to the adaptive FDE. The operating principle of the proposed FD-MIMO equaliser is presented in Sec. 3.1. Sec. 3.2 describes the simulation setup used to evaluate the performance of the proposed adaptive equaliser. Following this, simulation results comparing momentum-based gradient descent and conventional gradient descent are discussed in Sec. 3.3. Sec. 3.4 summarises the research work presented in this chapter.

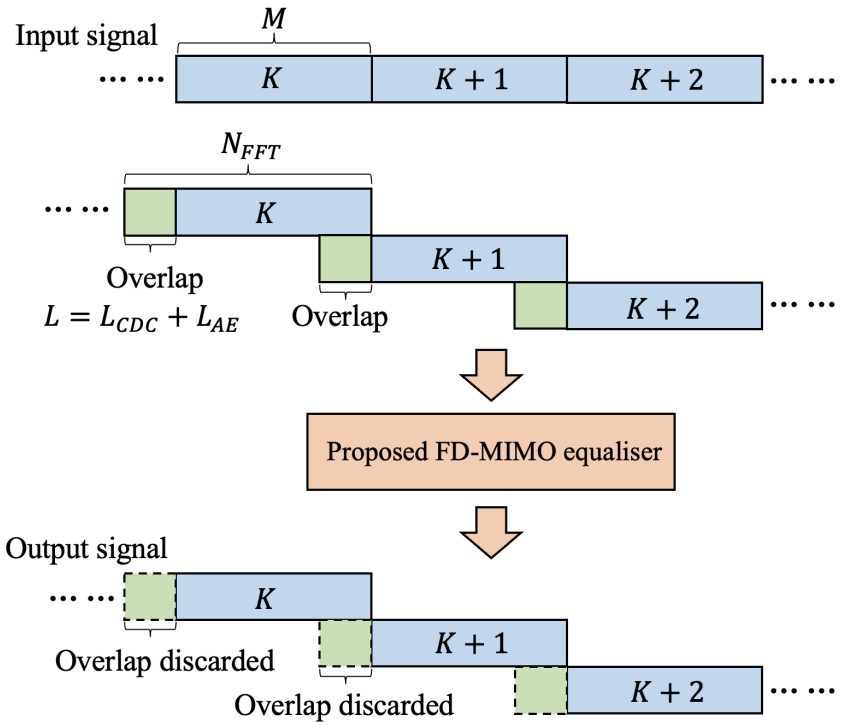

Figure 3.1: Block processing of FD-MIMO equaliser with overlap-save method. The notations are summarised in Table 3.1. CDC: chromatic dispersion compensation; AE: adaptive equaliser; FD-MIMO: frequency-domain multiple-input multiple-output.

3.1 Operating principle of frequency-domain MIMO equaliser

Fig.3.1 shows the block processing of the proposed FD-MIMO equaliser. The notations used in the following explanation are summarised in Table 3.1. As discussed in Ch.2, the overlap-save method has a lower computational complexity compared to the overlap-add approach, and hence has been used in the equaliser studied in this work [63, 170]. The input time-domain signal is first partitioned into blocks of M samples. In the overlap-save method, the overlap is achieved by taking L samples from the last block, giving a total block length of $L+M=N_{FFT}$. After performing FD-MIMO equalisation, the output blocks are combined together in the time domain with overlap samples being removed.

The schematic of the proposed FD-MIMO equaliser is shown in Fig.3.2. It is composed of two static equalisers and an adaptive equaliser. As Nyquist pulse

Description	Notation
Frequency-domain vector	Bold uppercase letter
Time-domain vector	Bold lowercase letter
Scalar	Non-bold letter
Index of the block	K
Signal length	M
Filter length of CDC	L_{CDC}
Filter length of adaptive equaliser	L_{ADEQ}
Total filter length	$L(L = L_{CDC} + L_{ADEQ})$
Block length (i.e., FFT size)	$N_{FFT}(N_{FFT} = L + M)$
x / y polarisation	x / y
Element-by-element multiplication	$\otimes$
Complex conjugate	$*$
A column vector of all zeros	$\mathbf{O}_L$

Table 3.1: Notations used in the derivation of proposed FD-MIMO equaliser. The size of the zero column vector $\mathbf{O}_L$ will be specified in the derivation.

shaping is widely employed in optical communications to maximise the bandwidth efficiency and minimise inter-symbol interference (ISI), a frequency-domain matched filtering using a root-raised cosine (RRC) filter is performed after static CDC [171]. The following adaptive equaliser mitigates PMD and tracks SOP rotations. The input time-domain signal, sampled at 2 samples per symbol, is transformed into the frequency domain using a pair of FFTs. As the chromatic dispersion is a static effect, it can be mitigated by multiplying the signal with the inverse transfer function of the dispersive link given in Eq.2.8 in Sec. 2.1. Hence, the transfer function for CDC is given by:

$$\mathbf{G}_{CDC} = \exp\left(j\frac{D\lambda^2 z}{4\pi c}\omega^2\right) \tag{3.1}$$

where D denotes the dispersion parameter, λ is the reference wavelength, z

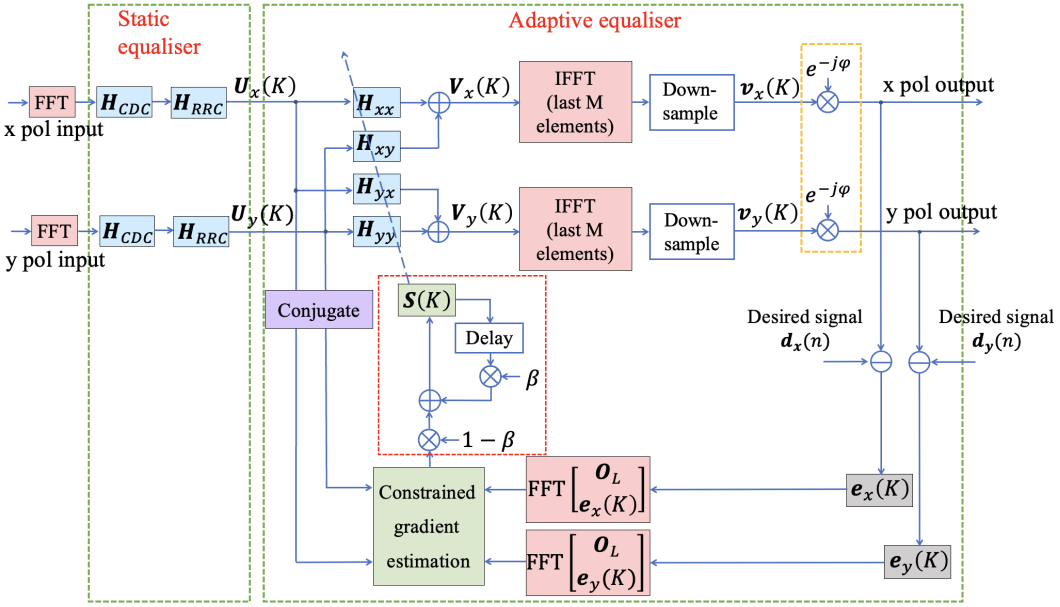

Figure 3.2: Schematic of the proposed FD-MIMO equaliser with two static equalisers for chromatic dispersion compensation and matched filtering, and one adaptive equaliser for mitigating time-varying distortions. The red-dash box displays the implementation of momentum-based gradient descent and the yellow-dash box shows pilot-based carrier phase estimation. The $\mathbf{O}_L$ denotes a L by 1 zero vector. CDC: chromatic dispersion compensation; RRC: root-raised cosine; FFT: fast Fourier transform; IFFT: inverse fast Fourier transform.

represents the transmission distance, c is the speed of light and ω denotes the angular frequency. As discussed in Sec. 2.1, the number of overlap samples is critical for effective chromatic dispersion compensation in the frequency-domain block processing [170]. Using the approximation of Gaussian pulse broadening, the minimum overlap is calculated as [170]:

$$\begin{aligned} T_p &= \frac{2}{\pi c T_s}\sqrt{\pi^2 c^2 T_s^4 + 4\lambda^4 D^2 z^2} \\ L_{CDC} &= 2 \times \left\lceil \frac{T_p}{2T_s} \right\rceil + 2 \end{aligned} \tag{3.2}$$

where T_p refers to the width of the broadened Gaussian pulse and T_s is the sample duration. Directly multiplying the frequency-domain signal with $\mathbf{G}_{CDC}$, the first $\frac{L_{CDC}}{2}$ and last $\frac{L_{CDC}}{2}$ samples should be discarded after converting back to the time domain, which accounts for inter-block interference (IBI) [97, 172]. For the convenience of implementation, a time delay (i.e., corresponds to a frequency shift

$\exp\left(-j\frac{L_{CDC}}{2}\times\omega\right)$) is added to the normal CDC transfer function (i.e., $\mathbf{G}_{CDC}$), so that the first L_{CDC} samples are now responsible for IBI and should be removed after equalisation. This time-delayed CDC is described as:

$$\begin{aligned}\mathbf{H}_{CDC} &= \mathbf{G}_{CDC}\times\exp\left(-j\frac{L_{CDC}}{2}\omega\right)\\ &= \exp\left\{\left(j\frac{D\lambda^2 z}{4\pi c}\omega^2 - j\frac{L_{CDC}}{2}\omega\right)\right\}\end{aligned} \tag{3.3}$$

Following CDC, the matched filtering is performed using a RRC filter as shown in Fig.3.2. It is often employed together with the transmitter RRC filter, giving a raised cosine (RC) shaped pulse. Depending on the roll-off factor of the RC filter, the shaped signal can have a near-rectangular spectrum which is desirable in terms of maximising the bandwidth efficiency [91]. In the frequency domain, the response of RC filter can be described as [171]:

$$\mathbf{H}_{RC}(f) = \begin{cases} 1 & |f| < \frac{1-\alpha}{2T_{sys}} \\ \frac{1}{2}\left[1+\cos\left(\frac{\pi T_{sys}}{\alpha}\left[|f|-\frac{1-\alpha}{2T_{sys}}\right]\right)\right] & \frac{1-\alpha}{2T_{sys}} \le |f| \le \frac{1+\alpha}{2T_{sys}} \\ 0 & \text{otherwise} \end{cases} \tag{3.4}$$

where f represents the frequency, α is the roll-off factor usually taking values from $[0,1]$ and T_{sys} denotes the symbol period. Taking the square-root of the frequency response of RC filter gives the transfer function of the RRC filter [171]:

$$\mathbf{H}_{RRC}(f) = \sqrt{|\mathbf{H}_{RC}(f)|} \tag{3.5}$$

Hence, the matched filtering is achieved by a complex multiplication between the frequency-domain transfer function of the RRC filter and the signal spectrum [14].

For implementing the adaptive MIMO equaliser, four sets of filter tap weights are initialised in the time domain, each of length L_{ADEQ} to accommodate the pulse

broadening induced by PMD. The adaptive equaliser is operated with constrained gradient descent algorithm as it offers a stable equalisation as discussed previously in Sec.2.1.2. The decision-directed least mean square (DD-LMS) algorithm is employed to update the filter coefficients [54]. In order to make correct decisions on symbols using the DD-LMS algorithm, phase noise needs to be removed first. In the implementation, QPSK pilot symbols inserted at the rate of $\frac{1}{32}$ are used for carrier phase estimation, giving an overhead of 3.1% [107]. The first few QPSK pilots with known phase and polarisation state at the transmitter are used to obtain an initial estimation of the polarisation rotation, and used to set the center tap of the filter coefficients, with the rest of taps being set to zero. Following this, FFTs are applied to convert the time-domain filter coefficients into the corresponding frequency response. After using pilot symbols for initialisation of the adaptive filter coefficients, the adaptive equaliser is updated in a blind manner.

The equalisation process for two polarisations is described by:

$$\begin{aligned} \mathbf{V}_x(K) &= \mathbf{H}_{xx}(K) \otimes \mathbf{U}_x(K) + \mathbf{H}_{xy}(K) \otimes \mathbf{U}_y(K) \\ \mathbf{V}_y(K) &= \mathbf{H}_{yx}(K) \otimes \mathbf{U}_x(K) + \mathbf{H}_{yy}(K) \otimes \mathbf{U}_y(K) \end{aligned} \tag{3.6}$$

where $\mathbf{H}_{xx}$, $\mathbf{H}_{xy}$, $\mathbf{H}_{yx}$ and $\mathbf{H}_{yy}$ are the frequency-domain filter coefficients, $\mathbf{U}_x$ and $\mathbf{U}_y$ are the frequency-domain input signals, $\mathbf{V}_x$ and $\mathbf{V}_y$ are the frequency-domain output signals, K is the block number and $\otimes$ denotes element-by-element multiplication as illustrated in Table.3.1.

After converting the equalised signal back to the time domain and down-sampling to 1 sample per symbol, the phase noise is estimated by comparing the phase rotation between transmitted and received pilot symbols. It is then linearly interpolated with the Wiener filter coefficients which can give a minimum-mean square estimation of the original phase noise [173]. The inverse of the estimated phase noise profile (i.e., $e^{-j\varphi}$) is then applied to the time-domain output signal to remove the laser phase noise, as shown in the yellow-dash box in Fig.3.2. Following this, the time-domain error vectors are calculated by comparing the deviation of equalised output signal from the desired signal. Considering only the payload

symbols, this is given by:

$$\mathbf{e}_{x,y}(K) = (\mathbf{d}_{x,y}(K) - e^{-j\varphi}\mathbf{v}_{x,y}(K))e^{j\varphi} \tag{3.7}$$

where $\mathbf{v}_{x,y}(K)$ denotes the time-domain adaptive equaliser output after down-sampling for x or y polarisation as shown in Fig.3.2, $\mathbf{d}_{x,y}(K)$ denotes the vector of the most likely symbols (i.e., desired symbols) after hard decisions. The term $e^{j\varphi}$ at the end of Eq.3.7 is used to feed back the estimated phase noise after making hard decisions as the input signals (i.e., $\mathbf{U}_x(K)$ and $\mathbf{U}_y(K)$) of the adaptive equaliser are still affected by the laser phase noise. The error vectors are then up-sampled and used for estimating the gradient.

The gradient is calculated in the constrained sense. Applying the time-domain constraint ensures that the frequency-domain filter coefficients and time-domain filter coefficients are equivalent [60, 63]. The time-domain gradients are given by:

$$\begin{aligned}
\nabla_{xx}(K) &= \text{first } L_{ADEQ} \text{ elements of IFFT}(\mathbf{E}_x(K) \otimes \mathbf{U}_x^*(K)) \\
\nabla_{xy}(K) &= \text{first } L_{ADEQ} \text{ elements of IFFT}(\mathbf{E}_x(K) \otimes \mathbf{U}_y^*(K)) \\
\nabla_{yx}(K) &= \text{first } L_{ADEQ} \text{ elements of IFFT}(\mathbf{E}_y(K) \otimes \mathbf{U}_x^*(K)) \\
\nabla_{yy}(K) &= \text{first } L_{ADEQ} \text{ elements of IFFT}(\mathbf{E}_y(K) \otimes \mathbf{U}_y^*(K))
\end{aligned} \tag{3.8}$$

where the asterisk denotes the complex conjugate. $\mathbf{E}_x(K)$ and $\mathbf{E}_y(K)$ represent the frequency-domain error vectors given by:

$$\mathbf{E}_{x,y}(K) = \text{FFT}\begin{bmatrix} \\ \mathbf{O}_L \\ \\ \mathbf{e}_{x,y}(K) \end{bmatrix} \tag{3.9}$$

where $\mathbf{O}_L$ denotes an L by 1 zero vector and $\mathbf{e}_{x,y}(K)$ is defined in Eq.(3.7).

Using conventional gradient descent for updating the filter coefficients,

$\mathbf{H}_{xx}(K+1)$ can be updated in the frequency domain as:

$$\mathbf{H}_{xx}(K+1) = \mathbf{H}_{xx}(K) + \mu \mathbf{G}_{xx}(K) \tag{3.10}$$

where μ denotes the step size. $\mathbf{G}_{xx}(K)$ is the gradient vector which is simply the frequency-domain representation of the time-domain gradient vector $\nabla_{xx}(K)$ given by:

$$\mathbf{G}_{xx}(K) = \text{FFT} \begin{bmatrix} \nabla_{xx}(K) \\ \\ \mathbf{O}_L \end{bmatrix} \tag{3.11}$$

where $\mathbf{O}_L$ is a zero vector with length of $L_{CDC} + M$ and $\nabla_{xx}(K)$ is defined in Eq.3.8. It can be seen that Eq.3.8 and Eq.3.11 are used to implement constrained gradient estimation by applying a time-domain constraint as previously discussed in Sec.2.1.2. The same operation can be applied to obtain $\mathbf{H}_{xy}(K+1)$, $\mathbf{H}_{yx}(K+1)$, $\mathbf{H}_{yy}(K+1)$.

It should be noted that the configuration of adaptive FDE for mitigating PMD and SOP rotations described above is similar to the FDE implemented in [60]. Nevertheless, in this work, the adaptive equaliser is updated using the DD-LMS algorithm, while the constant modulus algorithm (CMA) method was employed in [60]. Besides, the sub-equaliser was used for odd and even samples in [60] which is not considered in this work.

Apart from implementing chromatic dispersion compensation, matched filtering, and adaptive MIMO equalisation using DD-LMS together in one FFT block which is one of the main novelties of this algorithm, the momentum-based gradient descent algorithm is introduced to the FD-MIMO equaliser for the first time to improve the adaptive equaliser's tolerance against feedback latency. In the conventional implementation of gradient descent as discussed above, the adaptive filter update only relies on the current gradient information, and it is independent of all the previous updates (see Eq.3.8 and Eq.3.10). In the presence of adaptive filter update delays or rapid polarisation rotations where the signal is rather unstable, the

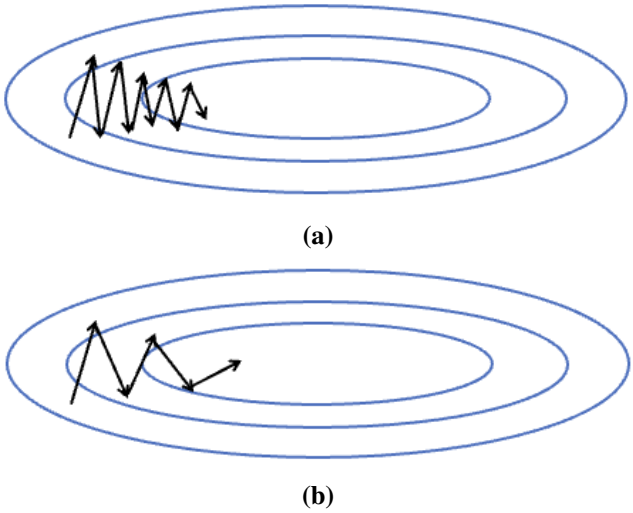

Figure 3.3: The trajectory of the gradient update on the contour of the cost function, by using (a): conventional gradient descent; (b): momentum-based gradient descent. The center of the contour denotes the optimum.

gradient update will suffer from greater oscillations, bouncing up and down around the contour of the cost function as illustrated in Fig.3.3(a). For the purpose of arriving at optimum of the contour of the cost function, and obtaining the optimum adaptive filter taps, these fluctuations on the vertical axis are not desirable and will slow down the convergence speed of adaptive equaliser. In order to smooth out these vertical oscillations, the momentum-based gradient descent algorithm is implemented, shown in the red-dash box in Fig.3.2. Updating $\mathbf{H}_{xx}(K+1)$ using momentum-based gradient is given by:

$$\mathbf{H}_{xx}(K+1) = \mathbf{H}_{xx}(K) + \mu \mathbf{S}_{xx}(K) \tag{3.12}$$

Filter coefficients $\mathbf{H}_{xy}(K+1)$, $\mathbf{H}_{yx}(K+1)$, and $\mathbf{H}_{yy}(K+1)$ using momentum-based gradient descent are adjusted in a similar manner. In Eq.3.12, $\mathbf{S}_{xx}(K)$ denotes the momentum-based gradient. It is calculated as [174]:

$$\mathbf{S}_{xx}(K) = (1-\beta)\mathbf{G}_{xx}(K) + \beta \mathbf{S}_{xx}(K-1) \tag{3.13}$$

where $\mathbf{G}_{xx}(K)$ is the conventional gradient defined in Eq.3.11, β is the momentum parameter, usually taking values from $[0,1]$, $\mathbf{S}_{xx}(K-1)$ denotes the

momentum-based gradient calculated from the previous block [174]. To elaborate the operation principle of momentum-based gradient descent, Eq.3.13 can be further expanded as:

$$\begin{aligned}
\mathbf{S}_{xx}(K-1) &= (1-\beta)\mathbf{G}_{xx}(K-1) + \beta\mathbf{S}_{xx}(K-2) \\
\mathbf{S}_{xx}(K-2) &= (1-\beta)\mathbf{G}_{xx}(K-2) + \beta\mathbf{S}_{xx}(K-3) \\
&\vdots \\
\mathbf{S}_{xx}(1) &= (1-\beta)\mathbf{G}_{xx}(1) + \beta\mathbf{S}_{xx}(0)
\end{aligned} \tag{3.14}$$

where $\mathbf{S}_{xx}(0)$ is the initial gradient which can be set as 0. Combining Eq.3.13 and Eq.3.14 together gives:

$$\mathbf{S}_{xx}(K) = (1-\beta)\sum_{n=1}^{K}\beta^{K-n}\mathbf{G}_{xx}(n) + \beta^{K}\mathbf{S}_{xx}(0) \tag{3.15}$$

The last constant term $\beta^K\mathbf{S}_{xx}(0)$ in Eq.3.15 is related to the initialisation which can be ignored. The left last term indicates that momentum-based gradient estimation considers all the previous gradient updates. It behaves similarly to an exponential moving average with the momentum parameter β assigning different weights to the current and past gradients. In practice, β is often set to the value of 0.9, as it is shown to be robust and to work well in most cases [174]. Therefore, according to Eq.3.15, it can be seen that more recent gradients are given much higher weights as this exponential term β^{K-n} approaches 1, while the impact of older gradients gradually vanish as β^{K-n} is close to 0. With the momentum-based gradient estimation being implemented, the gradient update oscillations due to the occurrence of filter update delay or rapid dynamic channel variations can be averaged out as illustrated in Fig.3.3(b). Therefore, the momentum-based gradient descent can significantly improve the adaptive equaliser's tracking ability compared to the conventional gradient descent algorithm.

3.2 Simulation setup

Simulations were carried out using MATLAB to numerically assess the performance of the proposed FD-MIMO equaliser with momentum-based gradient algorithm in the presence of feedback latencies and varying SOP rotation frequencies. The results are compared with those obtained using a FD-MIMO equaliser with a conventional gradient descent approach.

In the simulation, a 92 Gbaud dual-polarisation (DP) 64 QAM system was modelled. A long random input signal sequence of 9.8304×10^5 symbols was generated, allowing the adaptive filter to converge to and then accurately track the signal polarisation and compensate the PMD from the optical channel. The system performance was evaluated on the last $55,536$ symbols of the signal once the adaptive equaliser had converged. At the transmitter, the DP 92 Gbaud 64 QAM signal was generated with the insertion of QPSK pilot symbols at the rate of $\frac{1}{32}$, used for carrier phase estimation (CPE). The signal was up-sampled to 2 samples/symbol and spectrally shaped by an RRC filter with 0.01 roll-off factor, following which an ideal dual-polarisation IQM was applied. The transmitter laser was centered at 1550 nm and had a linewidth of 100 kHz.

The optical channel considered in this work was a single span of standard single-mode fibre (SSMF), with a length of 40 km or 80 km. The chromatic dispersion was assumed to be 16.8 $\text{ps} \cdot \text{nm}^{-1}\text{km}^{-1}$. Based on Eq.3.2, the overlap L_{CDC} was 234 and 466 samples for the 40 km and 80 km SSMF respectively to achieve effective CDC. The effect of PMD and SOP rotations was modelled by the concatenation of a series of random birefringence sections as presented in Section 2.1.2, i.e., modeling the 40 km and 80 km fibre span as 40 and 80 cascaded 1 km section respectively, each with random birefringence. For a given section i, it

can be described using the Jones matrix R_i and D_i given in Eq.2.11, restated here:

$$\mathbf{R}_i = \begin{bmatrix} \cos\theta_i e^{-j\phi_i} & \sin\theta_i \\ -\sin\theta_i & \cos\theta_i e^{j\phi_i} \end{bmatrix} \quad \mathbf{D}_i = \begin{bmatrix} e^{-j\omega\frac{\tau_i}{2}} & 0 \\ 0 & e^{j\omega\frac{\tau_i}{2}} \end{bmatrix} \tag{3.16}$$

where θ_i and ϕ_i refer to the random rotation and random phase shift between two polarisations following the uniform distribution between $[-\pi,\pi]$ and $[-\pi/2,\pi/2]$ respectively, τ_i denotes the local differential group delay [175]. In this simulation, only first-order PMD was emulated with a PMD parameter of 0.5 ps/$\sqrt{\text{km}}$ and hence τ_i was set to 0.5427 ps [53,102]. With a symbol rate of 92 Gbaud and receiver DSP operating at 2 samples/symbol, adaptive filter length L_{ADEQ} = 16 was sufficient to cover the pulse broadening induced by PMD. Together with the overlap samples used for chromatic dispersion compensation, the total overlap lengths L were 250 and 482 in the 40 km and 80 km link respectively. In order to have a sufficient number of signal samples for equalisation, the corresponding FFT block size in the receiver DSP was set to 512 samples for the 40 km link and 1024 samples for 80 km link. To test the dynamic tracking ability of the FD-MIMO equaliser, continuous SOP rotation J_{SOP} was also included in the modelling [53]:

$$\mathbf{J}_{SOP} = \begin{bmatrix} \cos(2\pi f_{SOP}t) & \sin(2\pi f_{SOP}t) \\ -\sin(2\pi f_{SOP}t) & \cos(2\pi f_{SOP}t) \end{bmatrix} \tag{3.17}$$

where f_{SOP} denotes the rotation frequency of the SOP and t is the time instance. Under normal conditions, the SOP rotation speed varies up to 100 krad/s in practice [176]. Hence, the continuous SOP rotation frequency was varied from 0 to 60 kHz in the simulation. The overall dynamic channel model was given as:

$$\mathbf{J} = \mathbf{R}_N\mathbf{D}_N \ldots \mathbf{R}_i\mathbf{D}_i \ldots \mathbf{R}_1\mathbf{D}_1\mathbf{J}_{SOP} \tag{3.18}$$

where N denotes the total number of cascaded sections. Assuming the Erbium-doped fibre amplifier (EDFA) was used to compensate the loss induced by the optical fibre, amplified spontaneous emission (ASE) noise was added to the system by varying the received optical signal-to-noise ratio (OSNR) value within a 0.1 nm resolution bandwidth.

At the receiver, the signal was combined with a local oscillator (LO) centered at 1550 nm in an ideal polarisation-diverse 90° optical hybrid based coherent receiver. The power of the LO was 13 dBm and its linewidth was 100 kHz. Photodetection and balanced detection were assumed to be ideal to cancel out common modes. The signal then passed through the proposed FD-MIMO equaliser to mitigate impairments from the optical channel (i.e., chromatic dispersion, PMD and SOP rotations) and the laser-induced phase noise. In the operation of the momentum-based gradient descent algorithm, the momentum parameter β was set to 0.9 as commonly used in the literature [174]. Assuming soft-decision forward error correction codes, the system performance was evaluated using generalised mutual information (GMI) once the adaptive equaliser had converged. GMI indicates the maximum data throughput in a bit-wise decoder [177]. It is shown to be a more reliable metric for evaluating the performance of coded optical channels than conventional metrics such as bit error rate (BER) or Q-factor as it also considers the confidence in making decisions on received bits [178] . The maximum GMI is modulation format dependent. In the case of DP 64 QAM considered in this work, 12 bits are encoded and hence the maximum GMI for two polarisations is 12. In the simulation results presented in the next section, GMI/m was chosen to quantify the system performance where m denotes the total number of bits for two polarisations (m $=$ 12 in the case of DP 64QAM considered in the simulation). Hence, GMI/m indicates normalised bits per symbol that can be successfully detected after performing DSP. In the simulation results presented below, GMI/m was obtained as the average of ten runs of simulations at each SOP rotation frequency and feedback delay.

In the ideal case without delay in the filter update, the signal in block K is

equalised as shown in Eq.3.6, with the adaptive filter coefficients updated from the last block. However, in the presence of feedback latency which is unavoidable in practical real-time implementations of adaptive FDE, the equalisation process for two polarisations is modeled as:

$$\begin{aligned}\mathbf{V}_x(K) &= \mathbf{H}_{xx}(K-P)\otimes\mathbf{U}_x(K)+\mathbf{H}_{xy}(K-P)\otimes\mathbf{U}_y(K)\\ \mathbf{V}_y(K) &= \mathbf{H}_{yx}(K-P)\otimes\mathbf{U}_x(K)+\mathbf{H}_{yy}(K-P)\otimes\mathbf{U}_y(K)\end{aligned} \tag{3.19}$$

where P denotes the delay in terms of the number of FFT blocks. Eq.3.19 shows that the signal in block K is now equalised by the filter coefficients that are P blocks earlier than the current signal block which suggests that the filter coefficients are not up-to-date. If the signal has undergone rapid changes between $\mathbf{U}_{x,y}(K-P)$ and $\mathbf{U}_{x,y}(K)$, e.g., due to rapid SOP rotations, the tracking ability of the adaptive equaliser can be impaired.

3.3 Performance of momentum-based gradient descent

In the simulation of the 40 km link, the FFT size corresponding to the block length was 512 samples. Both conventional gradient descent and momentum-based gradient descent were implemented in the frequency domain as described in Sec.3.1. Fig.3.4 shows the performance of the FD-MIMO equaliser at an OSNR of 35 dB. In the absence of feedback latency (i.e., zero delay), the FD-MIMO equalisers using both the conventional gradient descent and the momentum-based gradient estimation successfully mitigate the static and dynamic distortions from the fibre, giving a GMI/m of approximately 1 (12 bits for two polarisations). When including a delay in the feedback affecting the filter update, the tracking ability of the adaptive equaliser employing the conventional gradient calculation is impaired. Its performance starts to break down at a delay of 4 FFT blocks and at a SOP rotation frequency of 60 kHz. In contrast, applying momentum-based gradient estimation, the tracking ability of the adaptive equaliser is significantly improved. It is robust to delays up to 14 blocks with SOP rotation frequencies up to 50 kHz. At a SOP rotation frequency of 60 kHz, the equaliser's tracking ability is degraded at feedback

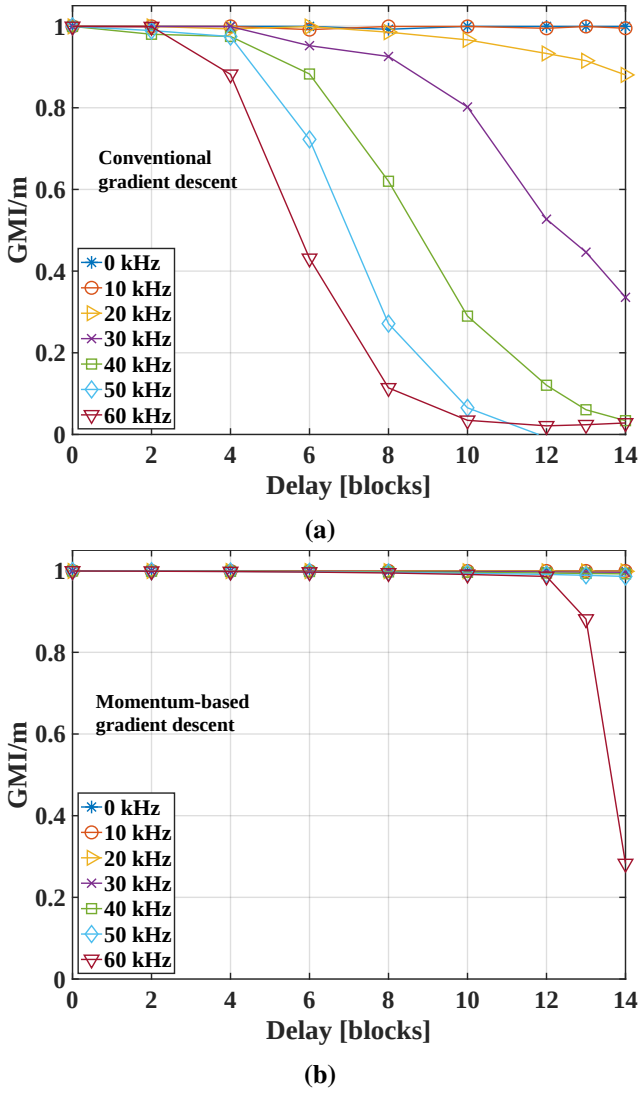

Figure 3.4: The performance of the FD-MIMO equaliser at an OSNR of 35 dB. (a): conventional gradient descent; (b): momentum-based gradient descent.

delays above 13 FFT blocks.

At 50 kHz SOP rotation frequency and zero block delay, the received signal scatter plots for the x polarisation using conventional gradient descent and momentum-based gradient descent are compared in Fig.3.5. The y polarisation performs similarly. Without delay in the feedback loop, both methods achieve good channel equalisation at 50 kHz SOP rotation frequency resulting in a clean scatter plot. The noisy clouds around the ideal constellation points are mainly due to the ASE noise. The scatter plots when employing the conventional gradient descent method with 8 blocks delay in the feedback loop, and the momentum-based gradient

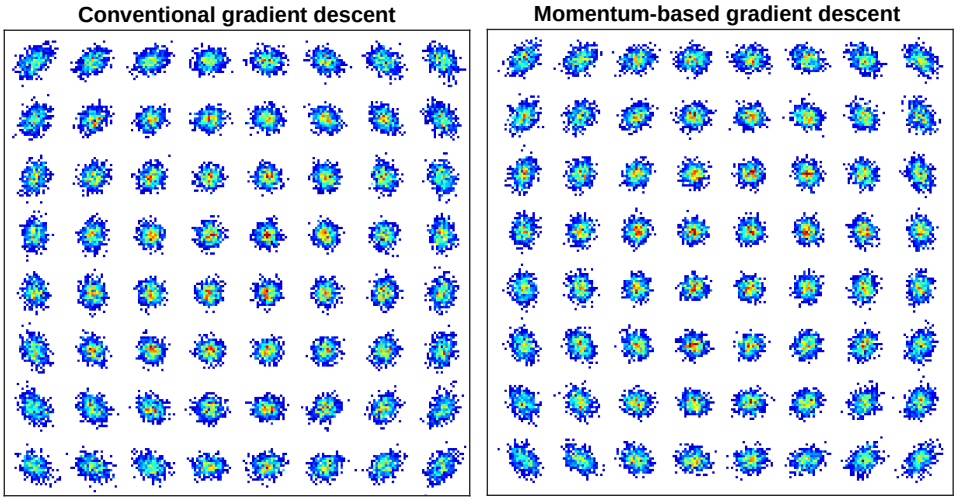

Figure 3.5: Without feedback delay, the received signal constellations employing (a) conventional gradient descent and (b) momentum-based gradient descent at 35 dB OSNR and 50 kHz SOP rotation speed.

descent with 14 blocks delay are presented in Fig.3.6. In the case of conventional gradient descent, the equaliser starts to fail to track 50 kHz SOP rotation at a delay of 8 FFT blocks, resulting in a more distorted constellation (GMI/m $\approx$ 0.28 as shown in Fig.3.4(a)). In contrast, employing momentum-based gradient descent, even at 14 blocks delay as shown in Fig.3.6(b), the equaliser is still capable of recovering the signal and the scatter plot is relatively clear (GMI/m $\approx$ 0.98 as displayed in Fig.3.4(b)).

The results with the 40 km link at an OSNR of 30 dB are shown in Fig.3.7, and the maximum achievable GMI/m decreases slightly to 0.98 due to the additional ASE noise. The ASE noise also degrades the performance of the FD-MIMO equaliser. Similar to the trend in Fig.3.4, the conventional gradient estimation fails to track high SOP rotations ($\geq$ 30 kHz) when there are delays of 2 blocks or more. In contrast, the performance of the momentum-based gradient descent algorithm only starts to deteriorate at an SOP rotation frequency of 60 kHz and at feedback delays of 8 blocks and above.

In Fig.3.8, simulation results for the 80 km link with received OSNR of 27 dB are plotted, showing the performance for the longer distance and lower OSNR. The required overlap samples for FD chromatic dispersion compensation of 80 km

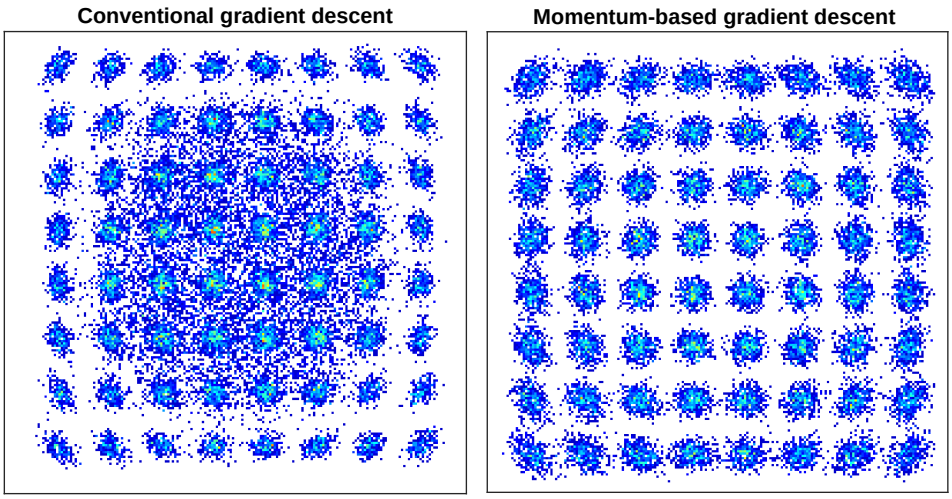

Figure 3.6: Received signal constellations at 35 dB OSNR and 50 kHz SOP rotation speed, by using (a) conventional gradient descent at 8 blocks delay, and (b) momentum-based gradient descent at 14 blocks delays.

SSMF were 466 as mentioned earlier. The overlap samples used for the adaptive equaliser were kept at 16, and therefore, the total overlap length was 482. The FFT size was increased to 1024 points to accommodate all the overlap samples.

At an OSNR of 27 dB, the initial GMI/m is around 0.91 as shown in Fig.3.8, limited by the ASE noise. The trends in the results are similar to those observed in the 40 km link as discussed above. However, due to the lower OSNR, the high level of ASE noise causes more perturbations to the equaliser's tracking ability. The equaliser fails to track 10 kHz SOP rotation with feedback delays of 8 FFT blocks or more when employing conventional gradient descent while momentum-based gradient descent can still successfully track SOP rotations of up to 20 kHz with 13 blocks delay.

The evolution of the SOP rotation can also be analysed using Stokes parameters, and visualised on the Poincaré sphere [179]. Assuming a linearly polarised input (i.e., $s = [1,0,0]^T$) and 50 kHz SOP rotation frequency, the trajectory of the first 2^{16} time instances obtained using Eq.3.17 are shown in Fig.3.9(a). It can be seen that the trajectory of the SOP rotation lies on the equator of the Poincaré sphere which represents a linear polarisation state [179]. In order to more exhaustively test the equaliser, the SOP rotations were modelled as random walks

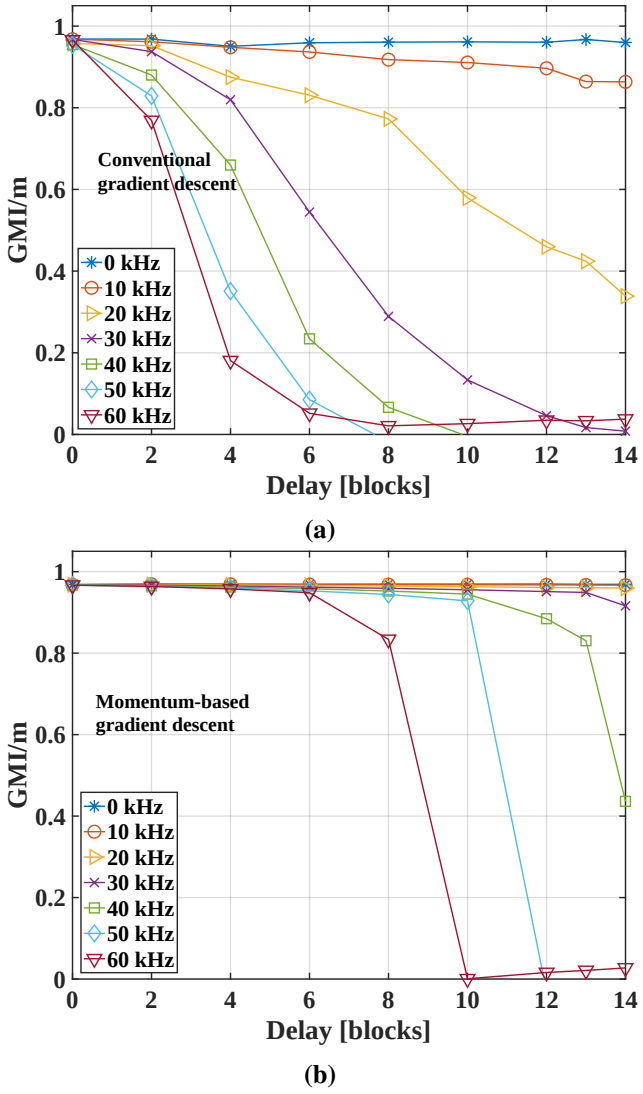

Figure 3.7: Performance of the FD-MIMO equaliser at an OSNR of 30 dB. (a): conventional gradient descent; (b): momentum-based gradient descent.

of the polarisation angle and phase. In these simulations, J_{SOP} in Eq.3.17 was replaced by:

$$\mathbf{J}_{SOP} = \begin{bmatrix} \cos\theta(t)e^{-j\phi(t)} & \sin\theta(t) \\ -\sin\theta(t) & \cos\theta(t)e^{j\phi(t)} \end{bmatrix} \tag{3.20}$$

where the sampled values $\theta(t)$ and $\phi(t)$ were generated by random walks with the frequency change in θ and ϕ between samples being normally distributed random values. An example of the resulting trajectory of SOP rotations is plotted

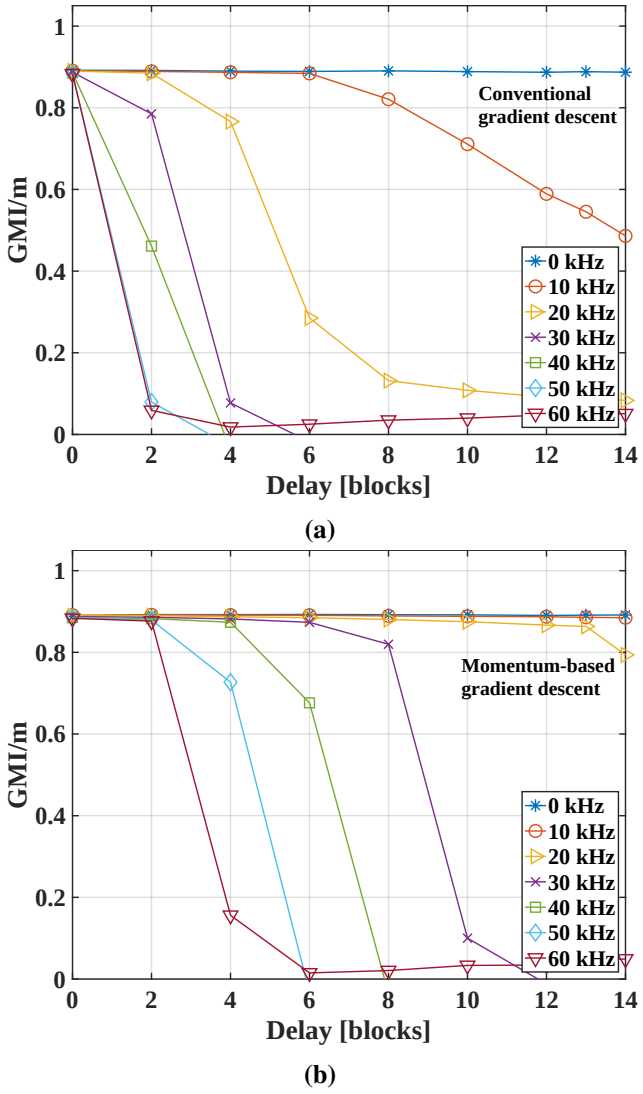

Figure 3.8: The performance of FD-MIMO equaliser at an OSNR of 27 dB. (a): conventional gradient descent; (b): momentum-based gradient descent.

in Fig.3.9(b). It can been seen that the state of polarisation traces a random path around the surface of the Poincaré sphere. In this case, the momentum-based gradient descent algorithm was still found to be more robust to feedback delays and fast SOP rotations than the conventional gradient descent approach. Simulation results show that in the 40 km link, with a received OSNR of 35 dB and an SOP rotation frequency of 1.1 MHz, the momentum-based gradient descent method can successfully track SOP rotation and tolerate delays of up to 14 FFT blocks with GMI/m $\approx$ 1. However, the conventional gradient descent starts to break down at a delay of 10 blocks with GMI/m $\approx$ 0.64.

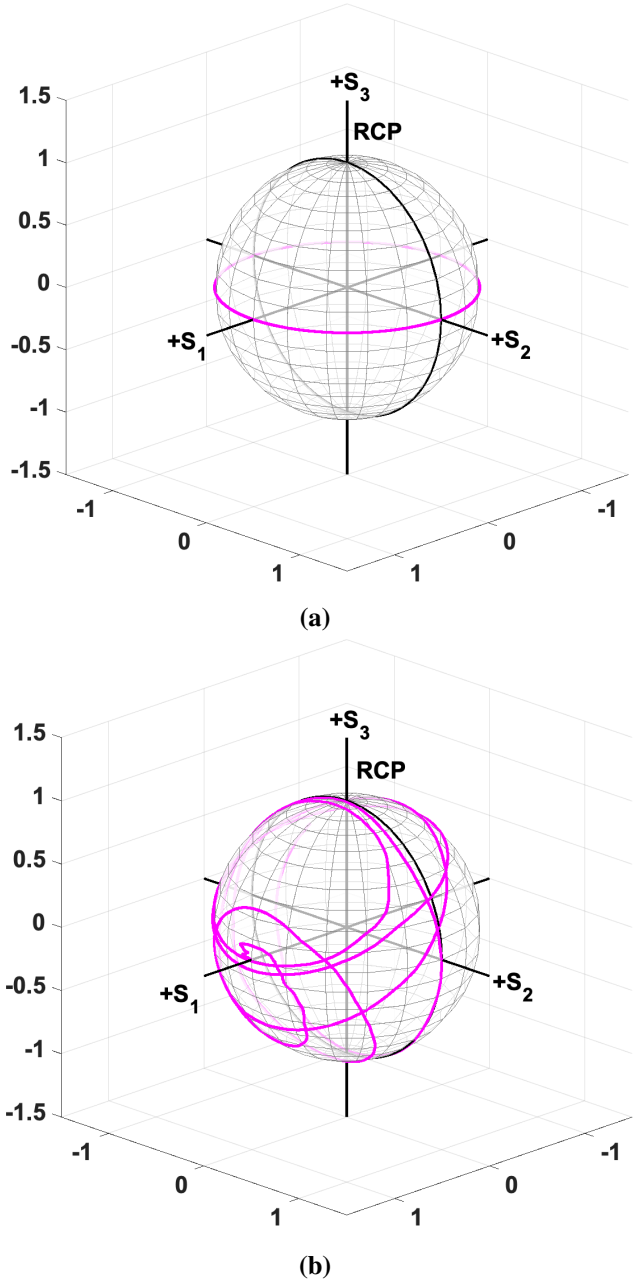

Figure 3.9: Trajectory of the Stokes parameters, (a) with the continuous time-varying polarisation angle, and (b) with polarisation angle (θ) and phase (ϕ) following random walks. RCP: right circularly polarised.

3.4 Summary

In this chapter, a novel frequency-domain (FD) multiple-input multiple-output (MIMO) equaliser employing a momentum-based gradient descent update algorithm is investigated in polarisation-division multiplexing (PDM) coherent systems. The FD-MIMO equaliser combines chromatic dispersion compensation (CDC), matched filtering and adaptive equalisation for mitigating time-varying distortions together in a single frequency-domain block processing. Therefore, multiple frequency domain and time domain conversions, i.e., FFTs and IFFTs between individual DSP stages, can be avoided to reduce the computational complexity. Besides, the adopted momentum-based gradient descent has been demonstrated to have the ability to successfully track dynamically varying optical channels and mitigate penalties from feedback latency which is the main disadvantage of adaptive frequency-domain equalisation. Therefore, the proposed FD-MIMO equaliser would be beneficial for applications in short-reach optical links, offering a low complexity and high performance solution for mitigating static and time-varying distortions from the optical fibre.

Chapter 4

Single-photodiode based coherent LiDAR

The basic operating principles of coherent frequency-modulated continuous-wave (FMCW) LiDAR were previously discussed in Sec. 2.2.3, together with various system setups that have been proposed in the literature and their trade-offs. Also as mentioned before, one of the primary concerns for practical implementation of coherent LiDAR systems is cost-effectiveness. Therefore, in this chapter, a low-cost and low-complexity coherent FMCW LiDAR system is investigated, with a focus on the coherent receiver. Specifically, the single-photodiode (PD) based coherent LiDAR receiver is studied. As discussed in Sec. 2.2.3, this receiver architecture has the advantage of minimising the cost compared to a 90° optical hybrid-based coherent receiver or a 3-dB coupler-based balanced detection receiver. However, the system performance is affected by the unwanted direct detection (DD) beating interference (BI). The performance of two chirp signals that have been used for ranging, namely 1) the single-sideband (SSB) FMCW signal, and 2) double-sideband (DSB) amplitude-modulated chirp signal, is assessed using such a receiver. Mitigation of DD beating distortions by introducing a sufficiently wide spectral guard band to separate the desired signal from the DD distortions is investigated. In addition, the impact of laser phase noise on the receiver sensitivity performance is evaluated.

In this chapter, the modulation of these two chirp signals is presented in the

following Sec. 4.1.1. The theoretical analysis of the desired beat frequency and the unwanted DD beating terms in the single-photodiode based coherent receiver is presented in Sec. 4.1.2. Sec. 4.2 details the implementation of simulation and experimental setup, followed by a discussion of results in Sec. 4.3. Sec. 4.4 summarises the research findings presented in this chapter.

4.1 Operating principle

4.1.1 Signal modulation

As shown previously in Fig.2.13 and Eq.2.26, the linearly chirped sawtooth waveform is expressed as:

$$\cos(\varphi(t)) = \cos\left(2\pi f_1 t + \frac{\pi B t^2}{T_m}\right) \tag{4.1}$$

where $\varphi(t)$ denotes the instantaneous phase of the signal, varying as a function of time t, B represents the chirping bandwidth and T_m is the chirp period. f_1 denotes the start of the chirp frequency, and thus $0 - f_1$ is regarded as the guard band.

The schematic of the transmitter setup for generating a DSB signal is shown in Fig.4.1. The DSB chirp signal is obtained by amplitude modulation of the continuous wave (CW) laser via an electro-optic modulator (EOM) (e.g., a single-drive Mach-Zehnder modulator (MZM)). It is a real-valued signal with two sidebands which are the complex conjugate of each other, centered at the optical carrier frequency of f_c. The optical carrier can be suppressed by bias the MZM at the null point. The driving voltage applied to the MZM is expressed as:

$$V(t) = V_D \cos(\varphi(t)) \ = V_D \cos\left(2\pi f_1 t + \frac{\pi B t^2}{T_m}\right) \tag{4.2}$$

where V_D denotes the amplitude of the driving voltage $V(t)$. The transfer function of a MZM is given by [180]:

$$E_{\text{out}}(t) = E_{\text{in}}(t) \cos\left(\frac{\phi(t)}{2} + \phi_0\right), \quad \phi(t) = \frac{\pi V(t)}{V_\pi} \tag{4.3}$$

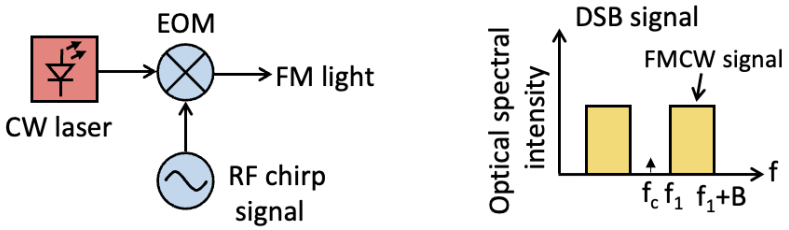

Figure 4.1: Schematic of the transmitter setup for generating DSB signal. CW: continuous wave; EOM: electro-optical modulator; RF: radio frequency; FM: frequency-modulated; DSB: double-sideband [45].

where $E_{\text{in}}(t)$ and $E_{\text{out}}(t)$ represent the input and output electrical fields of the incoming light, ϕ_0 represents the initial phase which is related to the direct current bias. The phase shift $\phi(t)$ between two arms of an MZM varies proportionally to the driving voltage $V(t)$. For a π phase shift, the corresponding driving voltage is V_π (i.e., $\phi(V_\pi) = \pi$).

It is assumed that the MZM is linearly modulated (i.e., $\frac{V_D}{V_\pi} \ll 1$) and operates at the minimum transmission point ($\phi_0 = -\frac{\pi}{2}$) to suppress the optical carrier. Substituting Eq.4.2 into Eq.4.3, the generated double-sided sawtooth waveform at the output of the MZM is given as:

$$\begin{aligned} E_{\text{out}}(t) &= E_{\text{in}}(t)\cos\left(\frac{\pi V_D}{2V_\pi}\cos(\varphi(t)) - \frac{\pi}{2}\right) \\ &\approx E_{\text{in}}(t)\cos(\varphi(t)) \end{aligned} \tag{4.4}$$

If the incoming optical light $E_{\text{in}}(t)$ of the MZM is corrupted by laser phase noise, then Eq.4.4 is expressed as:

$$E_{\text{out}}(t) = E_{\text{in}}(t)\cos(\varphi(t)) = A\cos(\varphi(t))\, e^{j(\omega_c t + \theta(t))} \tag{4.5}$$

where A and ω_c denote the amplitude and the angular carrier frequency ($\omega_c = 2\pi f_c$) of the laser source, $\theta(t)$ is the laser phase noise.

The generation of SSB FMCW signal requires an in-phase and quadrature modulator (IQM). Fig.4.2 displays the schematic of SSB chirp signal generation with the in-phase (I) and quadrature (Q) components of the IQM being

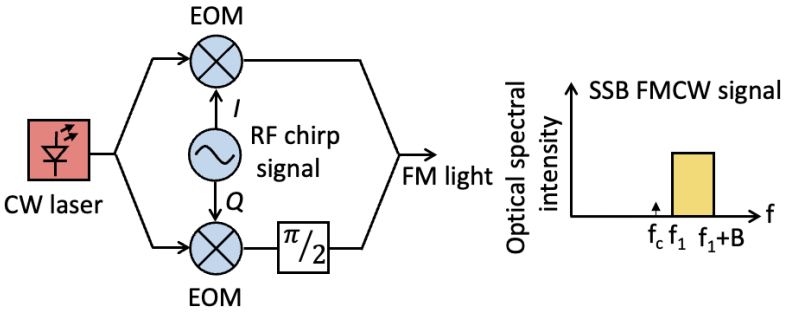

Figure 4.2: Schematic of the transmitter setup for generating SSB signal. CW: continuous wave; EOM: electro-optical modulator; I: in-phase; Q: quadrature; RF: radio frequency; FM: frequency-modulated; SSB: single-sideband [45].

independently modulated [45, 159]. The SSB signal is complex-valued. It has a constant intensity with one modulation sideband, which can be loaded onto either side of the optical carrier. The real and imaginary parts of an SSB signal are related to each other by the Hilbert transform. The driving voltages applied to the IQM are defined as:

$$V_I(t) = V_D \cos(\varphi(t)), \quad V_Q(t) = V_D \sin(\varphi(t)) \tag{4.6}$$

The transfer function of an IQM is given by [180]:

$$E_{\text{out}}(t) = \frac{1}{2} E_{\text{in}}(t) \left(\cos\left(\frac{\phi_I(t)}{2}\right) + j \cos\left(\frac{\phi_Q(t)}{2}\right) \right) \tag{4.7}$$

where $\phi_I(t) = \frac{\pi V_I(t)}{V_\pi}$ and $\phi_Q(t) = \frac{\pi V_Q(t)}{V_\pi}$, j denotes the $\frac{\pi}{2}$ phase shift induced on the light passing through one of the two EOMs in the IQM and the factor of $\frac{1}{2}$ indicates the 50/50 splitting ratio.

Similarly to the case with the DSB signal, the IQM is assumed to be biased at the minimum transmission point and to operate in the linear region. Combining Eq.4.6 and Eq.4.7, the generated SSB FMCW signal at the output of IQM given by:

$$\begin{aligned} E_{\text{out}}(t) &= \frac{1}{2} E_{\text{in}}(t)(\cos(\varphi(t)) + j \sin(\varphi(t)) \\ &= \frac{1}{2} A e^{j(\omega_c t + \varphi(t) + \theta(t))} \end{aligned} \tag{4.8}$$

It should be mentioned that, though the DSB signal is an amplitude-modulated signal, its operating principle is very similar to that of SSB FMCW signal. Hence,

the amplitude-modulated DSB signal is also referred to as a kind of FMCW signal in the literature [79, 80]. In the frequency domain, the lower sideband of the DSB signal is the complex conjugate of the upper sideband. Each modulation sideband on its own is an SSB FMCW signal as indicated in Fig.4.1.

4.1.2 Beating products

In order to have sufficient power for transmission, the chirp signal can be further amplified after generation, for example by an EDFA [34, 80]. In the system setups presented in this thesis, optical mixing is adopted where the chirp signal is chosen as the local oscillator (LO) as this technique offers a much simpler receiver (Rx) configuration as discussed in Sec.2.2.3. Hence, at the transmitter end, the amplified signal is split into two pathways, one as the LO and the other one as the out-going signal directed at the target. In this case, both the transmitted signal and LO are corrupted by ASE noise. A 3-dB coupler is used at the receiver to combine the LO and the back-reflected Rx signal. The Rx signal is time-delayed by τ depending on the round-trip delay (see Fig.2.13). The optical field at the output of the coupler is:

$$E = \frac{1}{\sqrt{2}}\Big[E_{\mathrm{LO}} + E_{\mathrm{ASE(LO)}} + j(E_{\mathrm{Rx}} + E_{\mathrm{ASE(Rx)}})\Big] \tag{4.9}$$

where E_{LO} and E_{Rx} represent the ASE-noise-free LO and Rx signal, $E_{\mathrm{ASE(LO)}}$ and $E_{\mathrm{ASE(Rx)}}$ denote the ASE noise from the LO and Rx signal. Following single-photodiode square-law detection, the detected photocurrent can be described as:

$$\begin{aligned} I_{\mathrm{PD}} &\propto \mathrm{R}|E|^2 \\ &\propto \frac{\mathrm{R}}{2}\Big(\underbrace{|E_{\mathrm{LO}}|^2}_{\text{LO-LO beating}} + |E_{\mathrm{Rx}}|^2 + |E_{\mathrm{ASE(LO)}}|^2 + |E_{\mathrm{ASE(Rx)}}|^2 \\ &\quad + \underbrace{2\,\mathrm{Re}\left[E_{\mathrm{LO}}E^*_{\mathrm{ASE(LO)}}\right]}_{\text{LO-ASE beating}} + 2\,\mathrm{Re}\left[E_{\mathrm{Rx}}E^*_{\mathrm{ASE(Rx)}}\right] \\ &\quad + \underbrace{2\,\mathrm{Im}\left[E_{\mathrm{Rx}}E^*_{\mathrm{LO}}\right]}_{\text{LO-signal beating}} + 2\,\mathrm{Im}\left[E_{\mathrm{ASE(Rx)}}E^*_{\mathrm{LO}}\right] \\ &\quad + 2\,\mathrm{Im}\left[E_{\mathrm{ASE(Rx)}}E^*_{\mathrm{ASE(LO)}}\right] + 2\,\mathrm{Im}\left[E_{\mathrm{Rx}}E^*_{\mathrm{ASE(LO)}}\right]\Big) \end{aligned} \tag{4.10}$$

where R is the PD responsivity, the asterisk denotes complex conjugation, and Re$[x]$ and Im$[x]$ represent the real and imaginary parts of x. In Eq.4.10, LO-signal beating is the desired beating component which contains the beat frequency. All the other beating products are unwanted interference which will degrade the receiver sensitivity. In particular, as the LO is often very strong in the coherent detection scheme, the LO-ASE beating interference (LO-ASE BI, broadband white noise) and LO-LO beating interference (LO-LO BI, related to the LO waveform) will fundamentally limit the receiver sensitivity.

In the case of the amplitude-modulated DSB signal, the desired LO-signal beating product is given by:

$$\begin{aligned} I^{\mathrm{DSB}}_{\text{LO-signal}} &\propto \mathrm{R}\,\mathrm{Im}\left[E_{\mathrm{Rx}}E^{*}_{\mathrm{LO}}\right] \\ &\propto \mathrm{R}A_{\mathrm{Rx}}A_{\mathrm{LO}}\cos(\varphi(t-\tau))\cos(\varphi(t))\sin(\Delta\theta(t)) \\ &\propto \frac{1}{2}\mathrm{R}A_{\mathrm{Rx}}A_{\mathrm{LO}}\sin(\Delta\theta(t)) \\ &\quad\times\Big[\cos(\Delta\varphi(t))+\cos(\varphi(t-\tau)+\varphi(t))\Big] \end{aligned} \tag{4.11}$$

where A_{LO} and A_{Rx} represent the amplitude of the LO and Rx signal respectively, and $\cos(\Delta\varphi(t))$ denotes the desired component at the beat frequency which is the frequency offset between the LO and the reflected Rx signal. $\cos(\varphi(t-\tau)+\varphi(t))$ represents a beating image, corresponding to the sum of the frequencies of the LO and Rx signal. $\Delta\theta(t)$ refers to the difference of laser phase noise between the LO and Rx signal. This is converted into amplitude noise after photodetection, introducing a power fluctuation to the desired beat signal. When the LO and Rx signals are in phase, the amplitude of the LO-signal beating product can be zero in the case of perfect phase noise correlation (i.e., $\Delta\theta(t)=0$). The LO-LO beating interference when using the DSB signal is:

$$\begin{aligned} I^{\mathrm{DSB}}_{\text{LO-LO BI}} &\propto \frac{\mathrm{R}}{2}|E_{\mathrm{LO}}|^{2} \\ &\propto \frac{\mathrm{R}}{2}|A_{\mathrm{LO}}\cos(\varphi(t))|^{2} \\ &\propto \frac{1}{4}\mathrm{R}A^{2}_{\mathrm{LO}}\Big(1+\cos(2\varphi(t))\Big) \end{aligned} \tag{4.12}$$

It can be seen in Eq.4.12, for a DSB signal, the LO-LO BI manifests as a constant direct current (DC) term plus a nonlinear beating interference which starts at a frequency of $2f_1$ and has twice the bandwidth of the original chirp signal. While the DC component can be easily filtered out using a DC blocker or removed digitally in the receiver DSP, this nonlinear interference will distort any desired LO-signal beating products that fall within the same frequency range. Therefore, as a way of mitigating the penalty of LO-LO BI, a spectral guard band is used to separate the desired beating products from the nonlinear LO-LO BI. For a sawtooth waveform considered in this work, the maximum possible delay is equal to half of the pulse period, avoiding the interference from the second beating tone caused by the discontinuity of the sawtooth waveform as mentioned in Sec.2.2.3 [181]. This leads to a maximum beat frequency f_b of $\frac{B}{2}$. Therefore, a minimum guard band of $\frac{B}{4}$ is necessary in order to mitigate LO-LO BI (i.e., $f_1 > \frac{B}{4}$).

In contrast, for an SSB FMCW signal, the desired LO-signal beating product is given by:

$$\begin{aligned} I^{\text{SSB}}_{\text{LO-signal}} &\propto \text{R}\,\text{Im}\left[E_{\text{Rx}}E^{*}_{\text{LO}}\right] \\ &\propto \text{R}\,\text{Im}\left(A_{\text{Rx}}A_{\text{LO}}e^{j(\Delta\varphi(t)+\Delta\theta(t))}\right) \\ &\propto \text{R}A_{\text{Rx}}A_{\text{LO}}\sin(\Delta\varphi(t)+\Delta\theta(t)) \end{aligned} \tag{4.13}$$

After photodetection, the phase noise variation $\Delta\theta(t)$ between the LO and Rx signal is added to the desired beat frequency. However, provided the round-trip-distance is within the laser coherence length, this phase noise variation will be negligible (i.e., $\Delta\theta(t) \approx 0$). The LO-LO BI in the case of the SSB signal is expressed as:

$$\begin{aligned} I^{\text{SSB}}_{\text{LO-LO BI}} &\propto \frac{\text{R}}{2}|E_{\text{LO}}|^2 \\ &\propto \frac{\text{R}}{2}|A_{\text{LO}}e^{j(\varphi(t)+\theta(t))}|^2 \\ &\propto \frac{1}{2}\text{R}A^2_{\text{LO}} \end{aligned} \tag{4.14}$$

As the SSB signal is only frequency/phase modulated and complex-valued, the LO-LO BI after photodetection is simply a constant DC component as shown in

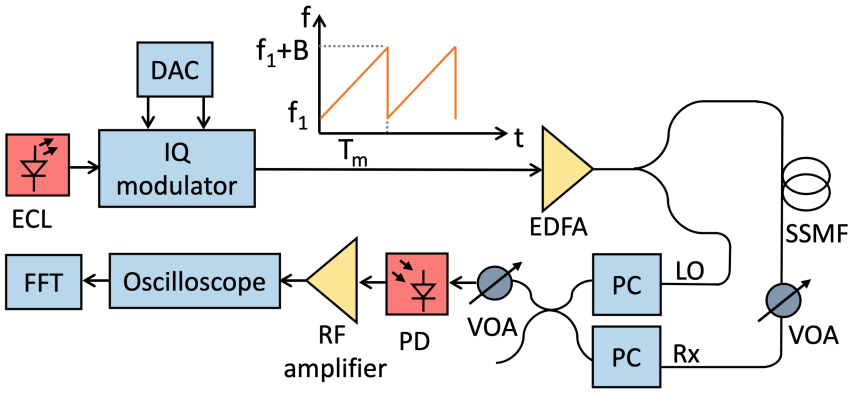

Figure 4.3: System setup of single-photodiode based coherent LiDAR. ECL: external cavity laser; IQ: in-phase and quadrature; DAC: digital-to-analog converter; EDFA: Erbium-doped fibre amplifier; SSMF: standard single-mode fibre; VOA: variable optical attenuator; LO: local oscillator; Rx: received signal; PC: polarisation controller; PD: photodiode; RF: radio frequency; FFT: fast Fourier transform.

Eq.4.14, which can be easily filtered out, and thus the LO-LO BI is avoided, whether or not a guard band is used.

4.2 Experimental and simulation setups

To investigate the impact of DD distortions arising from single-photodiode detection, especially the LO-LO BI, on the receiver sensitivity of a coherent LiDAR system, the setup shown in Fig.4.3 was employed for both Monte Carlo simulations and experimental demonstration.

In the experiment, an optical delay line L of 384.72 m of standard single-mode fibre (SSMF) with an effective refractive index n of approximately 1.5 was used to emulate the time-of-flight of the signal [75, 159]. At the transmitter, an external cavity laser centered at 1551.12 nm was used. It had an output power of 9.6 dBm and a laser linewidth of approximately 100 kHz. The laser coherence length was approximately 637 m in the SSMF, and thus the delay line was well within the coherence length [75]. The ECL was externally modulated via IQM (Oclaro 6M0C6400) driven by DAC sampling at 92 GSa/s. The extinction ratio of the IQM was approximately 40 dB. For the sawtooth chirp signal, the pulse period T_m was set as 5 µs and the chirping bandwidth $B = 5$ GHz. For the optical delay line of 384.72 m, the corresponding beat frequency $f_b = \frac{LnB}{cT_m} \approx 1.92$ GHz. In order to

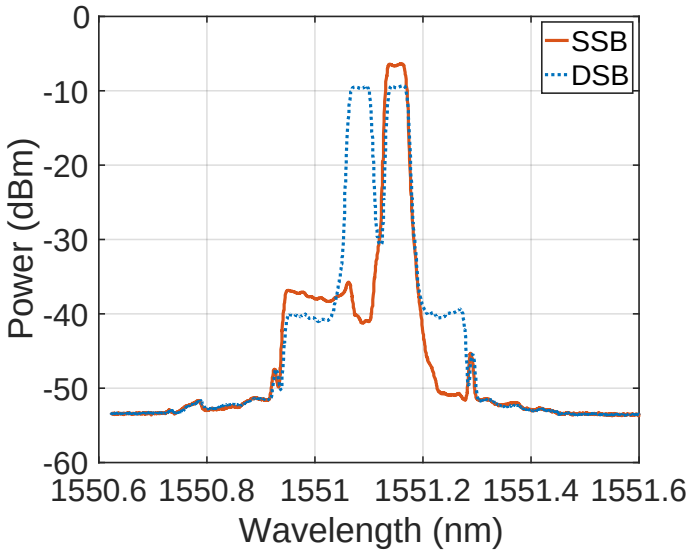

Figure 4.4: Transmitted DSB and SSB signals (2 GHz guard band, 5 GHz chirp) measured by an optical spectrum analyzer at 0.01 nm resolution bandwidth.

investigate how LO-LO BI affects Rx sensitivity, two values of guard band width were assessed: 0 and 2 GHz (i.e., $f_1 = 0$ GHz and $f_1 = 2$ GHz). As discussed in Sec. 4.1.1, Eq.4.6 was used to drive the IQM to generate the complex-valued SSB signal. For the DSB signal, both arms of the IQM were driven by the same waveform (Eq.4.2) in order to achieve the same output power as the SSB signal. The peak-to-peak driving voltage was set to approximately 1 V_π to maximise the output power after modulation. The modulated optical signal was then amplified to 17.3 dBm by an EDFA with a noise figure of 5.5 dB.

An example of the transmitted signal spectra (2 GHz guard band, 5 GHz chirping bandwidth) is shown in Fig.4.4, measured using an optical spectrum analyser (OSA) at a resolution bandwidth of 0.01 nm. For both SSB and DSB signals, a noise pedestal (15 GHz) which is about 30 dB lower than the signal power is observed to the side of the desired 5 GHz chirp spectra. This was caused by modulator nonlinearity, introducing a modulation sideband. The signal was then split by a 3-dB splitter into two paths; one for signal transmission and the other to serve as the LO at the receiver. A variable optical attenuator (VOA) was added before the receiver to adjust the received signal power.

At the receiver, the polarisation states of the Rx signal and LO were first

aligned by two polarisation controllers (PCs) to maximise the beating [34, 155], and then combined in a 3-dB coupler. The LO power at the input of the 3-dB coupler was 13.4 dBm and the Rx signal power was swept from -10.6 dBm to -66.8 dBm with a step size of -5 dB. A 6-dB optical attenuator was applied before the PD to reduce the total incident optical power below its maximum input power. In order to show the full-spectrum of the signal and DD beating interference, a PD with a bandwidth of 15 GHz was used with 0.6 A/W responsivity, followed by a radio frequency (RF) amplifier with 17 dB gain. Finally, the signal was digitised by a real-time oscilloscope sampling at 50 GSa/s. At each Rx power, 100 measurements were saved to test the reliability of DSB and SSB signals, each of 250,000 sampling points (i.e., one pulse period of 5 μs). A Fourier transform was applied off-line using MATLAB. The desired beat frequency f_b was extracted by identifying the beating tone with the highest power in the frequency domain, and converted into the distance through $L = \frac{f_b c T_m}{nB}$.

Monte Carlo simulations were also carried out using MATLAB, with the system structure and parameters used in the experiments as described above. The laser phase noise was modelled as a random walk, specifically the Wiener process described by [182]:

$$\theta(t) - \theta(t - \Delta t) \sim \mathcal{N}(0, 2\pi\Delta v\Delta t) \tag{4.15}$$

where Δt indicates a small time offset and Δv denotes the laser linewidth which was 100 kHz in simulation. $\mathcal{N}(0, 2\pi\Delta v\Delta t)$ denotes a normal distribution with zero mean and the variance of $2\pi\Delta v\Delta t$. As with the experiments, at each distance and received signal power, 100 simulations were performed.

4.3 System performance

4.3.1 Impact of LO-LO BI via Monte Carlo Simulations

In simulation, a sufficiently wide guard band was first employed to ensure LO-LO BI terms fell at frequencies outside the desired signal band (i.e., f_1 = 2 GHz), and

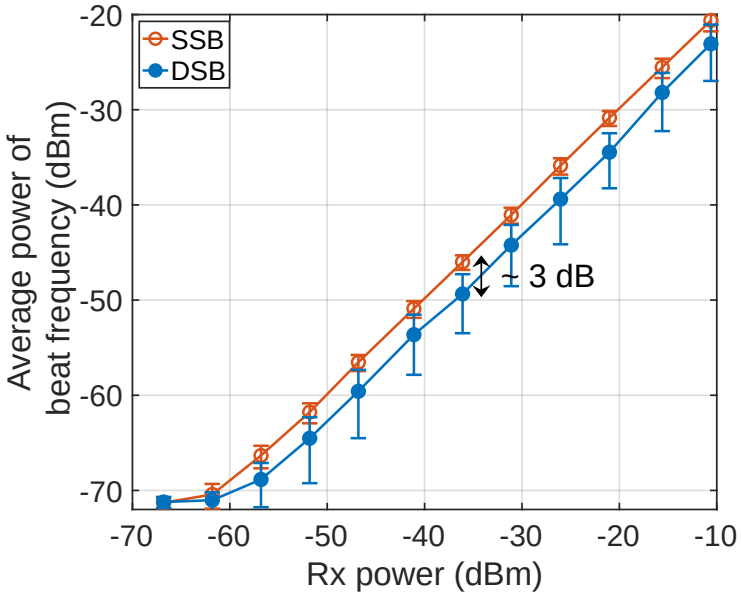

Figure 4.5: Simulated average power at the beat frequency versus Rx power for DSB and SSB signals. The vertical error bars indicate the standard deviation of the beat frequency power.

thus the system performance was limited by LO-ASE beating interference. The simulated average power at the beat frequency versus Rx power is displayed in Fig.4.5. The vertical bar at each Rx power represents the standard deviation of the beat frequency power over 100 simulations. It can be seen that the DSB signal experiences much greater power fluctuation than the SSB signal. This is explained by Eq.4.11 which suggests that for the DSB signal, the laser phase noise is converted to amplitude noise after photodetection. Such fluctuation leads to a $\sim$3 dB reduction of the average power of the beat frequency over 100 simulations compared to that of the SSB signal.

The power fluctuation in the case of the DSB signal might not be an issue when the Rx power is sufficiently high as the desired beat frequency can still be discerned from the noise floor. Nevertheless, at low Rx powers, e.g., for targets at long distances, the power of the beat frequency might fall below the noise floor and thus the distance estimation will not always be reliable. Fig.4.6(a) shows the standard deviation of the distance estimation as a function of the Rx power obtained by the Monte Carlo simulations. The inset shows an example of frequency-domain power spectra of the detected photocurrent for DSB and SSB signals at the Rx power of

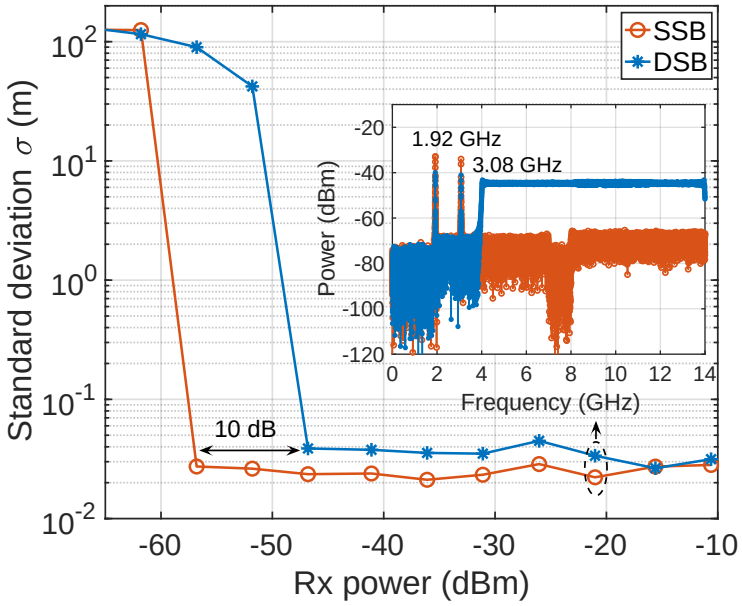

(a)

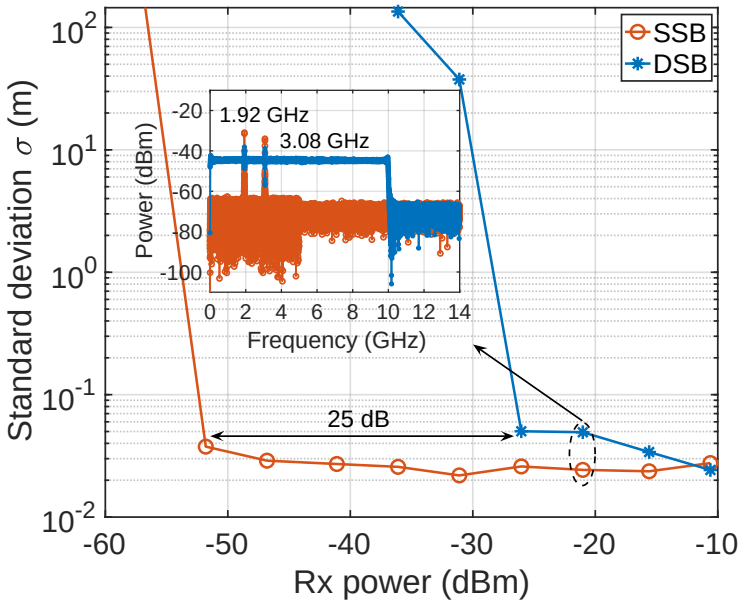

(b)

Figure 4.6: Simulated standard deviation of distance estimation versus Rx power with (a) 2 GHz guard band, and (b) without guard band. The inset in each figure shows the frequency-domain spectra of SSB and DSB signals.

−21.02 dBm in simulation. The desired beat frequency is at 1.92 GHz. The beating tone at 3.08 GHz is due to the discontinuity of the sawtooth waveform [181]. For the DSB signal, the nonlinear LO-LO BI is observed over the range from 4 to 14 GHz with twice the bandwidth of the signal's 5 GHz chirp as explained by Eq.4.12, and it is approximately 25 dB higher than the LO-ASE BI limited noise floor. For the SSB signal, the LO-LO BI is simply a DC term as suggested by Eq.4.14. As the DC component can be easily filtered out, the mean of detected signal waveforms was subtracted in the simulation to achieve the same effect, and that is why the DC term which should be at zero frequency is not present in the frequency-domain spectra for both DSB and SSB signals. Ideally, the LO-ASE noise floor is the broad-band white noise with a constant power spectral density. However, in order to replicate the actual experimental setup, a non-ideal modulator with an extinction ratio of approximately 40 dB was assumed [183], and modulation nonlinearity was also included in the simulation. This limited extinction ratio of the modulator leads to a weak residual carrier beating with the signal on reception, accounting for the additional noise from 2−7 GHz (around 5 dB higher than LO-ASE BI noise floor) with the same bandwidth as the chirp signal. The extra noise at frequencies above 8 GHz is caused by the nonlinearity of the modulator. Note that both these distortions exist in the DSB signal power spectrum but are masked by the dominant LO-LO BI in the high-frequency regime. In this case, with a sufficient guard band, the unwanted LO-LO BI is not at the same frequency range as the desired beat signal. In practice, a low-bandwidth PD can be used and this DD interference will fall outside the detection range and will not cause a receiver sensitivity penalty.

As shown in the plot of standard deviation versus Rx power in Fig.4.6(a), at Rx powers higher than −46.8 dBm, both DSB and SSB signals can accurately predict the distance, showing a standard deviation of distance estimation of approximately 0.03 m. As the Rx power decreases, for the DSB signal, the power fluctuation causes several inaccurate distance estimations over the 100 simulations and thus the standard deviation starts to increase. In contrast, the SSB signal demonstrates 10 dB better receiver sensitivity, and can operate reliably with Rx signal powers down to

−56.8 dBm.

To assess the impact of DD interference, the guard band was removed such that the LO-LO BI overlapped with the desired beat signal band in the frequency domain as shown in the inset of Fig.4.6(b). Compared to the results with the 2 GHz guard band given in Fig.4.6(a), the minimum Rx power for the SSB signal increases from −56.8 dBm to −51.8 dBm due to residual-carrier beating with the signal; a 5 dB penalty in receiver sensitivity. For the DSB signal, however, as the LO-LO BI is unmitigated, a 20 dB receiver sensitivity penalty is measured (i.e., from −46.8 dBm with a 2 GHz guard band to −26.04 dBm without a guard band). Therefore, in this case without a guard band, the SSB signal shows 25 dB better receiver sensitivity than the DSB signal.

4.3.2 Impact of LO-LO BI via experimental demonstration

Experiments were also carried out and the results were compared with the simulation results. Fig.4.7 shows the experimental average power at the desired beat frequency versus Rx power for DSB and SSB signals. Similarly to the simulation results in Fig.4.5, the DSB signal experiences a higher power fluctuation shown by the larger standard deviation at each received signal power level. This leads to a ∼4 dB reduction of the average beat signal power over 100 measurements compared to that of SSB signal. Note that at each Rx power, there is a small discrepancy in the average powers between the experimental and simulated results. This might be caused by the non-ideal polarisation alignment in the experiment which was manually tuned with the polarisation controller, leading to a reduction of approximately 2 dB in the average power of the beat frequency.

Fig.4.8(a) and (b) present, from the experiments, the standard deviation of the distance estimation as a function of Rx power with a 2 GHz guard band and without a guard band, respectively. The inset in each figure shows the experimental frequency-domain spectra of the SSB and DSB signals at the Rx power of −21.02 dBm. Each spectrum looks similar to the simulated one shown in Fig.4.6. Despite the main nonlinear interference such as LO-LO BI and the penalty from the non-ideal modulator which are also observed in the simulation, a few

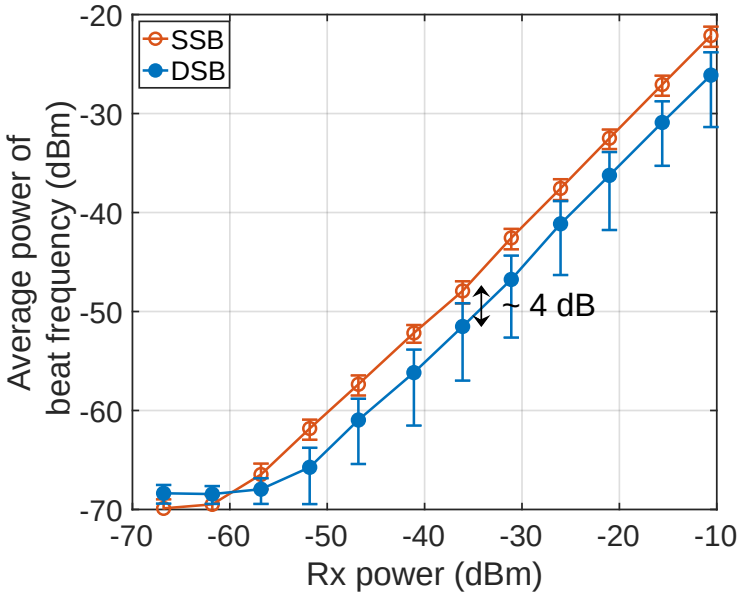

Figure 4.7: Experimental average power at the beat frequency versus Rx power for DSB and SSB signals. The vertical error bars indicate the standard deviation of the beat frequency power.

spectral components at frequencies below 600 MHz occur only in the experimental spectra for both DSB and SSB signals. As those components, which are generated by the transceiver are constant for all measurements, they can be removed through system calibration. Thus, in order to assess the limitation due to the LO-ASE beating noise floor, only frequency components between 600 MHz and 2 GHz were measured to identify the desired beat frequency.

In the case with a sufficiently wide guard band as shown in Fig.4.8(a), there is a 10 dB sensitivity difference between SSB and DSB signals, the same as that observed in the simulation results shown in Fig.4.6(a), and this is due to the phase noise induced power fluctuation of the DSB signal. Removing the guard band so that the LO-LO BI falls within the frequency range of the desired beat signal as plotted in the inset of Fig.4.8(b), the sensitivity difference between the DSB and SSB signals therefore increases to 25 dB. It should be noted that though the sensitivity difference between the DSB and SSB signals is the same as the simulation, the experimental results show a 5 dB worse receiver sensitivity than the simulation (e.g., with a 2 GHz guard band: the Rx sensitivity is -56.8 dBm for SSB signal in simulation and -51.8 dBm in experiment; for DSB signal: -46.8 dBm

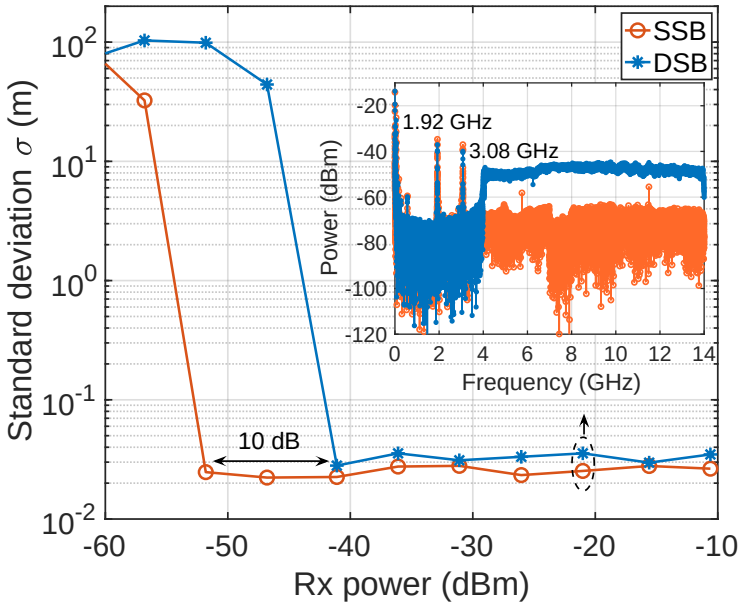

(a)

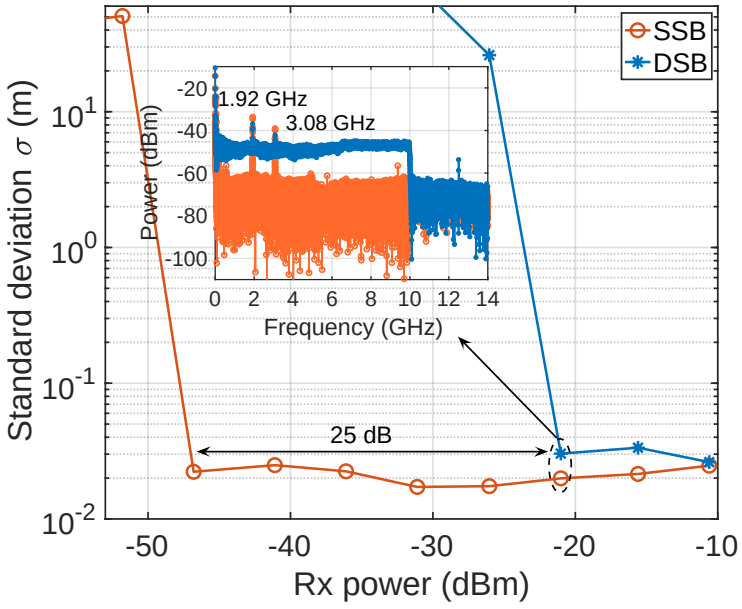

(b)

Figure 4.8: Experimentally measured standard deviation of distance estimation versus Rx power with (a) 2 GHz guard band, and (b) without guard band. The inset in each figure shows the frequency-domain spectra of SSB and DSB signals.

in simulation and −41.1 dBm in experiment. The same offset is observed in the case without a guard band.). In addition to the measurements with a delay line of 384.72 m, giving the above results, measurements with a delay line of 238.28 m were also carried out, and a similar performance was observed in both simulations and experiments.

4.3.3 Impact of laser phase noise on receiver sensitivity

So far, the penalties of DD distortions specifically the LO-LO BI were discussed through both numerical and experimental results. For the DSB signal, when the LO-LO BI is mitigated through the use of a spectral guard band, its receiver sensitivity is still affected by laser phase noise induced power fluctuation as suggested by Eq.4.11 even within the laser coherence length. Such power fluctuation leads to a 10 dB receiver sensitivity penalty at a delay length of 384.72 m compared to that observed with the SSB signal as shown in Fig.4.6(a) and Fig.4.8(a). It is also indicated by Eq.4.11 that, the shorter the delay line is, the more coherent is the laser phase noise between the LO and Rx signal. As phase noise is converted to amplitude noise after photodetection, a higher power fluctuation and thus a worse receiver sensitivity would be expected at a shorter delay length, making the DSB signal less reliable. In contrast, for the SSB signal as suggested by Eq.4.13, reducing the delay results in the relative phase noise difference between the LO and Rx signal approaching zero. In the frequency domain, the spectral broadening due to laser phase noise therefore will be smaller, and the majority of the desired beat signal power will be centered around a single beat frequency leading to a more accurate distance estimation.

In order to evaluate how such phase noise coherence affects the receiver sensitivity of DSB and SSB signals, more experiments were conducted by decreasing the delay line to 238.28 m, 131.56 m, 63.24 m and 43.68 m. All the measurements were performed with 5 GHz chirping bandwidth and 2 GHz guard band mitigating the penalty from LO-LO BI, so the system performance was limited by the LO-ASE beating noise floor. Extensive Monte Carlo simulations were also carried out with the delay line varying from 20 m to 395 m. The maximum beat

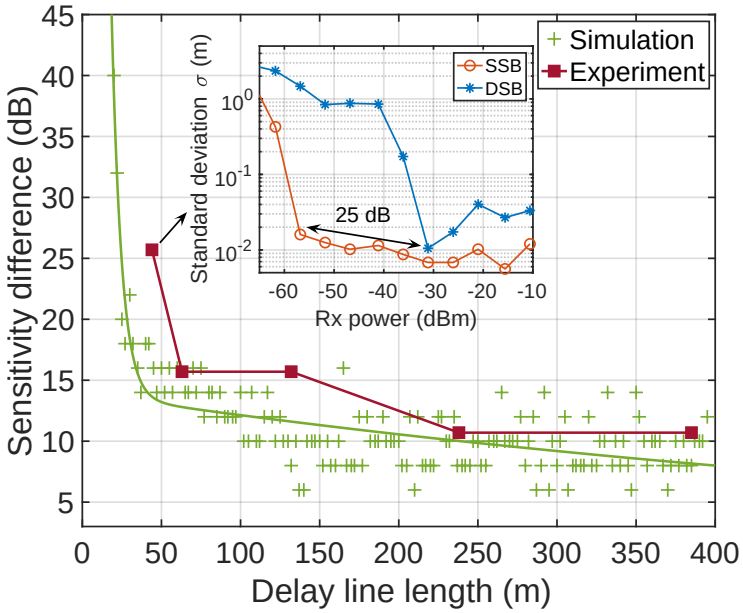

Figure 4.9: Receiver sensitivity difference between DSB and SSB signals versus delay line length. The green solid line is the nonlinear fitted curve of the simulation results. The inset shows the experimental standard deviation of distance estimation versus Rx power at the delay line length of 43.68 m.

frequency at 395 m is 1.975 GHz, which is still within the 2 GHz guard band ensuring the LO-LO BI will not interfere with the desired beat signal. The received signal power was varied from -10.6 dBm, decreased in steps of 2 dB down to -66.6 dBm.

The receiver sensitivity difference between DSB and SSB signals with varying delay length is shown in Fig.4.9. The simulation results show that at a shorter delay length, for example, at 20 m, there is a 40 dB sensitivity difference between DSB and SSB signals. As the delay increases, the sensitivity difference decreases and levels out at around 10 dB with distances above 100 m. The experimental results show a similar trend with a higher sensitivity difference between DSB and SSB signals at shorter delay distances. For example, the inset of Fig.4.9 plots the standard deviation of distance estimation versus received signal power at a delay line length of 43.68 m and the result indicates a 25 dB sensitivity difference. Increasing the delay, the sensitivity difference gradually flattens out to approximately 10 dB at delay line distances of 238.28 m and 384.72 m. The reason for this larger sensitivity difference at a shorter delay distance is two-fold.

On the one hand, the SSB signal achieves a better sensitivity at shorter distances as the phase noise variation becomes negligible, e.g., −56.8 dBm at 43.68 m and −51.8 dBm at 384.72 m (see Fig.4.8(a)). On the other hand, the beating signal power fluctuation with the DSB signal is larger due to the increased coherence of the phase noise between LO and Rx signal, and thus the required Rx power increases from −41.1 dBm at 384.72 m (see Fig.4.8(a)) to −31.1 dBm at 43.68 m. The results may suggest that with reducing distance to the target, the DSB signal requires increasing Rx power to allow the desired beat tone to be identified. In practice for a LiDAR system, the received signal after being reflected from a close target usually has a higher power than one reflected from a more distant target, and therefore, such power fluctuation of the DSB signal might not be a major issue.

It should be noted that the above results were obtained using an optical fibre delay line to emulate the time-of-flight. The interference from free-space environment, in which LiDAR is usually operated, may degrade the quality of the received signal. Nevertheless, as the LO-LO BI is only related to the LO, and not to the received signal, it will always be present in this single-photodiode based coherent LiDAR configuration regardless of the interference from free space. Therefore, compared to the DSB signal, the receiver sensitivity benefit offered by the SSB signal would still be expected in free-space operation.

4.4 Summary

In this chapter, the performance of two chirp signals: the single-sideband (SSB) frequency-modulated continuous-wave (FMCW) signal and the double-sideband (DSB) amplitude-modulated signal in a coherent LiDAR system with single photodiode detection was evaluated. The impact of direct-detection beating distortions and laser phase noise on the receiver sensitivity performance was mathematically analysed first, following which simulations and experiments were performed for verification with a good agreement achieved. The results indicate that the real-valued DSB signal suffers a significant receiver sensitivity penalty from nonlinear LO-LO beating interference (BI) and requires a sufficiently wide

spectral guard band to mitigate LO-LO BI, achieved at the expense of requiring a larger electrical bandwidth. In addition, the DSB signal is susceptible to power fluctuation caused by laser phase noise after photodetection, making it less reliable especially at shorter delay lengths.

These two main drawbacks associated with the DSB signal can be overcome through the use of a complex-valued SSB FMCW signal, at the expense of using a more complex in-phase and quadrature modulator (IQM) at the transmitter. For the SSB signal, the LO-LO BI is just a DC component which can be easily filtered out. Thus, a guard band is not necessary and the entire electrical bandwidth can be utilised for the chirp signal to achieve a better resolution. In addition, the use of an SSB signal with a single-photodiode based coherent receiver does not suffer from phase noise to amplitude noise conversion, which significantly relaxes the requirement for the received signal power. In both simulations and experiments, with a frequency chirp bandwidth of 5 GHz, and with no guard band, the SSB FMCW signal is shown to outperform the DSB signal-based system with 25 dB better receiver sensitivity at a delay line length of 384.72 m. Therefore, the SSB FMCW signal is shown to be a strong candidate for single-photodiode based coherent LiDAR system.

It should be noted that the above work focuses on the investigation of the performance of coherent LiDAR receivers with single-ended photodetection as it is low-cost and low-complexity, suitable for cost-sensitive LiDAR applications. To further reduce the cost and size of the current system, it is also possible to replace the transmitter EDFA by a semiconductor optical amplifier (SOA) [184] or a compact micro EDFA [185,186]. Nonetheless, the above results should provide some general insights into cost-effective coherent LiDAR system designs.

Chapter 5

Impact of laser phase noise on ranging precision

In the previous chapter, the receiver sensitivity performance of a low-cost and low-complexity single-photodiode based coherent LiDAR receiver was assessed. The simulation and experimental results show that the single-sideband (SSB) frequency-modulated continuous-wave (FMCW) signal has a higher tolerance to laser phase noise and local oscillator-local oscillator beating interference (LO-LO BI) than the double-sideband (DSB) amplitude-modulated signal. Apart from the coherent receiver, the laser also forms a critical component of a LiDAR system. As discussed previously in Sec. 2.2.3, the maximum ranging distance is usually assumed to be limited by the laser coherence length. When operating in an incoherent region, the laser phase noise causes a spectral broadening of the detected beat signal. This leads to variations in identifying the beat frequency, and thus degrading the ranging precision. Therefore, for long-distance ranging ($>$100 m), a low-linewidth laser is preferable, which will inevitably increase the system cost, especially below laser linewidth of 100 kHz.

Though certain degradations of ranging precision would be expected beyond the laser coherence length, the use of a relatively high-linewidth laser source might be a compromise solution for some cost-sensitive applications if the performance is acceptable. Therefore, in this chapter, through both experiments and simulations, penalties arising from the laser phase noise on the ranging precision when operating

within and beyond the laser coherence length are assessed. Sec. 5.1 presents, through experiments, the ranging precision at different delay distances when using 100 kHz and 1.2 MHz linewidth laser sources. More extensive simulation results with varying laser linewidths and delays are discussed in Sec. 5.2, followed by a summary of the research work presented in this chapter in Sec. 5.3.

5.1 Ranging precision of 100 kHz and 1.2 MHz lasers

The same system setup shown in the last chapter in Fig.4.3 was employed to assess the ranging precision. The SSB FMCW signal type was chosen, as it does not suffer from phase noise to amplitude noise conversion as investigated in the last Chapter. In order to evaluate the impact of laser phase noise, lasers with linewidths Δv of 100 kHz and 1.2 MHz were used in experiments both with an output power of 9.6 dBm. The corresponding coherence lengths are approximately 53 m and 637 m in the standard single-mode fibre (SSMF), given by $L_{coh} = \frac{c}{n\pi\Delta v}$ where c is the speed of light, and n is the refractive index of the SSMF [75]. The fibre delay length L was varied from 43.68 m to 384.72 m to evaluate the impact of laser phase noise on the ranging precision in experiments.

The received signal power was set to -21 dBm across all the measurements to ensure that the beat signal could always be discerned from the noise floor. One hundred traces were saved at each distance. The ranging precision was quantified by the standard deviation σ of the estimated distance over 100 measurements.

Fig.5.1 shows the frequency-domain power spectra of detected beat signals at a delay line $L = 238.28$ m, exhibiting a beat frequency of 1.19 GHz. With a laser linewidth of 100 kHz, 238.28 m is still within the coherence length ($\frac{L}{L_{coh}} \approx 0.37$). The laser phase noise from the LO and the delayed copy are almost correlated, and close to canceling each other, resulting in a relatively narrow beat tone (see Eq.4.13 in the last chapter). In the case of the 1.2 MHz laser source, however, the incoherent measurement ($\frac{L}{L_{coh}} \approx 4.5$) causes spectral broadening in the frequency domain as can be seen in Fig.5.1. This leads to increased uncertainty in identifying the center frequency of the beat signal and thus reduces the ranging precision. Fig.5.2 shows

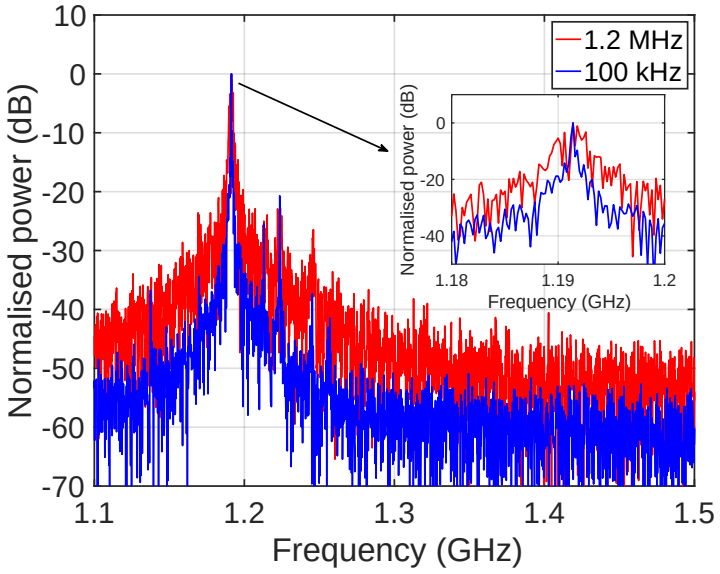

Figure 5.1: At a delay line $L = 238.28$ m, the normalised frequency-domain power spectra of detected beat signals using 1.2 MHz and 100 kHz laser sources.

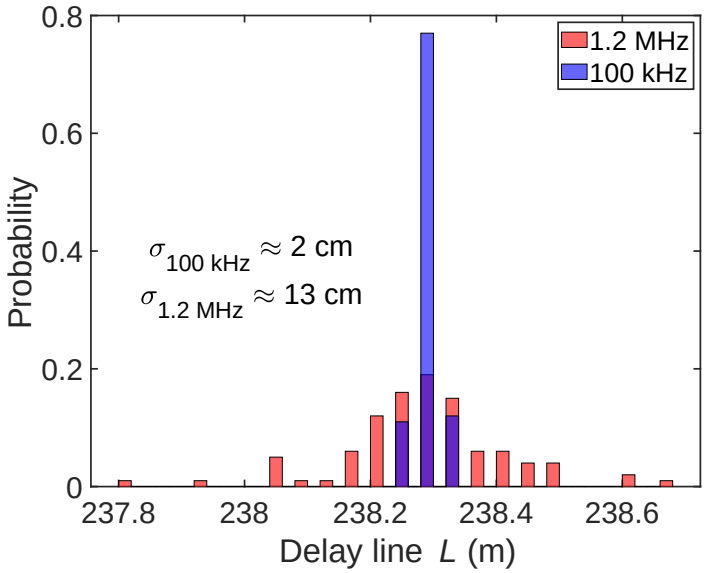

Figure 5.2: At a delay line $L = 238.28$ m, distributions of estimated distance over 100 traces with 1.2 MHz and 100 kHz laser sources.

the distribution of estimated distances over 100 measurements in the experiment. In the case of 1.2 MHz laser linewidth, the spectral broadening results in a variation of estimated distances from 237.8 m to 238.6 m, with a standard deviation $\sigma \approx$13 cm. For 100 kHz laser linewidth, the distance estimation is more certain, with 77% of measurements giving an estimated distance of 238.28 m, and the standard deviation is $\sim$2 cm.

Fig.5.3 compares the ranging precision with delay lines L varying from 43.68 m to 384.72 m when using 1.2 MHz and 100 kHz laser linewidth respectively. The top and bottom x-axes represent the delay lengths L normalised to the intrinsic laser coherence length L_{coh}. For the 100 kHz laser linewidth, all the delay lines used in the experiment were within the laser coherence length with maximum $\frac{L}{L_{coh}} \approx 0.6$. As the distance is increased, the ranging precision increases from 1 cm and plateaus at 2.5 cm. In the case of 1.2 MHz linewidth, at delay line $L = 43.68$ m, corresponding to $\frac{L}{L_{coh}} \approx 0.83$, the distance is approaching the laser coherence length, and $\sim$5 cm ranging precision is measured. Beyond the coherence length, the ranging precision starts to deteriorate rapidly. However, at $\frac{L}{L_{coh}} \approx 7$ (delay line $L = 384.72$ m), $\sim$15 cm ranging precision is still achievable.

5.2 Simulations of varying delay lines and laser linewidths

Simulations were performed next, investigating in detail how the ranging precision varies with laser linewidth and ranging distance. As with the simulation model presented in the previous Chapter, the laser phase noise was modeled as a Wiener process, with laser linewidth $\Delta\nu$ varying from 100 kHz up to 1.2 MHz. The SSMF delay lines L were varied from 10 m up to 490 m in simulations, limited by the discontinuity of the frequency chirp sawtooth waveform as previously discussed in Sec. 2.2.3. Monte Carlo simulations were carried out with 1000 measurements performed at each delay length and laser linewidth.

The ranging precision at varying delay lines and laser linewidths is shown in Fig.5.4. Good agreement between simulation and experimental results presented

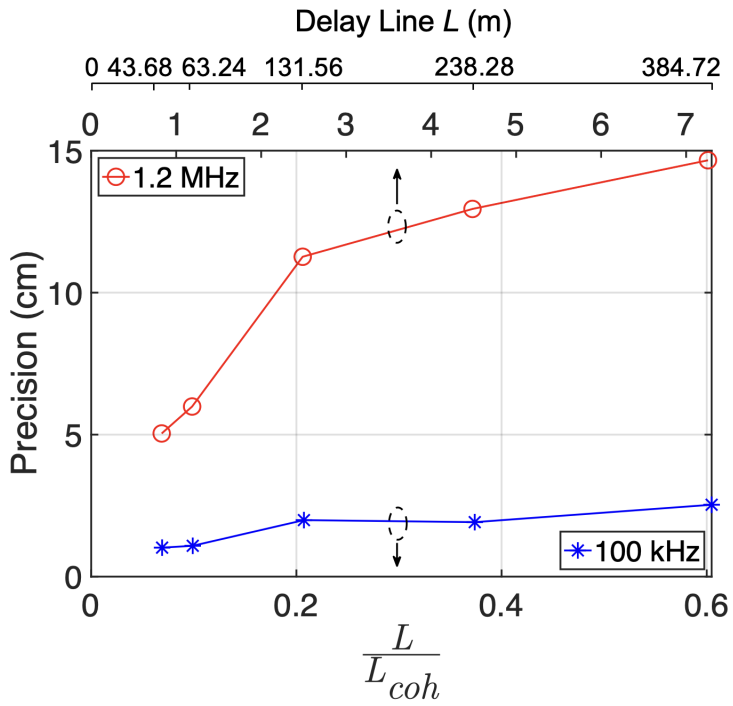

Figure 5.3: Ranging precision versus $\frac{L}{L_{coh}}$ with 1.2 MHz and 100 kHz laser source, for delay lines from 43.68 m to 384.72 m.

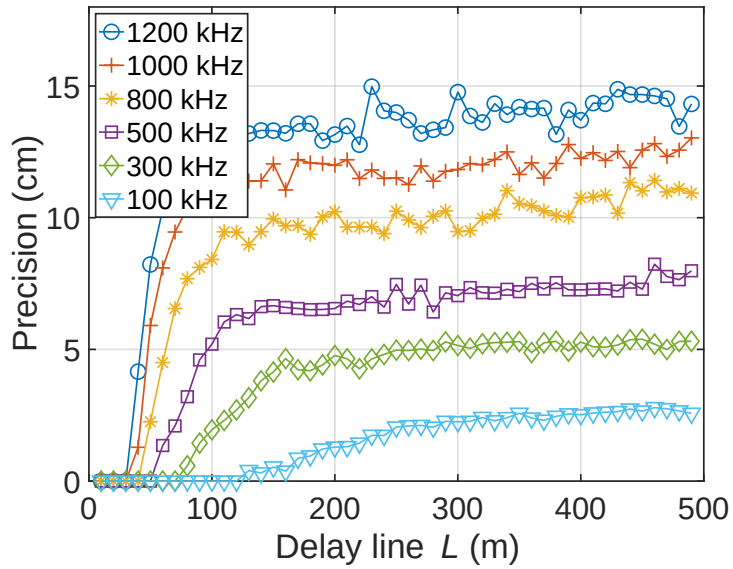

Figure 5.4: Numerical sweep of ranging precision with laser linewidth varying from 100 kHz to 1.2 MHz.

above was achieved. At delay distance L <120 m, the ranging precision could be sub-centimeter, while 1 cm precision is observed in the experiment in the case of 100 kHz laser source. This discrepancy might be due to additional noise and timing jitter in experiments. Increasing the delay length up to 490 m ($\frac{L}{L_{coh}} \approx 0.77$), a ranging precision of ∼2.5 cm is achievable for 100 kHz linewidth laser sources. For 300 kHz laser linewidth, $L_{coh} = 212.2$ m. With increased delay length, the ranging precision degrades from sub-centimeter and then plateaus at ∼5 cm in the incoherent regime. This was the case with the other laser linewidths; beyond the L_{coh}, the ranging precision plateaus at a certain level for each laser linewidth. In the case of 1.2 MHz laser source, with delay lines extending to 490 m which is 9× intrinsic laser coherence length, ∼15 cm ranging precision is still shown to be possible.

5.3 Summary

In this chapter, the impact of laser phase noise on the ranging precision of FMCW LiDAR systems when operating within and beyond the laser coherence length was assessed through both experiments and simulations. As expected, with increased laser linewidths and delay distances, the ranging precision deteriorates, especially in the incoherent measurement region. In the case of 1.2 MHz laser linewidth, it is shown that a ranging precision of ∼15 cm is still achievable at a distance of 384.72 m which is about 7× intrinsic laser coherence length. Provided that the ranging performance is acceptable, using a relatively high-linewidth laser for long-distance measurements might be considered for some cost-sensitive LiDAR applications.

Chapter 6

Conclusions and future work

The research work presented in this thesis focuses on the investigation of low-complexity digital signal processing (DSP) algorithm for short-reach optical fibre communication links, and the design of low-cost coherent light detection and ranging (LiDAR) systems. In this chapter, the key findings from this research work are summarised in Section 6.1. Suggestions for future work are given in Section 6.2.

6.1 Conclusions

For short-reach optical fibre links below $\leq$ 100 km, the system performance is largely limited by the static and time-varying linear distortions arising from the optical fibre: chromatic dispersion (CD), polarisation mode dispersion (PMD) and state of polarisation (SOP) rotations. The primary goals of implementing DSP algorithms at the receiver to mitigate these effects are cost-effectiveness and power-efficiency. Hence, the frequency-domain equalisation, taking advantage of the low computational complexity of the fast Fourier transform (FFT), is favourable. In this work, a novel low-complexity adaptive frequency-domain (FD) multiple-input multiple-output (MIMO) equaliser is studied. The proposed FD-MIMO equaliser combines static chromatic dispersion compensation (CDC) and adaptive equalisation for mitigating PMD and SOP rotations in one FFT block. This saves interim FFT/IFFT operations between individual DSP stages which can further reduce the calculation complexity. The main disadvantage

of adaptive frequency-domain equalisation is the feedback latency due to the presence of multiple FFTs/IFFTs and DSP operations in the feedback loop. This introduces delays in the adaptive filter coefficients update, and consequently degrades the equaliser's ability to track time-varying effects, especially during rapid SOP rotations. In order to improve the equaliser's robustness against feedback latency, a momentum-based gradient descent is applied to the adaptive FD-MIMO equaliser for the first time. Numerical assessment has demonstrated that the momentum-based gradient descent significantly outperforms the conventional gradient descent algorithm in the presence of adaptive filter update delays and dynamic channel variations. In transmission of a 92 Gbaud polarisation-division multiplexing (PDM) 64 QAM signal over 40 km standard single-mode fibre (SSMF), the momentum-based gradient descent was shown to be capable of tracking dynamic channels with up to 50 kHz SOP rotation frequency and mitigating penalties from feedback delays of up to 14 FFT blocks at the optical signal-to-noise ratio (OSNR) of 35 dB.

Apart from optical communications, optical sensing techniques, in particular, coherent LiDAR system with single-photodiode (PD) detection, are investigated in this thesis. Such a receiver architecture is low-cost and has low-complexity and hence is desirable for cost-sensitive LiDAR applications. The receiver sensitivity performance of two chirp signals, namely a single-sideband (SSB) frequency-modulated continuous-wave (FMCW) signal and a double-sideband (DSB) amplitude-modulated signal, was assessed using single PD-based coherent receivers. Both simulation and experimental results indicate that the SSB FMCW signal is a promising candidate for single-photodiode based coherent LiDAR system. It is immune to LO-LO beating interference (LO-LO BI) which is the dominant nonlinear distortion in such coherent receiver and which often requires a spectral guard band for mitigation. In addition, the SSB signal does not suffer from laser phase noise to amplitude noise conversion, hence offering a better receiver sensitivity compared to the DSB signal. In system tests with a delay line of 384.72 m, the SSB signal outperforms the DSB signal with a 10 dB better receiver

sensitivity in the case with a guard band for mitigating LO-LO BI, and 25 dB better sensitivity without a guard band. The drawback associated with SSB FMCW signal is the requirement of an in-phase and quadrature modulator (IQM) at the transmitter for the complex modulation while a Mach-Zehnder modulator (MZM) is sufficient for generating a real-valued DSB signal.

The transmitter laser linewidth is also an important parameter for FMCW LiDAR performance. For long-distance ranging of a few hundred meters, the use of low-linewidth lasers with increased laser coherence length is desirable at the expense of potentially high system cost. Although certain degradation in the ranging precision would be expected when operating in the incoherent regime, provided the performance is still acceptable, using a relatively high-linewidth laser might be considered for some cost-sensitive applications. Through both experiments and simulations, it was shown that for a 1.2 MHz linewidth laser, $\sim$15 cm ranging precision can still be achieved at a distance of 384.72 m which is about 7$\times$ the intrinsic laser coherence length.

6.2 Future work

6.2.1 Machine learning for mitigating time-varying effects in optical communication system

As mentioned in Chapter 1, applying machine learning (ML) techniques to optical communication systems has drawn a lot of research interests, in particular the deep learning (DL) technique [17, 29, 30, 187]. DL has demonstrated superior performance across a wide range of disciplines [188–190]. It utilises artificial neural networks to learn and extract high-level features from data. In the field of optical communication, DL has been applied in nonlinear transmission systems with the aim of reducing the computation complexity of conventional digital back propagation (DBP) algorithm which normally involves numerous alternating small steps to mitigate linear and nonlinear impairments from the fibre. This DL-based fibre nonlinearity mitigation technique is also referred to as learned DBP (LDBP) [31, 32, 187]. Deep learning has also been employed in optical

performance monitoring (OPM) where OSNR values, accumulated chromatic dispersion, differential group delay or even channel nonlinear effects can be identified by observing eye-diagram and eye-histogram parameters of the received signal [191, 192].

Though the DL-based algorithms seem to be promising for optimising and monitoring optical communication systems, their performance is highly dependent on the training process and the implementation of underlying neural networks. When encountering time-varying effects, such as PMD and SOP rotations as considered in the research work presented in this thesis, those dynamic effects might be hard to capture in the learning process and might ultimately lead to the failure of training [30]. One potential approach is to use a so-called recurrent neural network (RNN). RNN includes feedback connections that can allow information to be temporarily stored in the neural network. Therefore, it is usually applied to data with certain memories as is the case in a dynamic optical channel with PMD. Though the RNN has the ability to capture the time-varying effects, it might potentially lead to overkill and the poor performance on data it has not previously encountered. Hence, methods to design an appropriate RNN or in combination with other ML and DL approaches to mitigate time-varying distortions in optical communication systems are particularly interesting and worth investigating.

6.2.2 Comb-assisted FMCW LiDAR system

The optical frequency comb (OFC) has emerged as an alternative light source for LiDAR [193–196]. As its name suggests, the optical frequency comb consists of equally-spaced discrete lines in the frequency domain. In the time-of-flight (ToF) LiDAR systems, a few experiments proposed to use dual-frequency combs for absolute distance measurement [197, 198]. Since two combs are generated from the same seed laser, the optical phase is locked by default. Calculating the target distance against one of the dual combs enables a sub-nanometer-level precision. As for FMCW LiDAR, it was proposed to use a single reference interferometer to stitch together the comb lines at the receiver to increase the total signal duration when performing the Fourier transform. This leads to an improvement of

frequency-domain resolution, and hence the ranging resolution [35]. In addition, the OFC can be employed to accelerate the scanning speed when generating a 3D point cloud [199]. The technique involves using diffractive optics at the transmitter to spatially disperse all the comb lines to achieve massive parallel sensing and high-speed data acquisition. The proposed system can potentially replace conventionally-used laser arrays for simultaneously sweeping a wide range of view [82]. Besides, the eye safety issue is alleviated as the total emission power is dispersed across all the channels. Though these applications look very promising, each comb line is individually detected in such systems, requiring a wavelength demultiplexer, multiple PDs and ADCs, hence a rather complex system [35, 199]. Approaches to simplify such receiver architecture and reduce the system cost and complexity can be explored.

In addition to the coherent receiver which contributes to a large part of the system cost, the laser sources can be expensive, especially for high-coherence laser source as discussed previously in Sec. 2.2.3. In a comb-assisted LiDAR system, leveraging the fact that the laser phase noise is correlated among all the comb lines, potential techniques to reduce the phase noise penalty using the optical frequency comb would be interesting to investigate.

Acronyms

ADC analogue-to-digital converter

AMCW amplitude-modulated continuous-wave

APD single-photon avalanche detector

AR augmented reality

ASE amplified spontaneous emission

ASIC application-specific integrated circuit

AV autonomous vehicle

AWG arbitrary waveform generator

AWGN additive white Gaussian noise

BER bit error rate

BI beating interference

BPD balanced photodiode

CD chromatic dispersion

CDC chromatic dispersion compensation

CMA constant modulus algorithm

CMOS complementary metal-oxide semiconductor

CMRR common mode rejection ratio

CPE carrier phase estimation

CW continuous wave

DAC digital-to-analogue converter

DARPA Defense Advanced Research Projects Agency

DBP digital back propagation

DC direct current

DD direct detection

DD-LMS decision-directed least mean square

DFB distributed feedback

DGD differential group delay

DL deep learning

DML directly modulated laser

DP dual-polarisation

DSB double-sideband

DSP digital signal processing

ECL external cavity laser

EDFA Erbium-doped fibre amplifier

EOM electro-optic modulator

FD frequency-domain

FDE frequency-domain equaliser

FEC forward error correction

FFT fast Fourier transform

FIR finite impulse response

FMCW frequency-modulated continuous-wave

FOV field-of-view

FPGA field-programmable gate array

GMI generalised mutual information

GS geometric shaping

GVD group velocity dispersion

I in-phase

IFFT inverse fast Fourier transform

IM intensity modulation

IoT Internet of Things

IQM in-phase and quadrature modulator

ISI inter-symbol interference

KK Kramers-Kronig

LED light-emitting diode

LiDAR light detection and ranging

LMS least mean square

LO local oscillator

LO-LO BI local oscillator-local oscillator beating interference

MEMS micro-electromechanical system

MIMO multiple-input multiple-output

MIT Massachusetts Institute of Technology

ML machine learning

MSE mean squared error

MZM Mach-Zehnder modulator

OFC optical frequency comb

ONG Optical Networks Group

OPA optical phased array

OPM optical performance monitoring

OSA optical spectrum analyser

OSNR optical signal-to-noise ratio

PC polarisation controller

PD photodiode

PDM polarisation-division multiplexing

PLL phase-lock loop

PMD polarisation mode dispersion

PS probabilistic shaping

PSD power spectral density

PSK phase shift keying

Q quadrature

QAM quadrature amplitude modulation

QPSK quadrature phase shift keying

Radar radio detection and ranging

RC raised cosine

RDE radially-directed equaliser

RF radio frequency

RNN recurrent neural network

RRC root-raised cosine

Rx receiver

SDM space division multiplexing

SNR signal-to-noise ratio

SOP state of polarisation

SSB single-sideband

SSMF standard single-mode fibre

TD time-domain

TDE time-domain equaliser

TIA transimpedance amplifier

ToF time-of-flight

VCSEL vertical-cavity surface-emitting laser

VOA variable optical attenuator

VR virtual reality

WDM wavelength division multiplexing

Bibliography

[1] Cisco, "Cisco annual internet report (2018−2023) white paper," Cisco, Tech. Rep., March 2020.

[2] A. Feldmann, O. Gasser, F. Lichtblau, E. Pujol, I. Poese, C. Dietzel, D. Wagner, M. Wichtlhuber, J. Tapiador, N. Vallina-Rodriguez *et al.*, "Implications of the COVID-19 pandemic on the internet traffic," in *Broadband Coverage in Germany; 15th ITG-Symposium*. VDE, 2021, pp. 1–5.

[3] https://www.reuters.com/article/us-health-coronavirus-facebook-idUSKBN2190VH, [Online; accessed on 14-April-2022].

[4] https://www.forbes.com/sites/kristinstoller/2021/01/31/never-want-to-go-back-to-the-office-heres-where-you-should-work/?sh=e0e6b6167127, [Online; accessed on 14-April-2022].

[5] M. Speicher, B. D. Hall, and M. Nebeling, "What is mixed reality?" in *Proceedings of the 2019 CHI conference on human factors in computing systems*, 2019, pp. 1–15.

[6] L.-H. Lee, T. Braud, P. Zhou, L. Wang, D. Xu, Z. Lin, A. Kumar, C. Bermejo, and P. Hui, "All one needs to know about metaverse: A complete survey on technological singularity, virtual ecosystem, and research agenda," *arXiv preprint arXiv:2110.05352*, 2021.

[7] Y. Cai, J. Llorca, A. M. Tulino, and A. F. Molisch, "Compute-and data-intensive networks: The key to the metaverse," *arXiv preprint arXiv:2204.02001*, 2022.

[8] K. Kao and G. A. Hockham, "Dielectric-fibre surface waveguides for optical frequencies," *in Proceedings of the Institution of Electrical Engineers*, vol. 113, no. 7, pp. 1151–1158, 1966.

[9] T. Miya, Y. Terunuma, T. Hosaka, and T. Miyashita, "Ultimate low-loss single-mode fibre at 1.55 μm," *Electronics Letters*, vol. 15, no. 4, pp. 106–108, 1979.

[10] T. Okoshi, K. Emura, K. Kikuchi, and R. T. Kersten, "Computation of bit-error rate of various heterodyne and coherent-type optical communication schemes," *Journal of optical communications*, vol. 2, no. 3, pp. 89–96, 1981.

[11] T. Okoshi, "Recent advances in coherent optical fiber communication systems," *Journal of lightwave technology*, vol. 5, no. 1, pp. 44–52, 1987.

[12] R. J. Mears, L. Reekie, I. Jauncey, and D. N. Payne, "Low-noise erbium-doped fibre amplifier operating at 1.54 μm," *Electronics Letters*, vol. 23, no. 19, pp. 1026–1028, 1987.

[13] B. Mukherjee, "WDM optical communication networks: progress and challenges," *IEEE Journal on Selected Areas in communications*, vol. 18, no. 10, pp. 1810–1824, 2000.

[14] K. Kikuchi, "Fundamentals of coherent optical fiber communications," *Journal of Lightwave Technology*, vol. 34, no. 1, pp. 157–179, 2015.

[15] C. Laperle and M. O'Sullivan, "Advances in high-speed DACs, ADCs, and DSP for optical coherent transceivers," *Journal of lightwave technology*, vol. 32, no. 4, pp. 629–643, 2014.

[16] A. Alvarado, E. Agrell, D. Lavery, R. Maher, and P. Bayvel, "Replacing the soft-decision FEC limit paradigm in the design of optical communication

systems," *Journal of Lightwave Technology*, vol. 33, no. 20, pp. 4338–4352, 2015.

[17] B. Karanov, M. Chagnon, F. Thouin, T. A. Eriksson, H. Bülow, D. Lavery, P. Bayvel, and L. Schmalen, "End-to-end deep learning of optical fiber communications," *Journal of Lightwave Technology*, vol. 36, no. 20, pp. 4843–4855, 2018.

[18] E. Sillekens, D. Semrau, D. Lavery, P. Bayvel, and R. Killey, "Experimental demonstration of geometrically-shaped constellations tailored to the nonlinear fibre channel," in *2018 European Conference on Optical Communication (ECOC)*, 2018, pp. 1–3.

[19] J. Cho and P. J. Winzer, "Probabilistic constellation shaping for optical fiber communications," *Journal of Lightwave Technology*, vol. 37, no. 6, pp. 1590–1607, 2019.

[20] T. Hoshida, V. Curri, L. Galdino, D. T. Neilson, W. Forysiak, J. K. Fischer, T. Kato, and P. Poggiolini, "Ultrawideband systems and networks: Beyond C + L-band," *Proceedings of the IEEE*, vol. 110, no. 11, pp. 1725–1741, 2022.

[21] B. J. Puttnam, R. S. Luís, G. Rademacher, M. Mendez-Astudilio, Y. Awaji, and H. Furukawa, "S, C and extended L-band transmission with doped fiber and distributed raman amplification," in *2021 Optical Fiber Communications Conference and Exhibition (OFC)*. IEEE, 2021, p. Th4C.2.

[22] L. Galdino, A. Edwards, W. Yi, E. Sillekens, Y. Wakayama, T. Gerard, W. S. Pelouch, S. Barnes, T. Tsuritani, R. I. Killey, D. Lavery, and P. Bayvel, "Optical fibre capacity optimisation via continuous bandwidth amplification and geometric shaping," *IEEE Photonics Technology Letters*, vol. 32, no. 17, pp. 1021–1024, 2020.

[23] A. Napoli, N. Calabretta, J. K. Fischer, N. Costa, S. Abrate, J. Pedro, V. Lopez, V. Curri, D. Zibar, E. Pincemin *et al.*, "Perspectives of

multi-band optical communication systems," in *2018 23rd Opto-Electronics and Communications Conference (OECC)*. IEEE, 2018, pp. 5B3–1.

[24] P. Hazarika, M. Tan, A. Donodin, S. Noor, I. Phillips, P. Harper, J. S. Stone, M. J. Li, and W. Forysiak, "E-, S-, C-and L-band coherent transmission with a multistage discrete raman amplifier," *Optics Express*, vol. 30, no. 24, pp. 43 118–43 126, 2022.

[25] B. J. Puttnam, R. S. Luís, G. Rademacher, Y. Awaji, and H. Furukawa, "319 Tb/s transmission over 3001 km with S, C and L band signals over >120nm bandwidth in 125 μm wide 4-core fiber," in *Optical Fiber Communication Conference (OFC) 2021*. Optica Publishing Group, 2021, p. F3B.3.

[26] R. Emmerich, M. Sena, R. Elschner, C. Schmidt-Langhorst, I. Sackey, C. Schubert, and R. Freund, "Enabling SCL-band systems with standard C-band modulator and coherent receiver using coherent system identification and nonlinear predistortion," *Journal of Lightwave Technology*, vol. 40, no. 5, pp. 1360–1368, 2022.

[27] K. Saitoh and S. Matsuo, "Multicore fiber technology," *Journal of Lightwave Technology*, vol. 34, no. 1, pp. 55–66, 2016.

[28] B. J. Puttnam, G. Rademacher, and R. S. Luís, "Space-division multiplexing for optical fiber communications," *Optica*, vol. 8, no. 9, pp. 1186–1203, 2021.

[29] D. Zibar, M. Piels, R. Jones, and C. G. Schäeffer, "Machine learning techniques in optical communication," *Journal of Lightwave Technology*, vol. 34, no. 6, pp. 1442–1452, 2015.

[30] F. N. Khan, Q. Fan, C. Lu, and A. P. T. Lau, "An optical communication's perspective on machine learning and its applications," *Journal of Lightwave Technology*, vol. 37, no. 2, pp. 493–516, 2019.

[31] E. Sillekens, W. Yi, D. Semrau, A. Ottino, B. Karanov, D. Lavery, L. Galdino, P. Bayvel, R. I. Killey, S. Zhou, K. Law, and J. Chen, "Time-domain learned digital back-propagation," in *2020 IEEE Workshop on Signal Processing Systems (SiPS)*, 2020, pp. 1–4.

[32] C. Häger and H. D. Pfister, "Deep learning of the nonlinear schrödinger equation in fiber-optic communications," in *2018 IEEE International Symposium on Information Theory (ISIT)*. IEEE, 2018, pp. 1590–1594.

[33] O. Shental and J. Hoydis, "Machine LLRning: Learning to softly demodulate," in *2019 IEEE Globecom Workshops (GC Wkshps)*. IEEE, 2019, pp. 1–7.

[34] B. La Lone, B. Marshall, E. Miller, G. Stevens, W. Turley, and L. Veeser, "Simultaneous broadband laser ranging and photonic doppler velocimetry for dynamic compression experiments," *Review of Scientific Instruments*, vol. 86, no. 2, p. 023112, 2015.

[35] N. Kuse and M. E. Fermann, "Frequency-modulated comb LIDAR," *Apl Photonics*, vol. 4, no. 10, p. 106105, 2019.

[36] K. Chen, H. Zhang, Z. Xu, and S. Pan, "FMCW lidar with communication capability using phase-diversity coherent detection," in *2019 24th OptoElectronics and Communications Conference (OECC) and 2019 International Conference on Photonics in Switching and Computing (PSC)*. IEEE, 2019, pp. 1–3.

[37] A. Villringer and B. Chance, "Non-invasive optical spectroscopy and imaging of human brain function," *Trends in neurosciences*, vol. 20, no. 10, pp. 435–442, 1997.

[38] C. B. Carlisle, J. E. van der Laan, L. W. Carr, P. Adam, and J.-P. Chiaroni, "CO2 laser-based differential absorption lidar system for range-resolved and long-range detection of chemical vapor plumes," *Applied optics*, vol. 34, no. 27, pp. 6187–6200, 1995.

[39] A. B. Gschwendtner and W. E. Keicher, "Development of coherent laser radar at Lincoln laboratory," *Lincoln Laboratory Journal*, vol. 12, no. 2, pp. 383–396, 2000.

[40] C. F. Abari, A. T. Pedersen, and J. Mann, "An all-fiber image-reject homodyne coherent doppler wind lidar," *Optics express*, vol. 22, no. 21, pp. 25 880–25 894, 2014.

[41] P. Feneyrou, L. Leviandier, J. Minet, G. Pillet, A. Martin, D. Dolfi, J.-P. Schlotterbeck, P. Rondeau, X. Lacondemine, A. Rieu, and T. Midavaine, "Frequency-modulated multifunction lidar for anemometry, range finding, and velocimetry–1. theory and signal processing," *Applied optics*, vol. 56, no. 35, pp. 9663–9675, 2017.

[42] R. Roriz, J. Cabral, and T. Gomes, "Automotive lidar technology: A survey," *IEEE Transactions on Intelligent Transportation Systems*, 2021.

[43] https://en.wikipedia.org/wiki/Stanley_(vehicle), [Online; accessed on 21-June-2022].

[44] C. Rablau, "Lidar–a new (self-driving) vehicle for introducing optics to broader engineering and non-engineering audiences," in *Education and Training in Optics and Photonics*. Optica Publishing Group, 2019, p. 11143_138.

[45] B. Behroozpour, P. A. Sandborn, M. C. Wu, and B. E. Boser, "Lidar system architectures and circuits," *IEEE Communications Magazine*, vol. 55, no. 10, pp. 135–142, 2017.

[46] S. Royo and M. Ballesta-Garcia, "An overview of lidar imaging systems for autonomous vehicles," *Applied Sciences*, vol. 9, no. 19, p. 4093, 2019.

[47] M. E. Warren, "Automotive lidar technology," in *2019 Symposium on VLSI Circuits*. IEEE, 2019, pp. C254–C255.

[48] T. Kim, "Realization of integrated coherent lidar," Ph.D. dissertation, UC Berkeley, 2019.

[49] K. Zhong, X. Zhou, J. Huo, C. Yu, C. Lu, and A. P. T. Lau, "Digital signal processing for short-reach optical communications: A review of current technologies and future trends," *Journal of Lightwave Technology*, vol. 36, no. 2, pp. 377–400, 2018.

[50] J. C. Geyer, C. R. S. Fludger, T. Duthel, C. Schuhen, and B. Schmauss, "Efficient frequency domain chromatic dispersion compensation in a coherent Polmux QPSK-receiver," *in 2010 Conference on Optical Fiber Communication/National Fiber Optic Engineers Conference*, pp. 1–3, 2010.

[51] B. Farhang-Boroujeny, *Adaptive filters: theory and applications*. John Wiley & Sons, 2013.

[52] D. Lavery, B. C. Thomsen, P. Bayvel, and S. J. Savory, "Reduced complexity equalization for coherent long-reach passive optical networks [invited]," *IEEE/OSA Journal of Optical Communications and Networking*, vol. 7, no. 1, pp. A16–A27, Jan 2015.

[53] S. J. Savory, "Digital filters for coherent optical receivers," *Optics express*, vol. 16, no. 2, pp. 804–817, 2008.

[54] I. Fatadin, D. Ives, and S. J. Savory, "Blind equalization and carrier phase recovery in a 16-QAM optical coherent system," *Journal of Lightwave Technology*, vol. 27, no. 15, pp. 3042–3049, Aug 2009.

[55] E. M. Ip and J. M. Kahn, "Fiber impairment compensation using coherent detection and digital signal processing," *Journal of Lightwave Technology*, vol. 28, no. 4, pp. 502–519, 2009.

[56] S. J. Savory, "Digital coherent optical receivers: Algorithms and subsystems," *IEEE Journal of Selected Topics in Quantum Electronics*, vol. 16, no. 5, pp. 1164–1179, 2010.

[57] A. P. T. Lau, Y. Gao, Q. Sui, D. Wang, Q. Zhuge, M. H. Morsy-Osman, M. Chagnon, X. Xu, C. Lu, and D. V. Plant, "Advanced DSP techniques enabling high spectral efficiency and flexible transmissions: Toward elastic optical networks," *IEEE Signal Processing Magazine*, vol. 31, no. 2, pp. 82–92, 2014.

[58] H. Sun, M. Torbatian, M. Karimi, R. Maher, S. Thomson, M. Tehrani, Y. Gao, A. Kumpera, G. Soliman, A. Kakkar, M. Osman, Z. A. El-Sahn, C. Doggart, W. Hou, S. Sutarwala, Y. Wu, M. R. Chitgarha, V. Lal, H.-S. Tsai, S. Corzine, J. Zhang, J. Osenbach, S. Buggaveeti, Z. Morbi, M. I. Olmedo, I. Leung, X. Xu, P. Samra, V. Dominic, S. Sanders, M. Ziari, A. Napoli, B. Spinnler, K.-T. Wu, and P. Kandappan, "800g DSP ASIC design using probabilistic shaping and digital sub-carrier multiplexing," *Journal of Lightwave Technology*, vol. 38, no. 17, pp. 4744–4756, 2020.

[59] C. Fougstedt, P. Johannisson, L. Svensson, and P. Larsson-Edefors, "Dynamic equalizer power dissipation optimization," in *Optical Fiber Communication Conference*, 2016, p. W4A.2.

[60] M. S. Faruk and K. Kikuchi, "Adaptive frequency-domain equalization in digital coherent optical receivers," *Optics Express*, vol. 19, no. 13, pp. 12 789–12 798, 2011.

[61] K. Ishihara, T. Kobayashi, R. Kudo, Y. Takatori, A. Sano, E. Yamada, H. Masuda, and Y. Miyamoto, "Coherent optical transmission with frequency-domain equalization," in *2008 34th European Conference on Optical Communication*. IEEE, 2008, pp. 1–2.

[62] F. N. Hauske, C. Xie, Z. Zhang, C. Li, L. Li, and Q. Xiong, "Frequency domain chromatic dispersion estimation," in *2010 Conference on Optical Fiber Communication (OFC/NFOEC), collocated National Fiber Optic Engineers Conference*. IEEE, 2010, pp. 1–3.

[63] J. J. Shynk, "Frequency-domain and multirate adaptive filtering," *IEEE Signal Processing Magazine*, vol. 9, no. 1, pp. 14–37, Jan 1992.

[64] J. S. Bruno, V. Almenar, and J. Valls, "FPGA implementation of a 10 GS/s variable-length FFT for OFDM-based optical communication systems," *Microprocessors and Microsystems*, vol. 64, pp. 195–204, 2019.

[65] T. Zeng, Z. He, L. Meng, F. Jiang, J. Li, and X. Li, "The training based feed-forward 2× 2 MIMO algorithm and its real time implementation," *in European Conference on Optical Communication*, pp. 1–4, 2019.

[66] M. Mahdavi, O. Edfors, V. Öwall, and L. Liu, "A low latency fft/ifft architecture for massive mimo systems utilizing ofdm guard bands," *IEEE Transactions on Circuits and Systems I: Regular Papers*, vol. 66, no. 7, pp. 2763–2774, 2019.

[67] F. Pittalà, C. Stone, D. Clark, M. Kuschnerov, C. Xie, and A. Haddad, "Laboratory measurements of SOP transients due to lightning strikes on OPGW cables," in *Optical Fiber Communication Conference*. Optical Society of America, 2018, pp. M4B–5.

[68] D. Charlton, S. Clarke, D. Doucet, M. O'Sullivan, D. L. Peterson, D. Wilson, G. Wellbrock, and M. Bélanger, "Field measurements of SOP transients in OPGW, with time and location correlation to lightning strikes," *Optics Express*, vol. 25, no. 9, pp. 9689–9696, 2017.

[69] P. M. Krummrich, D. Ronnenberg, W. Schairer, D. Wienold, F. Jenau, and M. Herrmann, "Demanding response time requirements on coherent receivers due to fast polarization rotations caused by lightning events," *Optics express*, vol. 24, no. 11, pp. 12 442–12 457, 2016.

[70] K. Sayyah, R. Sarkissian, P. Patterson, B. Huang, O. Efimov, D. Kim, K. Elliott, L. Yang, and D. Hammon, "Fully integrated FMCW LiDAR optical engine on a single silicon chip," *Journal of Lightwave Technology*, vol. 40, no. 9, pp. 2763–2772, 2022.

[71] S. Kakuma, "Frequency-modulated continuous-wave laser radar using dual vertical-cavity surface-emitting laser diodes for real-time measurements of distance and radial velocity," *Optical Review*, vol. 24, no. 1, pp. 39–46, 2017.

[72] C. J. Karlsson, F. Å. Olsson, D. Letalick, and M. Harris, "All-fiber multifunction continuous-wave coherent laser radar at 1.55 μm for range, speed, vibration, and wind measurements," *Applied optics*, vol. 39, no. 21, pp. 3716–3726, 2000.

[73] T. DiLazaro and G. Nehmetallah, "Multi-terahertz frequency sweeps for high-resolution, frequency-modulated continuous wave ladar using a distributed feedback laser array," *Optics express*, vol. 25, no. 3, pp. 2327–2340, 2017.

[74] T. Hariyama, P. A. Sandborn, M. Watanabe, and M. C. Wu, "High-accuracy range-sensing system based on FMCW using low-cost VCSEL," *Optics express*, vol. 26, no. 7, pp. 9285–9297, 2018.

[75] T. Kim, P. Bhargava, and V. Stojanović, "Overcoming the coherence distance barrier in long-range FMCW LiDAR," *2018 Conference on Lasers and Electro-Optics (CLEO)*, p. STh3L.7, 2018.

[76] X. Zhang, J. Pouls, and M. C. Wu, "Laser frequency sweep linearization by iterative learning pre-distortion for FMCW LiDAR," *Optics express*, vol. 27, no. 7, pp. 9965–9974, 2019.

[77] M.-C. Amann, T. M. Bosch, M. Lescure, R. Myllylä, and M. Rioux, "Laser ranging: a critical review of unusual techniques for distance measurement," *Optical engineering*, vol. 40, no. 1, pp. 10–19, 2001.

[78] N. Satyan, A. Vasilyev, G. Rakuljic, V. Leyva, and A. Yariv, "Precise control of broadband frequency chirps using optoelectronic feedback," *Optics express*, vol. 17, no. 18, pp. 15 991–15 999, 2009.

[79] P. Adany, C. Allen, and R. Hui, "Chirped lidar using simplified homodyne detection," *Journal of lightwave technology*, vol. 27, no. 16, pp. 3351–3357, 2009.

[80] Z. Xu, H. Zhang, K. Chen, D. Zhu, and S. Pan, "FMCW lidar using phase-diversity coherent detection to avoid signal aliasing," *IEEE Photonics Technology Letters*, vol. 31, no. 22, pp. 1822–1825, 2019.

[81] S. Gao, M. O'Sullivan, and R. Hui, "Complex-optical-field lidar system for range and vector velocity measurement," *Optics express*, vol. 20, no. 23, pp. 25 867–25 875, 2012.

[82] A. Martin, D. Dodane, L. Leviandier, D. Dolfi, A. Naughton, P. O'Brien, T. Spuessens, R. Baets, G. Lepage, P. Verheyen, P. De Heyn, P. Absil, P. Feneyrou, and J. Bourderionnet, "Photonic integrated circuit-based FMCW coherent LiDAR," *Journal of Lightwave Technology*, vol. 36, no. 19, pp. 4640–4645, 2018.

[83] Y. Furukado, H. Abe, Y. Hinakura, and T. Baba, "Experimental simulation of ranging action using Si photonic crystal modulator and optical antenna," *Optics Express*, vol. 26, no. 14, pp. 18 222–18 229, 2018.

[84] C. V. Poulton, A. Yaacobi, D. B. Cole, M. J. Byrd, M. Raval, D. Vermeulen, and M. R. Watts, "Coherent solid-state LIDAR with silicon photonic optical phased arrays," *Optics letters*, vol. 42, no. 20, pp. 4091–4094, 2017.

[85] C. V. Poulton, M. J. Byrd, P. Russo, E. Timurdogan, M. Khandaker, D. Vermeulen, and M. R. Watts, "Long-range lidar and free-space data communication with high-performance optical phased arrays," *IEEE Journal of Selected Topics in Quantum Electronics*, vol. 25, no. 5, pp. 1–8, 2019.

[86] T. Kim, P. Bhargava, C. V. Poulton, J. Notaros, A. Yaacobi, E. Timurdogan, C. Baiocco, N. Fahrenkopf, S. Kruger, T. Ngai *et al.*, "A single-chip optical phased array in a wafer-scale silicon photonics/CMOS 3D-integration

platform," *IEEE Journal of Solid-State Circuits*, vol. 54, no. 11, pp. 3061–3074, 2019.

[87] J. Doylend and S. Gupta, "An overview of silicon photonics for lidar," *Silicon Photonics XV*, vol. 11285, pp. 109–115, 2020.

[88] G. P. Agrawal, "Nonlinear fiber optics," in *Nonlinear Science at the Dawn of the 21st Century*. Springer, 2000, pp. 195–211.

[89] https://www.corning.com/media/worldwide/coc/documents/Fiber/product-information-sheets/PI1463_07-14_English.pdf, [Online; accessed on 20-May-2021].

[90] http://www.tlc.unipr.it/cucinotta/cfa/datasheet_SMF28e.pdf, [Online; accessed on 20-May-2021].

[91] M. S. Faruk and S. J. Savory, "Digital signal processing for coherent transceivers employing multilevel formats," *Journal of Lightwave Technology*, vol. 35, no. 5, pp. 1125–1141, 2017.

[92] M. Kuschnerov, F. N. Hauske, K. Piyawanno, B. Spinnler, A. Napoli, and B. Lankl, "Adaptive chromatic dispersion equalization for non-dispersion managed coherent systems," *in 2009 Conference on Optical Fiber Communication*, pp. 1–3, 2009.

[93] J. Leibrich and W. Rosenkranz, "Frequency domain equalization with minimum complexity in coherent optical transmission systems," in *Optical Fiber Communication Conference*, 2010, p. OWV1.

[94] A. Eghbali, H. Johansson, O. Gustafsson, and S. J. Savory, "Optimal least-squares FIR digital filters for compensation of chromatic dispersion in digital coherent optical receivers," *Journal of Lightwave Technology*, vol. 32, no. 8, pp. 1449–1456, 2014.

[95] S. S. Haykin, *Adaptive filter theory*. Pearson Education India, 2008.

[96] T. Xu, G. Jacobsen, S. Popov, M. Forzati, J. Mårtensson, M. Mussolin, J. Li, K. Wang, Y. Zhang, and A. T. Friberg, "Frequency-domain chromatic dispersion equalization using overlap-add methods in coherent optical system," *Journal of optical communications*, vol. 32, no. 2, pp. 131–135, 2011.

[97] R. Kudo, T. Kobayashi, K. Ishihara, Y. Takatori, A. Sano, and Y. Miyamoto, "Coherent optical single carrier transmission using overlap frequency domain equalization for long-haul optical systems," *Journal of Lightwave Technology*, vol. 27, no. 16, pp. 3721–3728, Aug 2009.

[98] T. Xu, G. Jacobsen, S. Popov, J. Li, E. Vanin, K. Wang, A. T. Friberg, and Y. Zhang, "Chromatic dispersion compensation in coherent transmission system using digital filters," *Optics express*, vol. 18, no. 15, pp. 16 243–16 257, 2010.

[99] B. Spinnler, "Complexity of algorithms for digital coherent receivers," in *2009 35th European Conference on Optical Communication*. IEEE, 2009, pp. 1–4.

[100] R. Corsini, A. Peracchi, E. Matarazzo, T. Foggi, J. Nijhof, G. Meloni, L. Potì, R. Magri, and E. Ciaramella, "Blind adaptive chromatic dispersion compensation and estimation for DSP-based coherent optical systems," *Journal of Lightwave Technology*, vol. 31, no. 13, pp. 2131–2139, 2013.

[101] D. Penninckx and V. Morenas, "Jones matrix of polarization mode dispersion," *Optics Letter*, vol. 24, no. 13, pp. 875–877, 1999.

[102] J. Lee and Y. C. Chung, "Statistical PMD emulator using variable DGD elements," in *Optical Fiber Communication Conference and Exhibit*. IEEE, 2002, pp. 375–376.

[103] S. Desbruslais and P. Morkel, "Simulation of polarisation mode dispersion and its effects in long-haul optically amplified lightwave systems," in *IEE Colloquium on International Transmission System*. IET, 1994, pp. 6–1.

[104] J. Treichler and B. Agee, "A new approach to multipath correction of constant modulus signals," *in IEEE Transactions on Acoustics, Speech, and Signal Processing*, vol. 31, no. 2, pp. 459–472, 1983.

[105] D. Godard, "Self-recovering equalization and carrier tracking in two-dimensional data communication systems," *IEEE transactions on communications*, vol. 28, no. 11, pp. 1867–1875, 1980.

[106] M. J. Ready and R. P. Gooch, "Blind equalization based on radius directed adaptation," *in International Conference on Acoustics, Speech, and Signal Processing*, pp. 1699–1702 vol.3, 1990.

[107] Y. Wakayama, E. Sillekens, L.Galdino, D. Lavery, R. I. Killey, and P. Bayvel, "Increasing achievable information rates with pilot-based DSP in standard intradyne detection," in *European Conference on Optical Communication*, 2019, p. W.1.B.5.

[108] L. Liu, Z. Tao, W. Yan, S. Oda, T. Hoshida, and J. C. Rasmussen, "Initial tap setup of constant modulus algorithm for polarization de-multiplexing in optical coherent receivers," in *2009 Conference on Optical Fiber Communication*. IEEE, 2009, p. OMT2.

[109] D. Mansour and A. Gray, "Unconstrained frequency-domain adaptive filter," *IEEE Transactions on Acoustics, Speech, and Signal Processing*, vol. 30, no. 5, pp. 726–734, 1982.

[110] M. S. Faruk, "Unconstraint adaptive frequency-domain equalizer for coherent optical receivers," in *8th International Conference on Electrical and Computer Engineering*, 2014, pp. 40–42.

[111] https://www.lightwaveonline.com/network-design/high-speed-networks/article/16654079/lightning-affects-coherent-optical-transmission-in-aerial-fiber, [Online; accessed on 26-April-2022].

[112] M. Morsy-Osman, M. Chagnon, Q. Zhuge, X. Xu, M. E. Mousa-Pasandi, Z. A. El-Sahn, and D. V. Plant, "Ultrafast and low overhead training symbol based channel estimation in coherent M-QAM single-carrier transmission systems," *Optics express*, vol. 20, no. 26, pp. B171–B180, 2012.

[113] J. Yang, E. Sillekens, W. Yi, P. Bayvel, and R. I. Killey, "Joint estimation of dynamic polarization and carrier phase with pilot-based adaptive equalizer in PDM-64QAM transmission system," *Optics Express*, vol. 29, no. 26, pp. 43 136–43 147, 2021.

[114] Y. Li and J. Ibanez-Guzman, "Lidar for autonomous driving: The principles, challenges, and trends for automotive lidar and perception systems," *IEEE Signal Processing Magazine*, vol. 37, no. 4, pp. 50–61, 2020.

[115] M. A. Albota, B. F. Aull, D. G. Fouche, R. M. Heinrichs, D. G. Kocher, R. M. Marino, J. G. Mooney, N. R. Newbury, M. E. O'Brien, B. E. Player *et al.*, "Three-dimensional imaging laser radars with Geiger-mode avalanche photodiode arrays," *Lincoln Laboratory Journal*, vol. 13, no. 2, pp. 351–370, 2002.

[116] R. K. Ula, Y. Noguchi, and K. Iiyama, "Three-dimensional object profiling using highly accurate FMCW optical ranging system," *Journal of Lightwave Technology*, vol. 37, no. 15, pp. 3826–3833, 2019.

[117] D. Resler, D. Hobbs, R. Sharp, L. Friedman, and T. Dorschner, "High-efficiency liquid-crystal optical phased-array beam steering," *Optics letters*, vol. 21, no. 9, pp. 689–691, 1996.

[118] B.-W. Yoo, M. Megens, T. Sun, W. Yang, C. J. Chang-Hasnain, D. A. Horsley, and M. C. Wu, "A 32$\times$ 32 optical phased array using polysilicon sub-wavelength high-contrast-grating mirrors," *Optics express*, vol. 22, no. 16, pp. 19 029–19 039, 2014.

[119] H. W. Yoo, N. Druml, D. Brunner, C. Schwarzl, T. Thurner, M. Hennecke, and G. Schitter, "MEMS-based lidar for autonomous driving," *e & i Elektrotechnik und Informationstechnik*, vol. 135, no. 6, pp. 408–415, 2018.

[120] S. T. Holmström, U. Baran, and H. Urey, "MEMS laser scanners: a review," *Journal of Microelectromechanical Systems*, vol. 23, no. 2, pp. 259–275, 2014.

[121] J. Liu, Q. Sun, Z. Fan, and Y. Jia, "TOF lidar development in autonomous vehicle," in *2018 IEEE 3rd Optoelectronics Global Conference (OGC)*. IEEE, 2018, pp. 185–190.

[122] R. Horaud, M. Hansard, G. Evangelidis, and C. Ménier, "An overview of depth cameras and range scanners based on time-of-flight technologies," *Machine vision and applications*, vol. 27, no. 7, pp. 1005–1020, 2016.

[123] A. Kolb, E. Barth, R. Koch, and R. Larsen, "Time-of-flight cameras in computer graphics," in *Computer Graphics Forum*, vol. 29, no. 1. Wiley Online Library, 2010, pp. 141–159.

[124] S. Foix, G. Alenya, and C. Torras, "Lock-in time-of-flight (ToF) cameras: A survey," *IEEE Sensors Journal*, vol. 11, no. 9, pp. 1917–1926, 2011.

[125] W. C. Partners and Y. Développement, "Automotive lidar market report," OIDA Publications & Reports; Optical Society of America: Washington, DC, USA, Tech. Rep., 2018.

[126] J. Illade-Quinteiro, V. M. Brea, P. López, D. Cabello, and G. Doménech-Asensi, "Distance measurement error in time-of-flight sensors due to shot noise," *Sensors*, vol. 15, no. 3, pp. 4624–4642, 2015.

[127] R. Agishev, B. Gross, F. Moshary, A. Gilerson, and S. Ahmed, "Range-resolved pulsed and CWFM lidars: potential capabilities comparison," *Applied Physics B*, vol. 85, no. 1, pp. 149–162, 2006.

[128] D. J. Lum, S. H. Knarr, and J. C. Howell, "Frequency-modulated continuous-wave LiDAR compressive depth-mapping," *Optics express*, vol. 26, no. 12, pp. 15 420–15 435, 2018.

[129] M. U. Piracha, D. Nguyen, D. Mandridis, T. Yilmaz, I. Ozdur, S. Ozharar, and P. J. Delfyett, "Range resolved lidar for long distance ranging with sub-millimeter resolution," *Optics express*, vol. 18, no. 7, pp. 7184–7189, 2010.

[130] G. M. Williams, "Optimization of eyesafe avalanche photodiode lidar for automobile safety and autonomous navigation systems," *Optical Engineering*, vol. 56, no. 3, p. 031224, 2017.

[131] https://cdn.sparkfun.com/datasheets/Sensors/Proximity/LIDAR-Lite-Data-Sheet.pdf, [Online; accessed on 21-June-2022].

[132] https://static.rapidonline.com/pdf/75-0724_v1.pdf, [Online; accessed on 21-June-2022].

[133] https://www.lidarsensor.nl/wp-content/uploads/2020/11/LiDAR-Sensor-datasheet-SF23-ENG.pdf, [Online; accessed on 21-June-2022].

[134] Z. Liu, J. F. Barlow, P.-W. Chan, J. C. H. Fung, Y. Li, C. Ren, H. W. L. Mak, and E. Ng, "A review of progress and applications of pulsed doppler wind LiDARs," *remote sensing*, vol. 11, no. 21, p. 2522, 2019.

[135] P. Lindelöw *et al.*, *Fiber based coherent lidars for remote wind sensing*. Ørsted. DTU, Technical University of Denmark, 2007.

[136] H. Sarbolandi, D. Lefloch, and A. Kolb, "Kinect range sensing: Structured-light versus time-of-flight kinect," *Computer vision and image understanding*, vol. 139, pp. 1–20, 2015.

[137] https://www.allaboutcircuits.com/technical-articles/how-do-time-of-flight-sensors-work-pmdtechnologies-tof-3D-camera/, [Online; accessed on 21-June-2022].

[138] S. Gokturk, H. Yalcin, and C. Bamji, "A time-of-flight depth sensor - system description, issues and solutions," in *2004 Conference on Computer Vision and Pattern Recognition Workshop*, 2004, pp. 35–35.

[139] R. Whyte, L. Streeter, M. J. Cree, and A. A. Dorrington, "Application of lidar techniques to time-of-flight range imaging," *Applied optics*, vol. 54, no. 33, pp. 9654–9664, 2015.

[140] R. Lange and P. Seitz, "Solid-state time-of-flight range camera," *IEEE Journal of quantum electronics*, vol. 37, no. 3, pp. 390–397, 2001.

[141] https://www.cvl.isy.liu.se/education/undergraduate/tsbb09/lasmaterial/SR3000_Flyer_Jan07.pdf, [Online; accessed on 21-June-2022].

[142] C. S. Bamji, P. O'Connor, T. Elkhatib, S. Mehta, B. Thompson, L. A. Prather, D. Snow, O. C. Akkaya, A. Daniel, A. D. Payne *et al.*, "A 0.13 μm CMOS system-on-chip for a 512$\times$ 424 time-of-flight image sensor with multi-frequency photo-demodulation up to 130 MHz and 2 Gs/s ADC," *IEEE Journal of Solid-State Circuits*, vol. 50, no. 1, pp. 303–319, 2014.

[143] S. Kawahito, I. A. Halin, T. Ushinaga, T. Sawada, M. Homma, and Y. Maeda, "A CMOS time-of-flight range image sensor with gates-on-field-oxide structure," *IEEE Sensors Journal*, vol. 7, no. 12, pp. 1578–1586, 2007.

[144] D. Stoppa, N. Massari, L. Pancheri, M. Malfatti, M. Perenzoni, and L. Gonzo, "A range image sensor based on 10- μm lock-in pixels in 0.18-μm CMOS imaging technology," *IEEE Journal of Solid-State Circuits*, vol. 46, no. 1, pp. 248–258, 2011.

[145] https://thinklucid.com/helios-time-of-flight-tof-camera/, [Online; accessed on 21-June-2022].

[146] https://www.ifm.com/gb/en/product/O3D303?tab=details, [Online; accessed on 21-June-2022].

[147] D. Pierrottet, F. Amzajerdian, L. Petway, B. Barnes, G. Lockard, and M. Rubio, "Linear FMCW laser radar for precision range and vector velocity measurements," *MRS Online Proceedings Library (OPL)*, vol. 1076, 2008.

[148] J. Zheng, "Analysis of optical frequency-modulated continuous-wave interference," *Applied optics*, vol. 43, no. 21, pp. 4189–4198, 2004.

[149] https://www.oequest.com/getDatasheet/id/13138-13138.pdf, [Online; accessed on 2-Feb-2022].

[150] A. Vasilyev, N. Satyan, S. Xu, G. Rakuljic, and A. Yariv, "Multiple source frequency-modulated continuous-wave optical reflectometry: theory and experiment," *Applied optics*, vol. 49, no. 10, pp. 1932–1937, 2010.

[151] J. Qin, Q. Zhou, W. Xie, Y. Xu, S. Yu, Z. Liu, Y. tian Tong, Y. Dong, and W. Hu, "Coherence enhancement of a chirped dfb laser for frequency-modulated continuous-wave reflectometry using a composite feedback loop," *Optics letters*, vol. 40, no. 19, pp. 4500–4503, 2015.

[152] E. Baumann, F. R. Giorgetta, I. Coddington, L. C. Sinclair, K. Knabe, W. C. Swann, and N. R. Newbury, "Comb-calibrated frequency-modulated continuous-wave ladar for absolute distance measurements," *Optics letters*, vol. 38, no. 12, pp. 2026–2028, 2013.

[153] https://www.id-photonics.com/images/stories/PDF/Data_sheet_CBDX-x-x-xx.pdf, [Online; accessed on 21-June-2022].

[154] https://www.findlight.net/front-media/products/datasheet/RIO-PLANEX-Series-1550nm-Low-Phase-Noise-Narrow-Linewidth-External-Cavity-Laser.pdf, [Online; accessed on 21-June-2022].

[155] Z. Xu, L. Tang, H. Zhang, and S. Pan, "Simultaneous real-time ranging and velocimetry via a dual-sideband chirped lidar," *IEEE Photonics Technology Letters*, vol. 29, no. 24, pp. 2254–2257, 2017.

[156] P. A. Sandborn, N. Kaneda, Y.-K. Chen, and M. C. Wu, "Dual-sideband linear FMCW lidar with homodyne detection for application in 3D imaging," *2016 Conference on Lasers and Electro-Optics (CLEO)*, p. STu4H.8, 2016.

[157] T. Liao, M. Hameed, and R. Hui, "Bandwidth efficient coherent lidar based on phase-diversity detection," *Applied Optics*, vol. 54, no. 11, pp. 3157–3161, 2015.

[158] Z. Xu, K. Chen, H. Zhang, and S. Pan, "Multifunction lidar system based on polarization-division multiplexing," *Journal of Lightwave Technology*, vol. 37, no. 9, pp. 2000–2007, 2019.

[159] S. Gao and R. Hui, "Frequency-modulated continuous-wave lidar using I/Q modulator for simplified heterodyne detection," *Optics letters*, vol. 37, no. 11, pp. 2022–2024, 2012.

[160] J. Wojtanowski, M. Zygmunt, M. Kaszczuk, Z. Mierczyk, and M. Muzal, "Comparison of 905 nm and 1550 nm semiconductor laser rangefinders' performance deterioration due to adverse environmental conditions," *Opto-Electronics Review*, vol. 22, no. 3, pp. 183–190, 2014.

[161] S. Crouch, "Advantages of 3D imaging coherent lidar for autonomous driving applications," in *Proceedings of the 19th Coherent Laser Radar Conference, Okinawa, Japan*, 2018, pp. 18–21.

[162] https://www.laserfocusworld.com/test-measurement/test-measurement/article/16566903/blackmore-launches-450-m-doppler-lidar-for-autonomous-vehicle-fleets, [Online; accessed on 21-June-2022].

[163] https://www.silc.com/product/, [Online; accessed on 14-April-2022].

[164] https://www.aeva.com/aeries-ii/, [Online; accessed on 21-June-2022].

[165] https://velodynelidar.com/wp-content/uploads/2019/12/63-9229_Rev-K_Puck-_Datasheet_Web.pdf, [Online; accessed on 14-April-2022].

[166] http://webfile.focuslight.com/web/image/20210611/Rev02%20LE02%20Datasheet%20EN.pdf, [Online; accessed on 21-June-2022].

[167] https://www.ofcconference.org/library/exhibits/OFC/2021/pdfs/1447255-pb-productBrochure3.pdf, [Online; accessed on 21-June-2022].

[168] https://www.st.com/resource/en/datasheet/vl53l0x.pdf, [Online; accessed on 21-June-2022].

[169] B. Zhou, Y. Peng, and D. Hwang, "Pipeline FFT architectures optimized for FPGAs," *International Journal of Reconfigurable Computing*, vol. 2009, 2009.

[170] T. Xu, G. Jacobsen, S. Popov, M. Forzati, J. Mårtensson, M. Mussolin, J. Li, K. Wang, Y. Zhang, and A. T. Friberg, "Frequency-domain chromatic dispersion equalization using overlap-add methods in coherent optical system," *Journal of optical communications*, vol. 32, no. 2, pp. 131–135, 2011.

[171] K. Kikuchi, "Fundamentals of coherent optical fiber communications," *Journal of Lightwave Technology*, vol. 34, no. 1, pp. 157–179, 2015.

[172] K. Ishihara, R. Kudo, T. Kobayashi, A. Sano, Y. Takatori, T. Nakagawa, and Y. Miyamoto, "Frequency-domain equalization for coherent optical transmission systems," in *Optical Fiber Communication Conference*, 2011, p. OWW4.

[173] E. Ip and J. M. Kahn, "Feedforward carrier recovery for coherent optical communications," *Journal of Lightwave Technology*, vol. 25, no. 9, pp. 2675–2692, Sep. 2007.

[174] S. Ruder, "An overview of gradient descent optimization algorithms. arxiv 2016," *arXiv preprint arXiv:1609.04747*, 2016.

[175] G. P. Agrawal, "Polarization effects," in *Nonlinear fiber optics*. Elsevier, 2013.

[176] https://acacia-inc.com/blog/when-lightning-strikes-why-fast-sop-tracking-is-important/, [Online; accessed on 21-June-2022].

[177] A. Alvarado, T. Fehenberger, B. Chen, and F. M. Willems, "Achievable information rates for fiber optics: Applications and computations," *Journal of Lightwave Technology*, vol. 36, no. 2, pp. 424–439, 2017.

[178] A. Alvarado, E. Agrell, D. Lavery, R. Maher, and P. Bayvel, "Replacing the soft-decision FEC limit paradigm in the design of optical communication systems," *Journal of Lightwave Technology*, vol. 33, no. 20, pp. 4338–4352, 2015.

[179] E. Collett, "The wave theory of light," in *Field guide to polarization*. Spie Bellingham, WA, 2005.

[180] M. Seimetz, *High-order modulation for optical fiber transmission*. Springer, 2009.

[181] D. Uttam and B. Culshaw, "Precision time domain reflectometry in optical fiber systems using a frequency modulated continuous wave ranging technique," *Journal of Lightwave Technology*, vol. 3, no. 5, pp. 971–977, 1985.

[182] M. G. Taylor, "Phase estimation methods for optical coherent detection using digital signal processing," *Journal of Lightwave Technology*, vol. 27, no. 7, pp. 901–914, 2009.

[183] https://www.lasercomponents.com/de/?embedded=1&file=fileadmin/user_upload/home/Datasheets/ixblue/mxiqer-ln-30.pdf&no_cache=1, [Online; accessed on 3-May-2021].

[184] https://www.neophotonics.com/products/semiconductor-optical-amplifier-soa/, [Online; accessed on 3-May-2021].

[185] https://ii-vi.com/product/flexsom-edfa/, [Online; accessed on 3-May-2021].

[186] https://www.epsglobal.com/Media-Library/EPSGlobal/Products/files/finisar/roadm-fws-optoelectronic/Single-Channel-Micro-EDFA.pdf?ext=.pdf, [Online; accessed on 3-May-2021].

[187] C. Häger and H. D. Pfister, "Nonlinear interference mitigation via deep neural networks," in *Optical Fiber Communication Conference*. Optica Publishing Group, 2018, p. W3A.4.

[188] P. P. Shinde and S. Shah, "A review of machine learning and deep learning applications," in *2018 Fourth International Conference on Computing Communication Control and Automation (ICCUBEA)*, 2018, pp. 1–6.

[189] J. Ker, L. Wang, J. Rao, and T. Lim, "Deep learning applications in medical image analysis," *IEEE Access*, vol. 6, pp. 9375–9389, 2018.

[190] D. W. Otter, J. R. Medina, and J. K. Kalita, "A survey of the usages of deep learning for natural language processing," *IEEE Transactions on Neural Networks and Learning Systems*, vol. 32, no. 2, pp. 604–624, 2021.

[191] X. Wu, J. A. Jargon, R. A. Skoog, L. Paraschis, and A. E. Willner, "Applications of artificial neural networks in optical performance monitoring," *Journal of Lightwave Technology*, vol. 27, no. 16, pp. 3580–3589, 2009.

[192] F. N. Khan, Y. Zhou, A. P. T. Lau, and C. Lu, "Modulation format identification in heterogeneous fiber-optic networks using artificial neural networks," *Optics express*, vol. 20, no. 11, pp. 12 422–12 431, 2012.

[193] S. Droste, G. Ycas, B. R. Washburn, I. Coddington, and N. R. Newbury, "Optical frequency comb generation based on erbium fiber lasers," *Nanophotonics*, vol. 5, no. 2, pp. 196–213, 2016.

[194] T. Udem, R. Holzwarth, and T. Hänsch, "Femtosecond optical frequency combs," *The European Physical Journal Special Topics*, vol. 172, no. 1, pp. 69–79, 2009.

[195] A. Pasquazi, M. Peccianti, L. Razzari, D. J. Moss, S. Coen, M. Erkintalo, Y. K. Chembo, T. Hansson, S. Wabnitz, P. Del'Haye *et al.*, "Micro-combs: A novel generation of optical sources," *Physics Reports*, vol. 729, pp. 1–81, 2018.

[196] I. Coddington, W. C. Swann, L. Nenadovic, and N. R. Newbury, "Rapid and precise absolute distance measurements at long range," *Nature photonics*, vol. 3, no. 6, pp. 351–356, 2009.

[197] E. L. Teleanu, V. Durán *et al.*, "Electro-optic dual-comb interferometer for high-speed vibrometry," *Optics Express*, vol. 25, no. 14, pp. 16 427–16 436, 2017.

[198] M.-G. Suh and K. J. Vahala, "Soliton microcomb range measurement," *Science*, vol. 359, no. 6378, pp. 884–887, 2018.

[199] J. Riemensberger, A. Lukashchuk, M. Karpov, W. Weng, E. Lucas, J. Liu, and T. J. Kippenberg, "Massively parallel coherent laser ranging using a soliton microcomb," *Nature*, vol. 581, no. 7807, pp. 164–170, 2020.